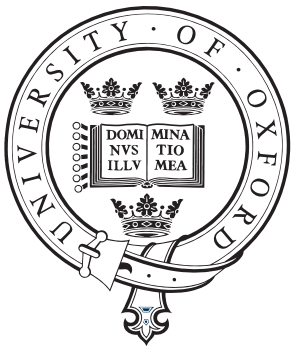

Theoretical and experimental investigations of turbulent jet formation in planetary fluid dynamics

A thesis submitted for the degree of Doctor of Philosophy

Robin D. Wordsworth
Linacre College, Oxford University

January 21, 2009

Abstract

This thesis describes theoretical and experimental investigations of planetary-scale turbulence and jet formation.

In the first section, the interaction between zonal jets and planetary waves is described using techniques adapted from quantum mechanics. The planetary wavefield is treated as a ensemble of wavepackets, and the quantum mechanical Wigner function is used to construct an equation for the evolution of wavepacket density in phase space that includes all effects of the mean flow on the waves. Analytical arguments, combined with a simple numerical model, are then used to give an intuitive picture of jet formation as a positive feedback process in which a jet 'feeds' on wavepackets as it grows. Furthermore, it is shown that the phase space approach also allows a very intuitive explanation of east-west jet asymmetry in terms of wavepacket motion.

In the second section, a differentially heated rotating annulus experiment is used to study planetary-scale turbulence and jet formation in the laboratory. The cases of both flat and sloping vertical boundaries were investigated; in the former, it was found that the flow evolved into a statistically steady state typically consisting of a large-scale coherent structure plus a more rapidly varying eddy field. In the latter case, the sloping boundaries caused turbulent eddies to behave like planetary waves at large scales, and eddy interaction with the zonal flow then led to the formation of several alternating jets at mid-depth. The jets in the experiment did not scale with the Rhines length, and spectral analysis of the flow indicated a distinct separation between jets and eddies in wavenumber space, with direct energy transfer occuring *nonlocally* between them. This result suggests that the traditional turbulent cascade picture of zonal jet formation may be an inappropriate one in the geophysically important case of large-scale flows forced by differential solar heating.

Additional experiments were performed with an insulating barrier that blocked flow in the azimuthal direction. At low rotation rates, a large gyre was observed at mid-depth in the annulus, with an intense 'southward' boundary current on the left side of the barrier. At high rotation rates, the flow became turbulent, and the gyre split into several zonal jets away from the barrier. These experiments may have implications for physical oceanography, as recent observations and simulations of the Earth's deep oceans have indicated that zonal jet formation may also be occurring there.

In the final section, the numerical model of the first section is extended, in order to produce a simple reduced model of the jet formation observed in the unblocked experiments. The model results were qualitatively very similar to the experiment, although quantitative differences existed. The reasons for the discrepancies are discussed, along with suggestions for future research and implications for the modelling of real planetary-scale fluids. In particular, it is noted that if nonlocal energy transfer dominates in real geophysical fluids such as the Earth's atmosphere, it may be possible to construct faster general circulation models that parameterise the effects of eddy-eddy interactions.

Contents

Acknowledgements

I would like to thank:

My supervisor, Peter Read, for constant encouragement and helpful advice on all parts of the project. My parents for their kindness and support. Hiro Yamazaki for his help on all aspects of fluid dynamics, his creative approach to experimental physics and also for his role in the early days as a relationship counsellor between myself and my computer. David Andrews for several enlightening theoretical discussions, and also for kindly agreeing to give comments on an early draft of my theoretical paper.

Everybody in the AOPP workshop for superb technical support throughout the experimental part of my DPhil; in particular, Duncan and Jason for helping with the disassembly and repair of the rotating table, and Andy Clack for help on electrical and mechanical issues too numerous to list. The Natural Environment Research Council for funding this DPhil, and Linacre College, the Institute of Physics and the Royal Meteorological Society for helping to fund my attendance at overseas conferences. Many people from AOPP and elsewhere, including Chris Jones, Joel Sommeria, Andy Ingersoll, Ben, Colin, Con, Lee, Lena, Luca, Roland and Scott for interesting and wide-ranging debates on all aspects of planetary physics.

Also Ana, Alfonso and Tom, for their solidarity in fighting the natural tendency towards chaos of the planetary fluid dynamics lab. Sarah and Monika for shielding me from numerous vast and terrifying bureaucracies. Jo, Zhenyu and Ranah for allowing me to smoke their cigarettes during lunch breaks whilst simultaneously denying I was a smoker.

Finally and most importantly, Seirian for always being there when it counted the most.
Diolch am wneud fy mywyd mor hwylus — byddai'n caru ti am byth.

I am an old man now, and when I die and go to heaven there are two matters on which I hope for enlightenment. One is quantum electrodynamics, and the other is the turbulent motion of fluids. And about the former I am rather optimistic.

— Horace Lamb, 1932 speech to the British Association for the Advancement of Science.

Chapter 1

Introduction

Turbulence is the last great unsolved problem of classical physics.

This is unfortunate, as the most common state of fluid systems in the Universe is a turbulent one. From the motion of stellar interiors to the large-scale structure of the cosmos; from oceanic eddies that transport heat, plankton and human pollution to the flow of blood in our own bodies — highly nonlinear fluid motion is everywhere. If we have until now failed to understand it completely, it is certainly not through want of examples to observe in nature.

This thesis is concerned only with a very specialised case: that of turbulence in planetary atmospheres and oceans on the largest scales. Specialised as it is, planetary-scale fluid dynamics is a subject of great practical importance to all of us, as it determines both the day-to-day weather and the long term climate of Earth. It is also fascinating from a fundamental point of view. The rotation of planets combined with their spherical geometry leads their atmospheres and oceans to behave in unique and frequently counterintuitive ways. Indeed, after three years of DPhil research I am now strongly of the belief that traditional views of turbulence are, at best, of limited value in understanding the way planetary-scale fluids behave.

The central focus of the work presented here is zonal jet formation; the physical process by which a turbulent flow organises itself into alternating bands of high east-west velocity, separated by regions of intense shear and vortex formation. The most famous example of zonal jets in nature are the belts and zones of the planet Jupiter, as shown in Figure 1.1. However, jet formation also occurs in a wide variety of other situations in physics.

In this introductory chapter, we explore just why planetary-scale turbulence and jets are so important and challenging to study. The different situations in nature where jet formation occurs are described and previous work on the subject is briefly summarised (some of it is reviewed in greater detail in Chapter 2). At the end of the chapter, the central aims of this study are stated, and an outline of the entire thesis is given.

1.1 Turbulence and jet formation in nature

The most famous examples of jets in nature, the colourful belts and zones of Jupiter, have been observed more or less continuously since the introduction of the first telescopes. Perhaps the very

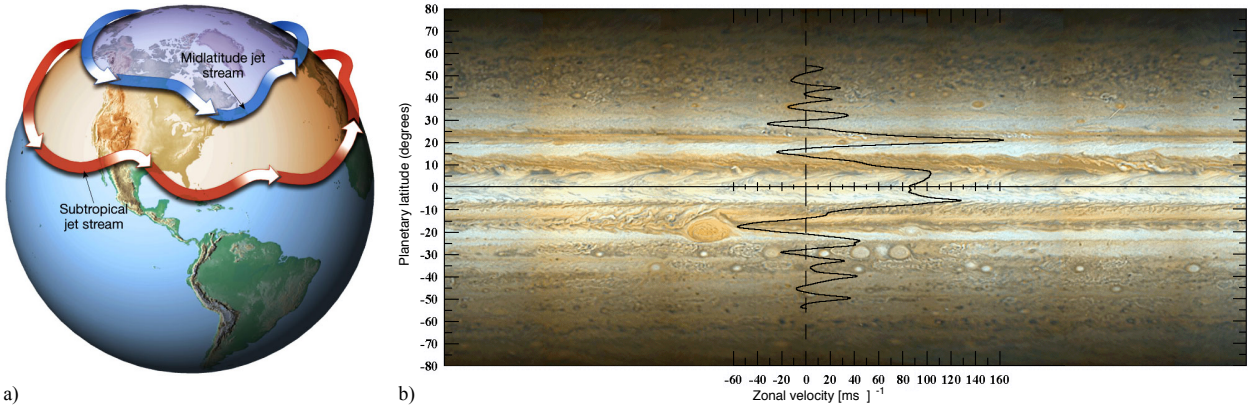

Figure 1.1: Some examples of zonal jets in nature. a) A schematic of the global circulation of Earth's atmosphere (reproduced from *The Atmosphere, Lutgens and Tarbuck, 2001*). b) A rectangular projection of Jupiter's atmosphere in the visible spectrum. The zonal velocity profile as measured by the NASA Voyager probe is superimposed in black.

first human to observe Jupiter's jets was the Italian astronomer Giovanni Cassini, who is believed to have noted the planet's unusual striped appearance as early as the 1660s [18].

The birth of interplanetary exploration in the 1960s revolutionised observation of the Jovian atmosphere. The hugely successful Voyager and Galileo missions, in particular, allowed quantitative measurements of jet and vortex velocities for the first time, and theoretical understanding of the planet's rich atmospheric dynamics has benefited immensely from the wealth of data that these probes returned [6].

Although less photogenic in the visible spectrum due to their differing atmospheric chemistry, the other gas giant planets also feature persistent east-west jets. Saturn, in particular, has almost as many jets as Jupiter, along with many other exotic fluid dynamical phenomena including polar hotspots and a hexagonal vortex chain in the northern hemisphere [23][66]. Recent observations of the cloud layers of both Jupiter and Saturn by the NASA-ESA Cassini probe have also confirmed an idea long predicted by theorists: the jets are at least partially maintained by nonlinear eddy fluxes of momentum [22][59]. Rather than acting as a drag on the jets, the small-scale eddies and vortices in the atmosphere *actively feed them*.

Turbulent jet formation also occurs in the atmosphere of Earth (see Figure 1.1). Although Earth's subtropical jet stream exists mainly because of the effect of the Coriolis pseudoforce on the upper branch of the Hadley cell, the mid-latitude and polar jets are mostly maintained by nonlinear eddy forcing, just as in the gas giant planets [34]. There are some differences between the two cases, of course. Perhaps most important is the nature of the forcing: while convection from the deep interior is believed to be the main driver of the large-scale circulation of Jovian atmospheres, it is *baroclinic instability*, caused ultimately by the variation in solar heating with latitude, which dominates in the terrestrial case.

The jets of Earth's atmosphere and those of the gas giant planets are equally fascinating to the physicist. Due to the fundamental role that global jets play in Earth's climate, however, their practical importance is considerably greater. As well as affecting global chemistry by controlling the way trace chemicals are transported, they strongly influence (and are influenced by) the development

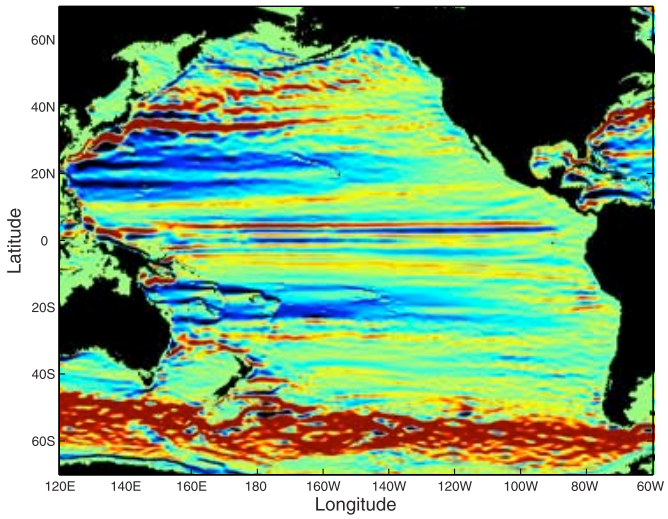

Figure 1.2: Contour plot of zonal (east-west) velocity from a high-resolution numerical simulation of Earth's Pacific ocean. Image reproduced with permission from Richards et al. [40].

of storms and local weather systems at different latitudes.

Recently, there has been increasing evidence that zonal jets are even more common in planetary-scale fluid systems than was previously thought. In particular, some new studies have hinted that an analogous process to the jet formation seen in atmospheres may also be occurring in Earth's oceans [40][55]. Figure 1.2 shows a contour plot of zonal velocity from a recent high-resolution numerical simulation reported in Richards et al. [40]. In their model, the authors found evidence of east-west bands of zonal velocity in the Pacific ocean that extended deep into the abyssal region. However, the jets produced were only visible after an intermediate time-average. On longer timescales, they were observed to slowly merge and bifurcate.

At the time of writing, oceanic zonal jet formation is a open area of research, and it may well be some time before the existence of persistent jets can be unambiguously verified or denied. In Chapter 7, some experimental results are presented which demonstrate that, from a fundamental perspective, it is at least possible for ocean basin jet formation to occur due to the same basic phenomenon responsible for jets in planetary atmospheres.

Finally, jet formation also occurs in tokomak plasmas [32]. Due to a fascinating mathematical analogy between planetary waves (see section 2.1.1) and plasma drift waves, the rotating fluid and plasma processes are dynamically extremely similar. This has lead to an interesting transfer of ideas between the two fields: some of the papers referenced in Chapter 3, for example, were written by plasma physicists on the drift wave – zonal flow problem.

1.2 Previous theoretical and numerical work

Many decades of intensive research has been put into understanding how turbulent fluids behave. Some of the world's most famous physicists have worked on the problem; Lev Landau, for example,

provided some early ideas that, although ultimately incorrect, provided much inspiration for future researchers.

The most successful attempt at a theory of turbulence to date came from the brilliant Russian mathematician Andrey Kolmogorov, in 1941 [33]. Kolmogorov used scaling and spectral analysis to make concrete predictions about idealised three-dimensional turbulent flow that hold extremely well in many cases. Despite his successes, however, it has never been possible to derive his results from the underlying equations of fluid dynamics. In Chapter 2, the Kolmogorov theory is briefly reviewed, along with similar heuristic approaches to understanding two-dimensional turbulence.

Planetary-scale turbulence is an even more complex and challenging subject. This is partly because in real atmospheres there are usually a variety of forcing and damping mechanisms present. More fundamentally, however, the rotation and spherical geometry of planets means that their large-scale flows are usually strongly *anisotropic*. As most classical turbulence ideas are built on isotropic assumptions, this makes their relevance of dubious validity, although they are often still used in the absence of other approaches.

There have been some important theoretical contributions to the planetary-scale turbulence problem, although all of them are partly heuristic. Peter Rhines, for example, laid out ideas on planetary waves and turbulence in a 1975 paper that is widely regarded as having kick-started modern thinking on the jet formation problem [54]. Also important was the work of Rick Salmon in 1978, who used statistical methods to make fairly robust predictions about the behaviour of planetary-scale turbulence forced by baroclinic instability [57]. Both studies are reviewed, along with other important work on the subject, in Chapter 2.

Given the difficulties associated with turbulence theory, however, it should be unsurprising that extensive work has been put into other approaches to the problem. In particular, many researchers have turned to numerical simulations of various idealised fluid systems. Starting with the early studies of Wiliams [68], there have now been many numerical investigations into the dynamics of turbulent jets. The most important and relevant of these are also reviewed in Chapter 2.

1.3 Laboratory models of jets and turbulence

Numerical simulations are extremely powerful tools in physics, and it is likely that as computing power increases, their importance can only grow. However, they do have disadvantages. They usually require parameterisations that can make their output difficult to interpret or even physically incorrect. The modelling of turbulent fluids, in particular, is extremely challenging, as the strong nonlinearity of such flows demands extremely high spatial and temporal model resolution.

Laboratory models of atmospheric and oceanic processes are now well-established as an alternative approach to the problem. They have unique advantages; for one, they employ real fluids, and hence do not suffer from discretisation errors, or the physically dubious 'numerical dissipation' that plagues computer models of turbulence.

In a very real sense, however, laboratory analogues should be seen as simply 'computer simulations by other means', as their aims are essentially the same; to reproduce the observed phenomena in settings that can be carefully controlled. Both methods have an essential role in planetary physics, as they allow one to apply the scientific method to a problem with a level of rigour that is never possible in observational work.

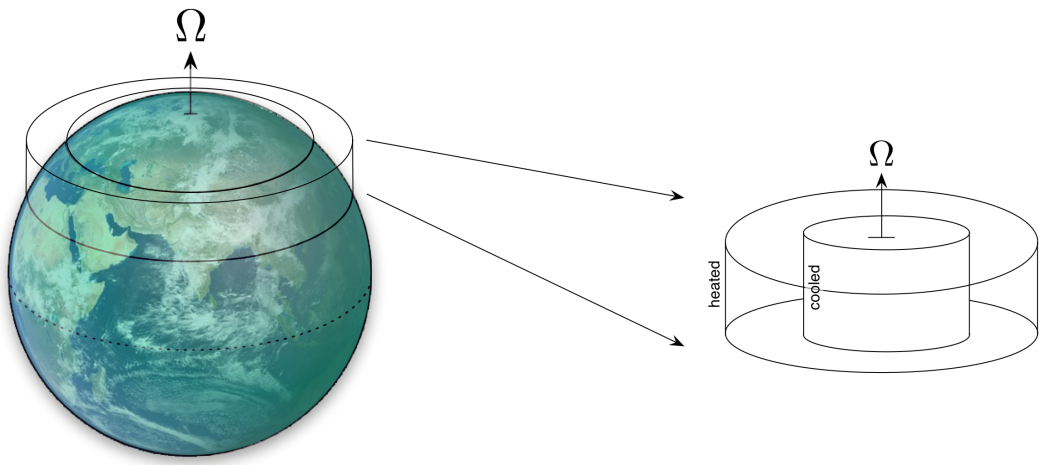

Figure 1.3: Schematic of the analogy between a planetary atmosphere at midlatitudes, and the differentially heated rotating annulus experiment.

Historically, attempts to simulate planetary atmospheric circulation in the laboratory date back as far as the work of Vettin in the 19$^{\text{th}}$ century, who placed ice in the centre of rotating dishes of air, with the aim of simulating the cooling effects caused by polar icecaps [67]. The first systematic investigation of laboratory models began with the independent work of Hide and Fultz in the 1950s [26][56]. They studied an experimental system, the differentially heated rotating annulus, which has proved of enduring relevance in the study of planetary atmospheres.

The idea behind the experiment, as shown schematically in Figure 1.3, is to reproduce the differential heating of a mid-latitude air mass in a rotating frame. Initially, the combined effects of differential heating and the Coriolis pseudoforce cause a vertically sheared zonal ('east-west') wind to develop. When the rotation rate of the turntable is increased above a certain critical value, this flow becomes hydrodynamically unstable, and exhibits a wide range of behaviour depending on the system parameters. Steady waves give way to aperiodic and eventually turbulent fluid behaviour as the system is pushed further away from the stable regime. The experiment is justifiably famous in the field of chaos theory, as it is believed to have inspired Lorenz to write his seminal paper *'Deterministic nonperiodic flow'* in the 1960s [37].

To reproduce jet formation in the laboratory, it is essential to account for one additional effect — the variation of Coriolis effect with latitude or *planetary β-effect*. One way this can be done is by placing sloping top and bottom boundaries in the annulus[1].

There have been several laboratory studies to date that attempted to simulate planetary turbulence and jet formation. Hide and Mason [29] studied the effects of sloping boundaries in some of their later experiments, but did not investigate regions of parameter space where multiple jet formation occurred. Other early studies include the work of Busse [11], who simulated deep planetary convection in rapidly rotating shells, with the centrifugal pseudoforce playing the role of a 'reversed' gravitational field.

A more recent experiment by Condie and Rhines [13] involved a heated rotating dish with a curved

[1]In heat-driven flows, the analogy between the β-effect and sloping topography is slightly complicated by stratification effects. This issue is discussed further in Chapters 2 and 6.

lower surface [13]. In that work, the development of a meandering surface jet was observed via surface aluminium streak imaging, and it was suggested that its formation could be explained purely through a conservation of angular momentum argument. However, no velocity field information was derived for the experiment, and therefore the contributions of nonlinear eddy fluxes to the overall momentum balance could not be computed.

Bastin and Read [7] used ohmic heating to *internally* heat a rotating fluid, with the aim of qualitatively reproducing the radiative forcing of the upper atmospheres of gas giant planets. They observed some evidence of jet formation with both negative and positive sloping boundaries, and noted that the jet structure could not be easily predicted from the form of the background thermal forcing.

In 2004, Read, Yamazaki et al., reported an experiment performed in a 13 m diameter annulus with convective forcing provided by spraying salt water onto fresh [51][52]. Multiple jets were observed in the fluid that were instantaneously barotropically unstable, and it was found that zonal acceleration and Reynolds stress were correlated, suggesting that barotropic eddies were the main driving mechanism for the jet.

Finally, a second experiment was carried out very recently at the same facility by a number of researchers (including the author of this thesis). This time, the sloping lower boundary of the tank was heated, in an attempt to more directly simulate the gas giant jet convection process. Jet formation was observed at high rotation rates, and dye visualisation of small scales revealed that the formation of convective plumes (similar to 'dust-devils') was extremely spatially intermittent. At the time of writing, however, analysis of the results is still at an early stage.

1.4 Thesis aims and overview

The aim of this DPhil project was to increase our understanding of the turbulent jet formation process. To this end, both theoretical and experimental research was performed.

The aim of the experimental research was to systematically study turbulence and jet formation in the 'classical' differentially heated rotating annulus. Although the setup of the experiment was standard, the dimensions of the apparatus allowed the investigation of a turbulent region of parameter space than has never before been studied in detail. To aid the study of this region, a new data acquisition system was also implemented, allowing much more detailed velocity field information to be derived than was previously possible.

The combination of these two improvements meant that a much greater focus on the dynamics of jet formation was possible than in previous investigations. To focus the analysis of the experimental results, several specific questions were posed. They are:

- Do multiple barotropic jets develop in the experimental system?
- If so, are the jets dynamically stable?
- How do they interact with the turbulent eddies?
- Is a turbulent cascade of energy from small to large scales occurring?
- If not, can wave-mean flow theory be used to describe the jet formation process?

The final question posed was

- Do jets form in the annulus when a vertical flow barrier is also present?

This last one is somewhat removed from the main topic of the thesis, but it is interesting nonetheless, as it relates to the real-world question mentioned in Section 1.1:

- Are the zonal jets found in recent high resolution ocean simulations dynamically related to those seen in planetary atmospheres?

This provided the motivation for the ocean wall experiments of Chapter 7.

The theoretical work described here had two main aims. The first was to develop new ways of describing general interactions between zonal jets and planetary waves, in order to gain a deeper understanding of the dynamics. The motivation for this work is explained further in Chapter 2, where previous theoretical papers most relevant to the new approach are also reviewed. The second, more ambitious goal was to develop a simplified numerical model that could predict the results of the experiments. The guiding principle was to reduce the equations describing jet formation to as simple a form as possible, without cutting out the parts that were essential to the process.

The structure of this thesis is as follows. In Chapter 2, basic equations and concepts are reviewed, and the properties of some idealised turbulent flows are described. In Chapters 3 and 4, the Wigner function approach is introduced. Through the use of ideas from quantum mechanics, a combined real and spectral space view of the dynamics is constructed, and used to explain jet formation in a simple test case.

In Chapter 5, the setup of the rotating annulus experiment is described. In Chapter 6, results from the experiment are presented, with particular attention devoted to the sloping boundary cases in which multiple jet formation occurred. The ocean wall experiments, which were conducted with a flow barrier in the annulus, are described in Chapter 7.

In Chapter 8, the methods of Chapters 3 and 4 are used to make an extremely simple model of the unblocked sloping boundary experiments. The model setup and approximations are described, and then simulations are presented with the same general parameters as an experiment in which multiple jet formation occurred. The successes of the model in reproducing the observed experimental results, along with its weaknesses, are then discussed in detail. Finally, in Chapter 9, we discuss the success of the thesis in achieving the aims outlined here. Implications of the results are discussed, and suggestions are made for possible future work that could extend the ideas presented.

Chapter 2

Fundamental theory

In this chapter we introduce some basic theoretical concepts that will be needed throughout the rest of the thesis. The fundamental equations of fluid dynamics are stated (not derived!), and cast into a form that is most useful for describing planetary atmospheres and oceans. We then discuss the general properties of turbulent flows in a few different cases, also reviewing some of the most famous historical attempts to describe turbulence theoretically.

2.1 Fluid mechanics in a rotating frame

In the absence of forcing and damping, the local acceleration of any small portion of a fluid must equal all the forces imposed upon it. In the absence of sources and sinks, the mass of any small portion of a fluid is also conserved. These two fundamental principles are the basis of the *Euler equations* for non-relativistic fluid dynamics

$$\frac{d^2\mathbf{x}}{dt^2} = \frac{\partial \mathbf{u}}{\partial t} + (\mathbf{u}\cdot\nabla)\,\mathbf{u} = -\frac{1}{\rho}\nabla p + \nabla\Phi \tag{2.1}$$

$$\frac{\partial \rho}{\partial t} + \nabla\cdot(\mathbf{u}\rho) = 0, \tag{2.2}$$

where $\mathbf{u}$ is the (three-dimensional) velocity vector, ρ is density, p is pressure and Φ is a scalar representing all conservative forces.

In a rotating coordinate frame, Coriolis and centrifugal correction terms must be added to the equations of motion for any body. Furthermore, any real fluid will continually lose kinetic energy due to viscous damping. Equation (2.1) is therefore generalised to the more useful and physically realistic *Navier-Stokes equation*

$$\frac{\partial \mathbf{u}}{\partial t} + (\mathbf{u}\cdot\nabla)\,\mathbf{u} + \mathbf{f}\times\mathbf{u} = -\frac{1}{\rho}\nabla p + \nabla\Phi' + \nu\nabla^2\mathbf{u}. \tag{2.3}$$

Here $\mathbf{f} = 2\boldsymbol{\Omega}$, the Coriolis parameter, is twice the axial vector of planetary rotation rate and $\Phi' = \Phi + \Phi_c$ is the original conservative scalar term plus a contribution Φ_c due to the centrifugal pseudoforce. The parameter ν is the viscosity of the fluid. When combined with an appropriate equation of state and boundary conditions, equations (2.2) and (2.3) allow the evolution of a given fluid to be described completely.

In the absence of forcing, viscosity and diabatic heating effects, there is another locally conserved quantity in a fluid besides mass. This quantity is the *potential vorticity*, Π, defined as

$$\Pi = \frac{(\nabla \times \mathbf{u} + \mathbf{f}) \cdot \nabla \eta}{\rho} \tag{2.4}$$

in its most general form. The variable $\eta = \eta(p, \rho)$ can be any locally conserved thermodynamic scalar, such as entropy, or potential temperature in planetary atmospheric flows. Due to its dynamical significance, potential vorticity is an immensely useful quantity in planetary fluid dynamics, and frequent reference is made to it in this report.

The proof that Π is conserved is not a difficult one, and it is covered in detail in many texts (e.g., [44], [58]). As will be seen in the next section, in approximate planetary-scale fluid equations, potential vorticity becomes an even more useful and important quantity.

2.1.1 Approximate equations for planetary-scale fluids

In practical terms, (2.3) is rarely useful for theoretical or numerical analyses of geophysical turbulence. The chief reason for this is that it admits sound and inertia-gravity waves as solutions, both of which are of much higher frequency and smaller scale than the slow, planet-wide motions we are interested in.

To filter out the less interesting small-scale motion, it is necessary to bring in some extra physics. We make three assumptions. The first is that the fluid is effectively incompressible. In an incompressible fluid, (2.2) decouples into the two equations

$$\nabla \cdot \mathbf{u} = 0, \qquad (\partial_t + \mathbf{u} \cdot \nabla)\, \rho = D\rho = 0 \tag{2.5}$$

and sound waves vanish entirely. Physically, this means that we are treating their propagation speed as infinite when compared to that of the larger-scale fluid motion.

The second assumption made is that due to the planet's gravitational pull, the fluid is strongly stratified. In other words, it is close to a state of *hydrostatic balance*. If perfect hydrostatic balance holds in a fluid, the vertical component of the Navier-Stokes equation (2.3) becomes replaced by the simple relation

$$\frac{dp}{dz} = \rho \frac{d\Phi_g}{dz} = -\rho g. \tag{2.6}$$

The final assumption is that at large scales, the horizontal pressure gradient is approximately balanced by the Coriolis pseudoforce $\mathbf{f} \times \mathbf{u}$. If this is the case then (assuming for simplicity that $\mathbf{\Omega} = (0, 0, \Omega)$) the two horizontal components of (2.3) become

$$(\mathbf{f} \times \mathbf{u})_h = -\frac{1}{\rho} \nabla_h p \tag{2.7}$$

A fluid in the state defined by (2.7) is said to be in *geostrophic balance*. Note that (2.7) implies a very unintuitive result: the horizontal motion of fluid elements is perpendicular, not parallel, to the force applied to them! Clearly, one must be very careful when applying previous assumptions and prejudices to fluid motion in a rotating frame.

Neither (2.6) nor (2.7) involve time derivatives of any fields. In order to construct a reduced dynamical equation, we need to examine the fluid behaviour when only small departures are allowed

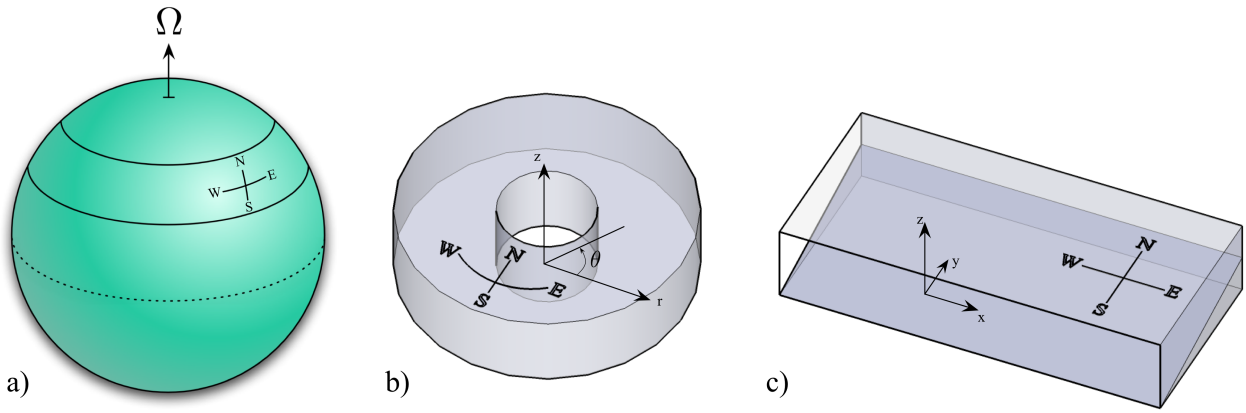

Figure 2.1: Schematic comparison of the real and approximate geometries of planetary fluid dynamics. a) The true spherical geometry of a planet. Latitudinal black solid lines indicate region over which a β-plane approximation might be expected to be valid. b) The experimental rotating annulus geometry. Azimuthal and radial directions correspond to east-west and north-south respectively. c) The β-plane channel geometry. Here, curvature disappears entirely, and the sinusoidal variation of Coriolis effect with latitude is treated as approximately linear (shown schematically as a sloping bottom boundary here).

from these two constraints. Before we do this, however, it is convenient to bring in one further approximation — this time a geometrical one. The full spherical coordinate system covering the entire planet is going to be replaced by a Cartesian one, valid over a certain latitude band. This approximation is perhaps made clearer by the diagrams in Figure 2.1.

Although forcing the equations of motion into a Cartesian form like this may seem like a drastic thing to do, it is more than paid for by the resulting increase in simplicity. Geometrical transforms are a very common trick in planetary fluid dynamics research. In particular, they are also used to interpret the results of rotating annulus experiments, such as the ones reported in Chapters 5-7 of this thesis. Frequently there, we will refer to the radial and azimuthal directions as 'north-south' and 'east-west' respectively.

The Coriolis parameter, which in general depends on latitude in the form $f_z(\lambda) = 2\Omega \sin\lambda$, will only vary a little over the local latitude band. If we define a 'local north-south coordinate' $y \approx a(\lambda - \lambda_0)$ (and similarily an 'east-west' coordinate $x \approx a(\theta - \theta_0)$), a Taylor expansion yields

$$f_z(y) = f_z(0) + y\left(\frac{df}{dy}\right)_{y=0} + \ldots \approx f_0 + \beta y \tag{2.8}$$

with $f_0 = 2\Omega \sin\lambda_0$ and the constant factor $\beta = (2\Omega \cos\lambda_0)/a$. Naturally enough, (2.8) is called the *β-plane approximation*. As will be seen later in this chapter, the constraints on planetary-scale motion that result from it are fundamental to the jet formation process.

As was mentioned in Chapter 1, the effect of a linearly varying Coriolis parameter can be reproduced in the laboratory by the addition of sloping top and bottom boundaries to the rotating annulus. If the flow in the annulus is barotropic (constant with height), there is a mathematical isomorphism between the topographic and planetary β-effects. When added to differentially heated experiments, such as the one discussed in this thesis, sloping boundaries no longer have a direct quantitative equivalence to the β-effect. Qualitatively, however, their effects are very similar. The

issue is discussed in more detail in Chapter 6, where wave frequencies are directly calculated from experimental data and compared with theory.

Having constructed the Cartesian β-plane, we can now finish the derivation of the reduced planetary-scale equations. To this end, we define the Rossby number

$$\epsilon \equiv \frac{[(\mathbf{u}\cdot\nabla)\,\mathbf{u}]}{[\mathbf{f}\times\mathbf{u}]} = \frac{U}{f_0 L}, \tag{2.9}$$

a ratio between nonlinear and Coriolis effects. If ϵ is small, a formal perturbation expansion can be performed on the full dynamical equations (2.3), with dynamical fields like $\mathbf{u}$ expanded as

$$\mathbf{u} = \mathbf{u}_0 + \epsilon\mathbf{u}_1 + \ldots. \tag{2.10}$$

At zeroth order, exact geostrophic balance as stated by (2.7) will apply. At first order truncation, a closed set of equations for the zeroth and first order variables can be constructed, and the flow is termed *quasigeostrophic*.

Departures from the hydrostatically balanced density profile $\rho_0(z)$ can be treated in a similar way, via a linear expansion of the density ρ. In particular, the incompressible equation of continuity (2.5) becomes

$$D\rho \to D_0\rho_1 + w_1\frac{d\rho_0}{dz} = D_0\rho_1 - \frac{\rho_0(z_0)}{g}N^2 w_1 = 0 \tag{2.11}$$

$$N^2 \equiv -\frac{g}{\rho_0(z_0)}\frac{d\rho_0}{dz} \tag{2.12}$$

for the linear departure ρ_1 from the static profile. The quantity N is the buoyancy frequency; it is the characteristic oscillation rate of small fluid elements displaced vertically from their stably[1] stratified location.

When these two expansions from geostrophic and hydrostatic balance are applied to (2.3), the quasigeostrophic (QG) equations result

$$D_0 u_0 - f_0 v_1 - \beta y v_0 = 0 \tag{2.13}$$

$$D_0 v_0 + f_0 u_1 + \beta y u_0 = 0 \tag{2.14}$$

$$D_0\left(-\frac{g\rho_1}{\rho_0}\right) + N^2 w_1 = 0 \tag{2.15}$$

$$\nabla\cdot\mathbf{u}_1 = 0. \tag{2.16}$$

In the above, $D_0 = \partial_t + \mathbf{u}_0\cdot\nabla$ is the *geostrophic* advection operator, and $\mathbf{u}_1$ is logically termed the ageostrophic velocity. Note that the derivation of equations (2.13)-(2.16) is carried out in far more detail in planetary fluid dynamics textbooks (see for example [2]).

Simplified as they are, (2.13)-(2.16) still appear rather messy. Their elegance is best appreciated by rewriting everything in terms of the *quasigeostrophic* potential vorticity, defined as

$$\begin{aligned} q &\equiv \frac{\partial v_0}{\partial x} - \frac{\partial u_0}{\partial y} + \frac{\partial}{\partial z}\left(\frac{f_0^2}{N^2}\frac{\partial\psi}{\partial z}\right) + f_0 + \beta y \\ &= \nabla_h^2\psi + \frac{\partial}{\partial z}\left(\frac{f_0^2}{N^2}\frac{\partial\psi}{\partial z}\right) + f_0 + \beta y. \end{aligned} \tag{2.17}$$

[1]There are situations where N^2 becomes negative, such as when a denser fluid region is above a lighter one. Then, N will clearly be imaginary. In this case, displaced fluid elements may rise exponentially, the stratification is *unstable*... and the QG approximation can no longer be valid.

We use the lowercase symbol q to distinguish it from the more general potential vorticity Π defined in (2.4). The quantity ψ is the geostrophic streamfunction, defined by

$$\mathbf{u}_0 = \begin{pmatrix} -\partial_y \psi \\ \partial_x \psi \end{pmatrix} \qquad \text{and} \qquad \frac{\rho_1}{\rho_0(z_0)} = \frac{-f_0}{g}\frac{\partial \psi}{\partial z}. \tag{2.18}$$

By definition, in a steady, geostrophically balanced flow, fluid elements follow contour lines of ψ.

Just as Π is locally conserved in a general flow, q is conserved in a quasigeostrophic one. This fact can be proved by writing ∂_x(2.14) $-\partial_y$(2.13) and using incompressibility to arrive at

$$D_0 \left(\nabla_h^2 \psi + f_0 + \beta y \right) = f_0 \frac{\partial w_1}{\partial z}, \tag{2.19}$$

and then taking the vertical derivative of (2.15). With use of (2.18), the beautifully simple result[2]

$$D_0 q = 0 \tag{2.20}$$

follows.

Although (2.20) and the more general equation $D\Pi = 0$ appear very similar, (2.20) is in fact far more useful. This is because an *inversion relationship* exists between q and ψ. Knowledge of either of these scalar fields in a well-bounded domain allows us to derive the other, and hence to predict the evolution of the entire quasigeostrophic fluid.

In the presence of forcing and damping, the right hand side of (2.20) is no longer zero. In a real fluid, such as that in the rotating annulus experiment, non-conservative effects of some kind are always important. They are also included in some of the reduced model simulations (Chapters 4 and Chapter 8). The most important damping in geophysical fluids is usually *Ekman suction* — an effect whereby eddies and vortices cause vertical fluxes of fluid from boundary layers into the interior, slowly reducing their strength as a result. It can be parameterised by a simple linear factor in the quasigeostrophic equation (e.g., $D_0 q = -\kappa q$). Damping and forcing processes are needed in the description of statistically steady turbulent fluids, which we will come to later in this chapter.

From here, we drop the zero subscript on geostrophic velocities and operators when describing quasigeostrophic processes; the context of the equations will always be made clear when necessary. The h subscript is similarly dropped from vectors and operators when it is clear that we are working in a two-dimensional horizontal system. Finally, this thesis makes much use of the elegant *Jacobian notation* $J[\psi, f] \equiv \mathbf{u} \cdot \nabla f$ for advection operators. In Cartesian coordinates, the Jacobian can be written explicitly as $J[\psi, f] = \partial_x \psi \partial_y f - \partial_y \psi \partial_x f$, due to the definition of streamfunction (2.18).

Two-layer quasigeostrophy

Conceptually, it is often very useful to make a further simplification known as the *two-layer approximation*, in which the potential vorticity equation becomes

$$\partial_t q_i + J[\psi_i, q_i] = 0 \qquad i = 1, 2 \tag{2.21}$$

[2] In the derivation of the QGPV equation, the identities $(\partial_x \mathbf{u}_0) \cdot \nabla v_0 = 0$, $(\partial_y \mathbf{u}_0) \cdot \nabla u_0 = 0$ and $(\partial_z \mathbf{u}_0) \cdot \nabla((f_0^2/N^2)\partial_z \psi) = 0$, all of which can be proved with use of the streamfunction definition (2.18), are extremely helpful.

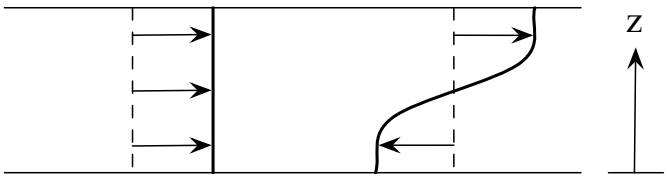

Figure 2.2: Schematic representation of the barotropic (left) and baroclinic (right) modes in the two-layer quasigeostrophic model.

with

$$\begin{aligned} q_1 &= \nabla^2\psi_1 - k_D^2(\psi_1 - \psi_2) + f_0 + \beta y \\ q_2 &= \nabla^2\psi_2 - k_D^2(\psi_2 - \psi_1) + f_0 + \beta y. \end{aligned} \tag{2.22}$$

This is physically equivalent to replacing the three-dimensional, stratified fluid described by (2.20) with two discrete layers of different densities. The parameter k_D is the internal deformation wavenumber; it tells us the relative importance of rotational and buoyancy effects. The deformation radius, $L_D = \pi k_D^{-1}$, is often a rough guide to the characteristic size of eddies that form in a turbulent quasigeostrophic fluid. We will discuss this issue further in Section 2.2.2.

We have assumed that rigid boundaries exist on the top and bottom of the fluid. This excludes the possibility of an external deformation radius appearing in (2.21) due to a movable interface (e.g., water → air) at the top or bottom layer. In both the theoretical and experimental chapters of this thesis, the systems studied always have rigid top and bottom boundaries of this kind.

With only two levels, the vertical modal decomposition of (2.21) is extremely easy. We define barotropic and baroclinic streamfunction and potential vorticity via level sums and differences,

$$\psi = \frac{1}{2}(\psi_1 + \psi_2) \tag{2.23}$$

$$\tau = \frac{1}{2}(\psi_1 - \psi_2) \tag{2.24}$$

and

$$q = \frac{1}{2}(q_1 + q_2) = \nabla^2\psi + f_0 + \beta y \tag{2.25}$$

$$\sigma = \frac{1}{2}(q_1 - q_2) = \nabla^2\tau - k_D^2\tau \tag{2.26}$$

respectively. In the two-layer system, therefore, the terms 'barotropic' and 'baroclinic' have simple interpretations as the vertical average and the vertical shear[3], as illustrated in Figure 2.2.

The dynamical equations for (2.25) and (2.26), in the absence of forcing and damping, can be written as

$$\partial_t q + \frac{1}{2}(J[\psi_1, q_1] + J[\psi_2, q_2]) = 0 \tag{2.27}$$

$$\partial_t \sigma + \frac{1}{2}(J[\psi_1, q_1] - J[\psi_2, q_2]) = 0. \tag{2.28}$$

[3]This can be contrasted with the more fundamental and general definition of a barotropic fluid as one in which pressure is a function of density only, $p = p(\rho)$.

In terms of purely modal variables, (2.27) and (2.28) become

$$\partial_t q + J[\psi, q] + J[\tau, \sigma] = 0 \tag{2.29}$$

$$\partial_t \sigma + J[\psi, \sigma] + J[\tau, q] = 0. \tag{2.30}$$

In Chapter 8, equations (2.27) and (2.28) are used to construct a reduced model of the rotating annulus experiment.

Planetary waves

Before we move on to the discussion of highly nonlinear, turbulent fluid behaviour, it is important to briefly mention the linear solutions to the QG equation. If it is assumed that there is no mean flow of any kind, and for simplicity also that there is no vertical structure ($N^2 \to \infty$), the potential vorticity equation (2.20) becomes

$$\partial_t q' + \beta \partial_x \psi' = 0 \tag{2.31}$$

If $\beta = 0$, then nothing very interesting happens. However when β is non-zero, (2.31) has wave solutions, with a Fourier transform revealing the dispersion relation

$$\omega = \frac{-\beta k_x}{k_x^2 + k_y^2}. \tag{2.32}$$

The planetary wave propagation mechanism has a very intuitive real space description, which is outlined in Figure 2.3. As we will see, planetary waves are fundamental to zonal jet formation.

2.1.2 Fluid equations in spectral form

In turbulence theory, it is often extremely useful to be able to examine a problem from a spectral space viewpoint. In spectral space, nonlinear advection terms of the type $J[\psi, q]$ transform into triad terms, describing energy exchange between the various modes of the system. In the absence of nonlinearity, the only way modes can gain or lose energy is through non-conservative effects.

Spectral transforms of fluid equations are easiest to perform in Cartesian coordinates, where simple Fourier transforms of all variables usually produce the required results. In non-Cartesian geometries, such as the experimental rotating annulus, Fourier modes are not in general eigenfunctions of the physically relevant operators, and derivation of spectral equations can become much more difficult.

In general, spectral equations are derived from real space ones by substituting in the spectrally transformed form of all variables, and then performing a further transform over the entire equation. For example, for the spatially unbounded, constant density Navier-Stokes equations, in a non-rotating frame, we can write all variables in terms of their Fourier integral coefficients, e.g.,

$$\mathbf{u}(\mathbf{x}, t) = \int \mathbf{u}(\mathbf{k}, t) e^{i\mathbf{k}\cdot\mathbf{x}} \mathrm{d}^3\mathbf{k}. \tag{2.33}$$

Writing $\mathbf{u}(\mathbf{k}, t) = \mathbf{u}_\mathbf{k}$ for brevity and substituting (2.33) into (2.1) (ignoring the conservative scalar term Φ), we arrive at

$$\frac{\partial}{\partial t} \int \mathbf{u}_\mathbf{k} e^{i\mathbf{k}\cdot\mathbf{x}} \mathrm{d}^3\mathbf{k} + \left(\int \mathbf{u}_\mathbf{l} e^{i\mathbf{l}\cdot\mathbf{x}} \mathrm{d}^3\mathbf{l} \right) \cdot \left(\int i\mathbf{m}\mathbf{u}_\mathbf{m} e^{i\mathbf{m}\cdot\mathbf{x}} \mathrm{d}^3\mathbf{m} \right)$$
$$= -\rho_0^{-1} \int i\mathbf{k} p_\mathbf{k} e^{i\mathbf{k}\cdot\mathbf{x}} \mathrm{d}^3\mathbf{k} - \nu \int |\mathbf{k}|^2 \mathbf{u}_\mathbf{k} e^{i\mathbf{k}\cdot\mathbf{x}} \mathrm{d}^3\mathbf{k}. \tag{2.34}$$

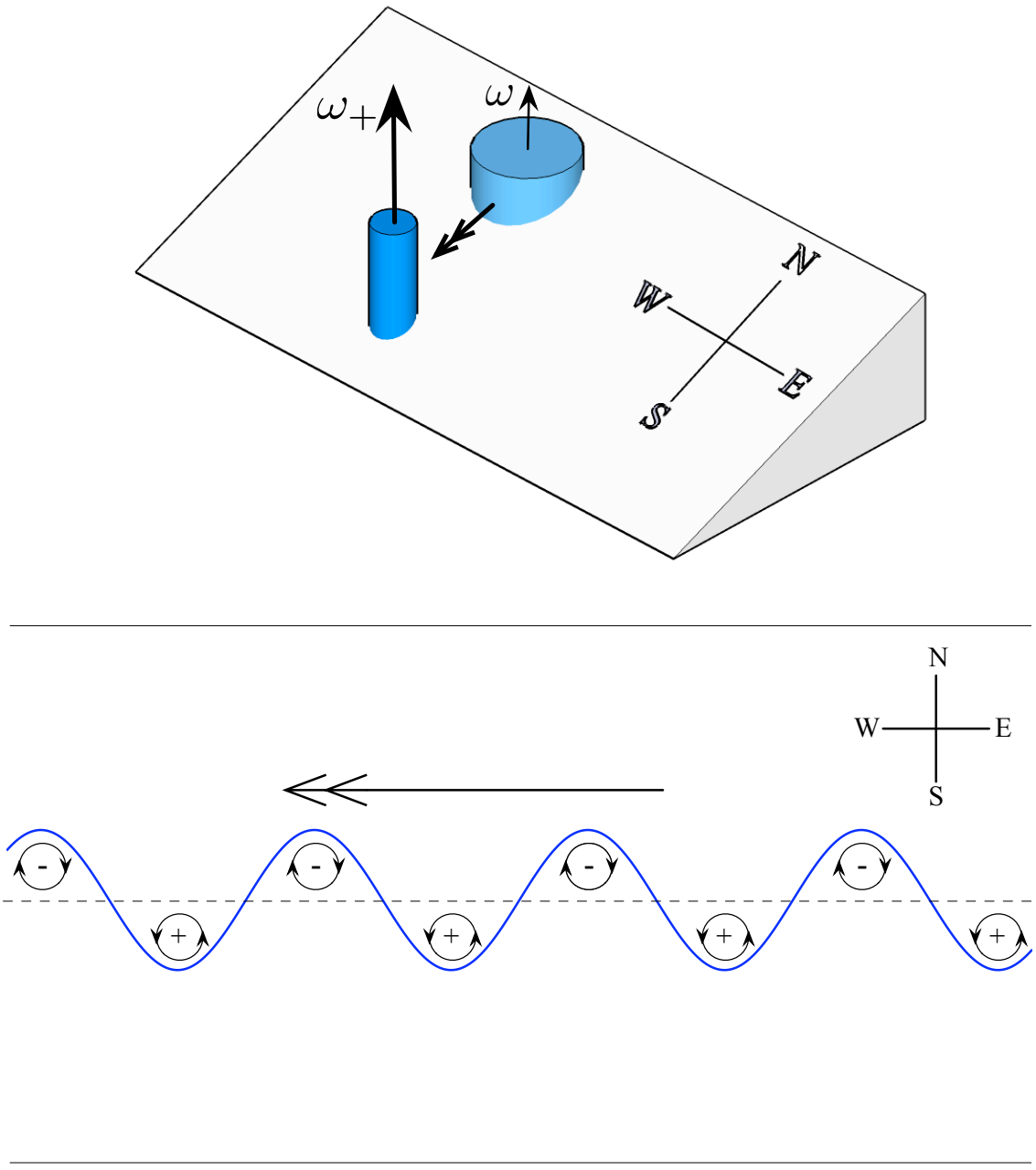

Figure 2.3: a) A vortex tube moving southwards elongates, and hence must spin up, gaining vorticity, in order to conserve angular momentum (alternatively, potential vorticity). Likewise, a vortex tube moving northwards spins down. b) If a sinusodial chain of vortex tubes is displaced latitudinally, the induced vorticity change of each tube will cause one of its neighbours to move north, and the other southwards. The motion is such that the wave will always move westward, with larger waves travelling faster, as is evident from (2.32).

If (2.34) is Fourier transformed, the definition of the $\mathbf{k}$-space δ-function

$$\delta_{\mathbf{k}} \equiv \delta(\mathbf{k}) = \frac{1}{2\pi} \int d^3\mathbf{x} e^{-i\mathbf{k}\cdot\mathbf{x}} \tag{2.35}$$

and the incompressibility condition (2.5), then allows one to derive the spectral Navier-Stokes equation

$$\frac{\partial \mathbf{u_k}}{\partial t} + \nu|\mathbf{k}|^2\mathbf{u_k} + O_{\mathbf{klm}}\mathbf{u_l}\mathbf{u_m} = 0. \tag{2.36}$$

The linear term $\nu|\mathbf{k}|^2\mathbf{u_k}$ describes viscous damping in spectral space. The function $O_{\mathbf{klm}}$ is a *triad operator*, coupling triplets of modes together that satisfy the resonance criterion $\mathbf{k} = \mathbf{l} + \mathbf{m}$. Its exact form here is

$$O_{\mathbf{klm}}\mathbf{u_l}\mathbf{u_m} = i \int\int \delta_{\mathbf{k=l+m}} \mathrm{d}^3\mathbf{l}\mathrm{d}^3\mathbf{m} \left(\mathbf{u_m}(\mathbf{u_l}\cdot\mathbf{m}) - \frac{\mathbf{k}}{|\mathbf{k}|^2}(\mathbf{u_m}\cdot\mathbf{l})(\mathbf{u_l}\cdot\mathbf{m}) \right) \tag{2.37}$$

with each integral over three-dimensional spectral space [58].

A similar method can be used to derive spectral equations for the two-layer quasigeostrophic equation (2.21). Here the derivation is slightly easier, however, as all dynamical variables are scalars. Following the same method as for the Navier-Stokes case, the resulting equations are

$$\begin{aligned} \frac{\partial \zeta_{\mathbf{k}}}{\partial t} + i\omega_{1\mathbf{k}}\zeta_{\mathbf{k}} + A_{\mathbf{klm}}\zeta_{\mathbf{l}}\zeta_{\mathbf{m}} + B_{\mathbf{klm}}\sigma_{\mathbf{l}}\sigma_{\mathbf{m}} &= 0 \\ \frac{\partial \sigma_{\mathbf{k}}}{\partial t} + i\omega_{2\mathbf{k}}\sigma_{\mathbf{k}} + C_{\mathbf{klm}}\sigma_{\mathbf{l}}\zeta_{\mathbf{m}} &= 0 \end{aligned} \tag{2.38}$$

where $\zeta_{\mathbf{k}} = -|\mathbf{k}|^2\psi_{\mathbf{k}}$ and $\sigma_{\mathbf{k}} = -(|\mathbf{k}|^2 + k_D^2)\tau_{\mathbf{k}}$. The linear response terms $\omega_{1\mathbf{k}}$ and $\omega_{2\mathbf{k}}$ are simply the frequencies of barotropic and baroclinic planetary waves

$$\begin{aligned} \omega_{1\mathbf{k}} &\equiv \frac{-\beta k_x}{|\mathbf{k}|^2} \\ \omega_{2\mathbf{k}} &\equiv \frac{-\beta k_x}{|\mathbf{k}|^2 + k_D^2}. \end{aligned} \tag{2.39}$$

The form of the triad operators in (2.38) is

$$\begin{aligned} A_{\mathbf{klm}} &= \int\int \delta_{\mathbf{k=l+m}} \mathrm{d}^2\mathbf{l}\mathrm{d}^2\mathbf{m} \frac{J[\mathbf{l},\mathbf{m}]}{|\mathbf{l}|^2} \\ B_{\mathbf{klm}} &= \int\int \delta_{\mathbf{k=l+m}} \mathrm{d}^2\mathbf{l}\mathrm{d}^2\mathbf{m} \frac{J[\mathbf{l},\mathbf{m}]}{|\mathbf{l}|^2 + k_D^2} \\ C_{\mathbf{klm}} &= \int\int \delta_{\mathbf{k=l+m}} \mathrm{d}^2\mathbf{l}\mathrm{d}^2\mathbf{m} \left(\frac{1}{|\mathbf{l}|^2 + k_D^2} - \frac{1}{|\mathbf{m}|^2} \right) J[\mathbf{l},\mathbf{m}] \end{aligned} \tag{2.40}$$

with each integral now over two-dimensional spectral space.

Wave turbulence theory

If a flow is only weakly turbulent, the nonlinear triad coupling term will be small and linear wave motion and / or damping will dominate. In this limiting case, the dynamical fields can be expanded

in terms of some dimensionless parameter λ that characterises the smallness of the nonlinear term, e.g.,

$$\psi_{\mathbf{k}} \approx \psi^0_{\mathbf{k}} + \lambda\psi^1_{\mathbf{k}} + \lambda^2\psi^2_{\mathbf{k}} + \dots . \tag{2.41}$$

In the case of planetary wave interaction, for example, λ could be a Rossby number written in terms of β, $\lambda = 1/\beta LT$, with L and T characteristic length and time scales, respectively. The expansion can be truncated at low order (or possibly renormalised), allowing the derivation of a reduced, simplified set of spectral equations. This is the basis of *resonant wave interaction theory.*

In resonant wave interactions, both the wavevectors *and* the frequencies of the interacting modes must match up for triad coupling to occur. Incidentally, this is closely analogous to the way in which interactions between sub-atomic particles must conserve both momentum and energy. For barotropic planetary waves interactions, for example, the constraints

$$\mathbf{k} = \mathbf{l} + \mathbf{m} \tag{2.42}$$

$$\omega_{\mathbf{k}} = \omega_{\mathbf{l}} + \omega_{\mathbf{m}} \qquad \rightarrow \qquad \frac{k_x}{|\mathbf{k}|^2} = \frac{l_x}{|\mathbf{l}|^2} + \frac{m_x}{|\mathbf{m}|^2} \tag{2.43}$$

will apply to triad selection.

These constraints have important consequences for the way in which waves, jets and turbulence interact in quasigeostrophic fluids. In particular, if we take one of the modes in the triads to be zonal (i.e., k_x, l_x or $m_x = 0$), then it may be shown by combining (2.42) and (2.43), and studying the form of the first triad operator in (2.40), that triad interactions between small amplitude planetary waves *cannot transfer energy to zonal modes* [36]. To understand jet formation, therefore, we must either study wave-wave interactions at higher order [41], or employ theoretical methods that do not focus solely on spectral interactions.

As we will see in the next section, the spectral view of fluid dynamics can be extremely powerful, and historically it has been dominant in terms of making observational predictions. However, it does have major disadvantages, particularly when the system of interest is highly anisotropic, as is the case for planetary-scale turbulence. Indeed, it is the view of this author that a rigid interpretation of fluid dynamics as spectral dynamics can severely limit one's ability to predict complex flow behaviour. Hence, one of the driving motivations for the work in the theoretical section of this thesis (Chapters 3 and 4) has been to combine the advantages of real space and spectral viewpoints in one dynamical framework.

2.2 The behaviour of turbulent fluids

Ask even a child to tell you whether or not a particular flow is turbulent and they will be able to answer very quickly. Defining *mathematically* what we mean by turbulence, however, is much more difficult. Lewis Fry Richardson, a pioneer in the development of fluid dynamics, sociology and many other fields, famously resorted to poetry to express his understanding of turbulent fluid motion:

Big whorls have little whorls
That feed on their velocity,
And little whorls have lesser whorls
And so on to viscosity.

Short as it is, this little limerick is actually rather brilliant, as it gets right to the heart of what turbulence in three dimensions is all about.

Consider the classic three-dimensional turbulence problem, where a non-rotating fluid with low viscosity is forced at large scales. This can be achieved, for example, by interrupting a laminar flow with a wire grid. Large-scale structures (i.e., 'big whorls') will barely feel the effects of viscosity (recall the factor of $|\mathbf{k}|^2$ in the viscous term in (2.36)). However, nonlinear triad interactions between wavenumbers can cause the exchange of kinetic energy between scales[4]. In particular, it can allow little whorls to feed on bigger ones, transferring energy to progressively smaller scales where it can eventually be dissipated by viscous effects.

If we assume that the turbulent fluid is forced with a constant energy input, then it is reasonable to imagine that in a *statistically* steady state this input will equal the power lost at the smallest scales to viscous dissipation (kinetic $\rightarrow$ thermal energy). If we also make the much more drastic assumption that *energy exchange occurs mainly between eddies of similar wavenumber*, we may hypothesise that locally, the total energy depends only on the wavenumber and the rate at which energy is moving to smaller scales.

Simple scaling analysis then tells us that in this so-called 'inertial range' where nonlinear interactions dominate, the dependence of time-averaged kinetic energy on absolute wavenumber $|\mathbf{k}| = k$ must be

$$E(k) = [L]^3[T]^{-2} = C\mathcal{E}^{2/3}k^{-5/3}, \tag{2.44}$$

where $\mathcal{E}$ is the energy input rate and C is hypothesised to be a universal constant. Equation (2.44) was first suggested by the Russian mathematician Andrey Kolmogorov in 1941, based on a heuristic argument similar to that given here [33]. It has now been verified by a large body of extremely careful experiments and idealised computer simulations. Despite its predictive successes, however, (2.44) is not a theorem; it has never been successfully derived from the Navier-Stokes equations. To many researchers, this epitomises the central problem of turbulence.

[4]Technical note: in this and following sections, we use the terms 'wavenumber' and (inverse) 'scale' more or less interchangeably. When the flows in question are isotropic, this is usually acceptable. In more general situations, however, it can lead to trouble, as the scale variation of a flow can often be strongly dependent on position. One way to get around this problem is to use phase space distributions, such as those employed in Chapters 3 and 4 of this thesis.

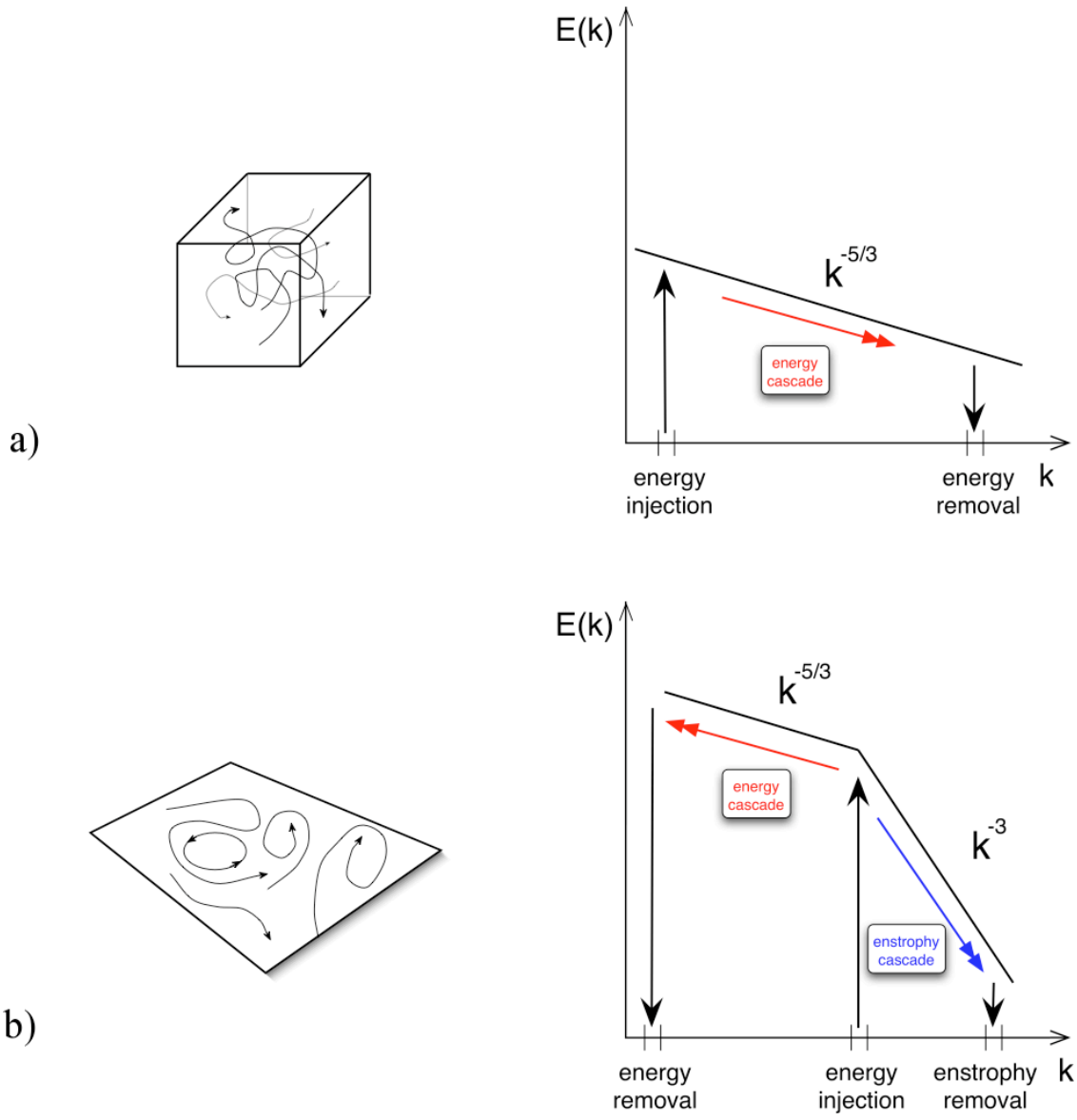

Figure 2.4: Three-dimensional turbulence in a steady state involves the transfer of energy to larger wavenumbers ($\sim$ smaller scales) b) two-dimensional turbulence in a steady state involves the transfer of energy to smaller wavenumbers, and of enstrophy to larger ones.

2.2.1 Two-dimensional turbulence

In idealised two-dimensional flows, and also in quasigeostrophic ones, the nature of turbulence is radically different to that in the three-dimensional case. This is because these flows are far more tightly constrained by conserved quantities. In a two-dimensional flow, vortex stretching is by definition impossible, and vortex tubes can only change their volume if the fluid is compressible.

Assuming incompressibility, the total *enstrophy* of the flow, defined as the integrated square of vorticity

$$Z = \int \frac{1}{2}\zeta^2 \mathrm{d}^2\mathbf{x} = \int_0^\infty Z(k)\mathrm{d}k \tag{2.45}$$

is therefore conserved in the absence of forcing and damping. On its own, this does not help very much; we simply have two conservation laws now instead of one. However, a far-reaching theorem developed by Fjørtoft in the 1950s [20] shows that the combined conservation of energy and enstrophy in a 2D fluid must dramatically alter the nature of the final flow state. By considering the nonlinear interaction between different modes on a sphere, Fjørtoft came to the conclusion that from an initial state, *the net flow of energy must always proceed to smaller wavenumbers.* His reasoning was elegantly simple, but his original proof was made more complex by the use of spherical normal modes, and the need to sum over all possible interacting triads.

A simpler, but less rigorous demonstration involves calculating the effect of energy and enstrophy conservation on a single triad interaction in plane two-dimensional geometry [58]. Let us consider three modes, with absolute wavenumbers k_1, k_2 and k_3. The total energy and enstrophy change after any nonlinear interaction must be zero. Noting that the dimensional relationship between enstrophy and energy

$$\frac{[Z]}{[E]} = \frac{[\zeta^2]}{[u^2]} = [L^{-2}] \qquad \text{implies} \qquad Z(k) = k^2 E(k) \tag{2.46}$$

both conservation laws can be written down in terms of energy

$$\begin{aligned} \delta E_{tot} &= \delta E_1 + \delta E_2 + \delta E_3 = 0 \\ \delta Z_{tot} &= k_1^2 \delta E_1 + k_2^2 \delta E_2 + k_3^2 \delta E_3 = 0, \end{aligned} \tag{2.47}$$

where of course δE_1 is the energy change for the 1st mode and so on. Eliminating the intermediate energy change δE_2 we find

$$\frac{\delta E_3}{\delta E_1} = \frac{k_1^2 - k_2^2}{k_2^2 - k_3^2}. \tag{2.48}$$

Equivalently, we can write both conservation laws in terms of enstrophy and derive

$$\frac{\delta Z_3}{\delta Z_1} = \left(\frac{k_3^2}{k_1^2}\right) \frac{k_1^2 - k_2^2}{k_2^2 - k_3^2}. \tag{2.49}$$

Equations (2.48) and (2.49) fundamentally constrain the flow of energy in the triad interactions. If, for example, $k_1 = 2k_2 = 3k_3$, then

$$\frac{\delta E_3}{\delta E_1} = \frac{27}{5} > 1 \tag{2.50}$$

$$\frac{\delta Z_3}{\delta Z_1} = \frac{3}{5} < 1. \tag{2.51}$$

It may be shown that whatever values for k_1, k_2 and k_3 are chosen, the net energy transfer is always to lower wavenumbers. Fjørtoft's theorem is one of the most remarkable results in fluid dynamics, as it implies that from an extremely nonlinear system with random initial conditions, energy must move to larger-scale structures, which will eventually dominate the fluid motion. Conversely, enstrophy moves downscale, where it must eventually experience dissipation in a real fluid.

It is worth noting what the theorem does not tell us; namely anything about the eventual result of the upscale energy transfer. It speaks only about one triad exchange, which by construction is at a scale where any energy removal or input is negligible. To assess what happens elsewhere, particularly at very low wavenumbers, more physics would need to be included.

The energy spectrum for two-dimensional flow can be predicted from these results in a rather ad-hoc way. If it is assumed that energy injection into the system occurs at a single value $k = k_{in}$, Fjørtoft's analysis shows that energy will travel upscale to lower k values, while enstrophy will travel downscale. Therefore it can be argued that if there is a large separation in k-space between energy injection and dissipation of enstrophy, the energy spectrum will effectively divide into two regimes; a low wavenumber one determined by the rate of energy injection $\mathcal{E}$, and a high wavenumber one determined by the rate of enstrophy dissipation, η. Assuming a δ-function input of energy at k_{in} and using more dimensional analysis, the energy spectrum can then be constructed piecewise

$$E(k) = \begin{cases} E_1(k) = C_1 \mathcal{E}^{2/3} k^{-5/3} & k < k_{in} \\ E_2(k) = C_2 \eta^{2/3} k^{-3} & k > k_{in} \end{cases} \tag{2.52}$$

A comparison between the 3D and 2D spectral predictions is given in Figure 2.4.

Two-dimensional turbulence is a step closer to the reality of large-scale planetary atmospheric and oceanic motion, because the stratification and rotation effects described in Section 2.1 cause vortex columns to align themselves in the vertical direction. However, several major differences exist that cause qualitatively different behaviour in the planetary case. The two most important of these are the β-effect, and vertical flow structure due to processes like baroclinic instability. We focus on the latter in the next section.

2.2.2 Two-layer quasigeostrophic turbulence

In this section, we examine triad interactions in the two-layer, f-plane ($\beta = 0$) quasigeostrophic model and see how inclusion of the baroclinic mode affects the steady-state properties of the fluid. The problem is one that was first examined by Rick Salmon in 1978 [57], and represents the simplest possible situation that still includes some vertical structure. As the experiment described in Chapters 5-7 is baroclinically forced at large scales, his analysis is highly relevant to this thesis.

Firstly, from the definition of two-layer QG energy

$$E_{tot} = \frac{1}{2} \int \mathrm{d}^2\mathbf{x} \left(\nabla\psi_1 \cdot \nabla\psi_1 + \nabla\psi_2 \cdot \nabla\psi_2 + \frac{1}{2} k_D^2 \left(\psi_1 - \psi_2\right)^2 \right) \tag{2.53}$$

$$= \frac{1}{2} \int \mathrm{d}^2\mathbf{x} \left(\nabla\psi \cdot \nabla\psi + \nabla\tau \cdot \nabla\tau + k_D^2 \tau^2 \right) \tag{2.54}$$

it may be noted that the combined energy of the barotropic and baroclinic modes is equal to

$$\begin{aligned} E_{\mathbf{k}} &= |\mathbf{k}|^2 |\psi_{\mathbf{k}}|^2 + \left(|\mathbf{k}|^2 + k_D^2 \right) |\tau_{\mathbf{k}}|^2 \\ E_{\mathbf{k}} &= T_{\mathbf{k}} + C_{\mathbf{k}} \end{aligned} \tag{2.55}$$

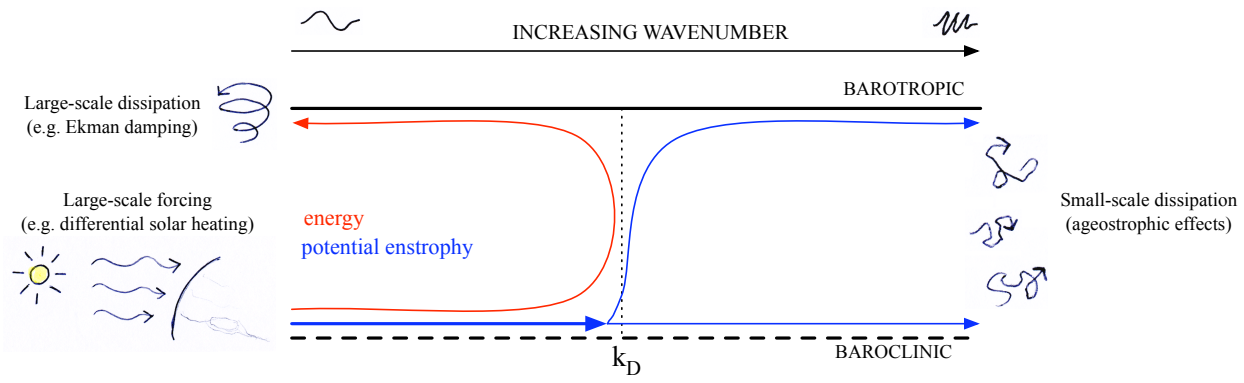

Figure 2.5: Spectral space cartoon of the energy and potential enstrophy transfers theorised to occur in the limit $k_{forcing} << k_D << k_{ageostrophic}$.

for any given horizontal wavenumber $\mathbf{k}$.

In the 2D turbulence case we have just considered, potential vorticity is simply ordinary (Eulerian) vorticity, so it is natural that enstrophy, the square of vorticity, is also conserved. By analogy, for the two-layer model we can define *potential* enstrophy

$$\begin{aligned} Z_{\mathbf{k}} &= |\mathbf{k}|^4 |\psi_{\mathbf{k}}|^2 + \left(|\mathbf{k}|^2 + k_D^2\right)^2 |\tau_{\mathbf{k}}|^2 \\ Z_{\mathbf{k}} &= |\mathbf{k}|^2 T_{\mathbf{k}} + \left(|\mathbf{k}|^2 + k_D^2\right) C_{\mathbf{k}} \end{aligned} \tag{2.56}$$

and see that in any two-layer triad interaction, both energy and potential enstrophy must be conserved.

Now from (2.38), it is obvious that there are two types of triad interaction permitted:

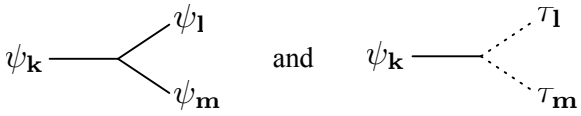

Three barotropic modes can exchange energy with each other, or one barotropic mode can exchange with two baroclinics. The restriction to only two interaction types can be seen as a direct consequence of vertical wavenumber conservation — a barotropic mode has $m = 0$, while the single baroclinic mode in the two-layer model has $m = \pm 1$. The efficiency of energy exchange between modes will depend on the ratio of each of their wavevectors to the deformation wavenumber, $|\mathbf{k}|^2/k_D^2$.

In [57], Salmon carried out a detailed analysis of the steady-state solution to this problem. Careful consideration of non-conservative effects (forcing and damping) along with the crucial assumption of irreversibility, led to some very interesting conclusions about the direction of energy flow in spectral space. His result, which still dominates thinking on the baroclinic turbulence problem today, can be neatly summarised in diagrammatic form (Figure 2.5). If baroclinic forcing is large-scale, as is the case for the differentially heated annulus experiment, the Earth's atmosphere, and at least partially also for the gas giant planets, energy is initially transferred to larger baroclinic wavenumbers ($\sim$ smaller-scale structures). When it hits the deformation wavenumber, transfer to

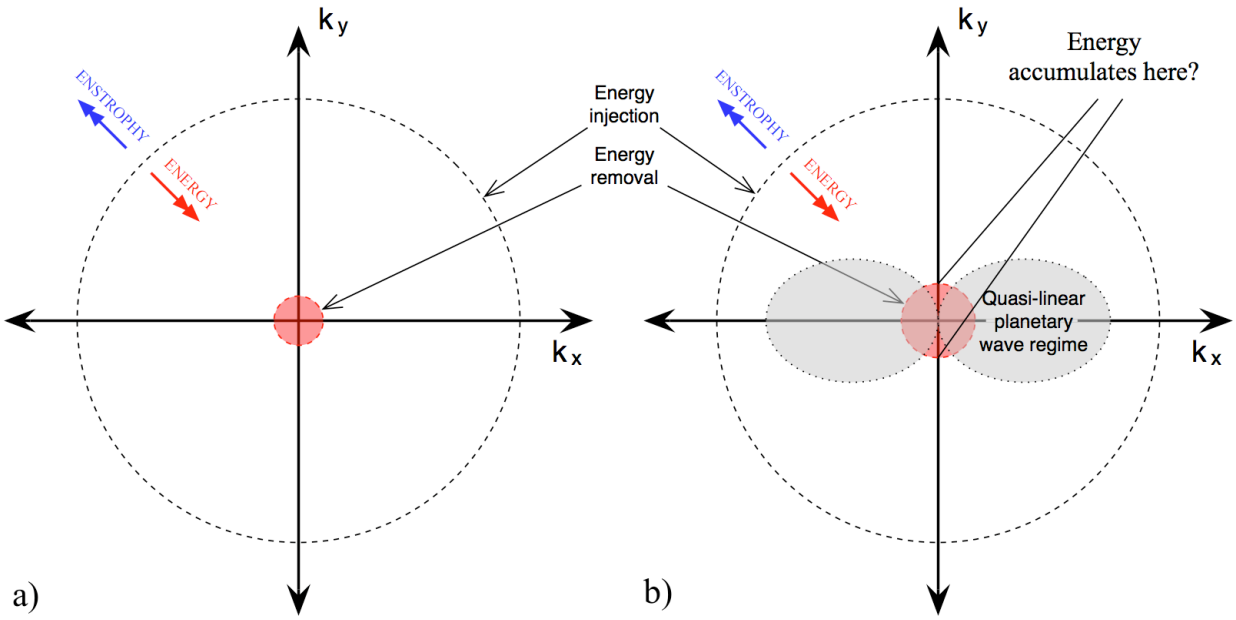

Figure 2.6: The spectral view of β-plane jet formation.

the quasi-2D barotropic modes becomes effective. If the separation of scales is large enough, it might then be expected that the barotropic part will only 'see' forcing at the deformation radius scale, and hence will behave similarly to the 2D turbulent flow described in the previous section. In particular, it is generally expected that a *barotropic* inverse cascade will still transfer kinetic energy from small to large scales.

Note that this argument critically depends on three assumptions. First, it is assumed that the flow is in a statistically steady state. Second, some form of large-scale damping is required to remove energy from the barotropic field. The third and most serious assumption is that there is a well-defined separation between the forcing scale and deformation radius. In many real situations, including the atmospheres of Earth and the gas giant planets, this separation is not particularly distinct.

In Chapter 6, it will be seen to just what extent these classical turbulence ideas hold in a real laboratory experiment.

2.2.3 Turbulence on a β-plane

The final heuristic description we wish to consider is that of barotropic turbulence on a β-plane (or, more generally, a rotating sphere). This problem was first tackled by Peter Rhines in 1975 [54]. In a seminal paper, Rhines argued that the 'inverse cascade' of two-dimensional turbulence (see Figure 2.4) would be modified at low wavenumbers by the presence of planetary waves.

He used scale analysis to define an eddy turnover time

$$\tau_{eddy} \equiv \frac{1}{\sqrt{\int k^2 E(k) \mathrm{d}k}} \approx \frac{1}{U_{rms}|\mathbf{k}|} \tag{2.57}$$

and argued that when this is larger than the planetary wave period, triad interactions will be inhibited by the waves, effectively halting the cascade. Given that the barotropic planetary wave dispersion relation in the absence of large zonal flow is (2.32), this appears to mean that cascade interaction will be prohibited in a dumbbell shaped region of **k**-space, with the boundary given by

$$k_x \propto \pm|\mathbf{k}|^3. \tag{2.58}$$

If large-scale friction (an essential part of the spectral view of jet formation) is included, a steady state may be reached, in which energy tends to collect in modes that satisfy $k_x = 0$, $k_y =$ small but not zero (i.e., zonal modes). These ideas are illustrated schematically in Figure 2.6.

Rhines also predicted from scale analysis that the characteristic width of the zonal flow (equivalently, of the jets) would be of order

$$L_\beta = \sqrt{\frac{U_{rms}}{\beta}}. \tag{2.59}$$

As it is derived from a combination of fundamental system parameters, the *Rhines scale*, as it has become known, is often of importance in determining the steady-state jet width of natural and experimental systems. However, its usefulness is somewhat limited, as U_{rms} is not a fundamental parameter; it is only known after the fluid is in a steady state.

Insightful as it was, Rhines' work, like all the theories expounded in this section, was essentially heuristic in nature, and cannot provide a detailed dynamical explanation of the jet formation process. As a result, barotropic β-plane jet formation has been the subject of intensive numerical study by many researchers (e.g., [12], [31], [68]). One particularly important study was that of Vallis and Maltrud [64], who simulated decaying, unforced turbulence, and originated the 'planetary wave dumbell' concept in order to explain their results. Interestingly, however, they also suggested that there was no *a priori* justification for zonal energy to peak at the Rhines scale.

More recently, Galperin, Sukoriansky and co-workers have done much to clarify the spectral view of idealised β-plane zonal jet formation. In Sukoriansky et al. [61], with the aid of a series of long integration time computer simulations of the barotropic QG equations on a sphere, they produced an empirical theory for the observed slopes of both total and zonal energy spectra. Making use of scaling analysis, they predicted that in a certain 'zonostrophic' regime, the steady-state *zonal* energy spectrum at large scales would be modified, taking the form

$$E_z(k_y) = C_z \beta^2 k_y^{-5}. \tag{2.60}$$

They verified the existence of (2.60) in their idealised simulations, and predicted an approximate value of 0.5 for the 'universal' constant C_z. In Galperin et al. [21], they noted further properties of the idealised barotropic system, including the importance of the large-scale damping mechanism in determining the steady-state jet structure. In particular, if the damping is scale-independent, as is the case for Ekman suction, they found that zonal kinetic energy peaked at a value

$$k_{fr} \approx \left(10 C_z \frac{\kappa \beta^2}{4\mathcal{E}}\right)^{1/4}, \tag{2.61}$$

defined in terms of *external* system parameters (here κ is the Ekman damping parameter and $\mathcal{E}$ is the energy input rate as before). They showed that in the zonostrophic regime, this wavenumber was, to within a factor of $\mathcal{O}[1]$, the inverse of the Rhines scale L_β^{-1}.

Turbulence in two-layer β-plane flows

Very little theoretical work has been done on combining the results of this section and the previous one. Salmon [58] noted that the two-layer arguments are based on conservation laws and hence should survive the inclusion of a constant β-effect. As his argument is based only on conservation laws and an irreversibility principle, it does make quite unambiguous predictions, but only about the general direction of energy transfer. Further theoretical progress has proved difficult, not least because for many real flows the deformation radius is not much smaller than the observed jet width. In this situation standard cascade-type arguments, which are dependent on the existence of well-defined inertial ranges in spectral space, are of dubious validity.

Some numerical simulations of baroclinically forced turbulence have been carried out. Panetta [43] simulated two-layer β-plane turbulence in a doubly periodic domain, and found that equivalent barotropic jets with width proportional to the Rhines scale formed, with the system only reaching a steady state over a time-scale longer than that suggested by any simple combination of model parameters.

However, the computational power needed to simulate fully three-dimensional turbulent flows for long time periods mean that this problem has not been well studied in general. In particular, large uncertainties remain concerning the exact nature of energy transfer from baroclinic to barotropic modes, as well as that between eddies and the mean zonal flow. The motivation for additional studies and theoretical work clearly remains strong.

Other approaches to β-plane jet formation

Given the problems associated with a purely spectral view of turbulent jet formation, it is not surprising that many researchers have attempted to pursue other methods. Much work has been done on the subject, and no attempt to make a comprehensive review will be made here. We mention just two other avenues of research, both of which are highly relevant to the new work described in the next chapter.

The first is eddy-mean flow theory, which properly began in a planetary context with the work of Eliassen and Palm [17], and was greatly extended and generalised by Andrews and McIntyre in [3] and [4]. In this mainly real space approach, less emphasis is placed on turbulent interactions between modes. Instead, the interaction between zonal flow and 'eddies' (i.e., everything else) takes centre stage. As will be seen in the next chapter, a key part of eddy-mean flow theory is the *non-acceleration theorem*, which shows eddy motion and jet formation to be directly tied to one another.

The other approach, which has perhaps seen rather less attention to date than it deserves, is wave-kinetics. In wave-kinetic theory, the interactions of broadband systems of waves are described using the formalism first developed by Hasselmann, Zahkarov and others [24][72]. At least for weakly turbulent flows, this approach has allowed the prediction of certain flow properties, such as the slopes of energy spectra, that have not been possible using other methods.

However, previous analyses involving this approach have either ignored the mean flow entirely, or made an early assumption of spatial scale separation between mean flow and waves. Analyses involving planetary waves have also usually explored certain special cases, e.g., the limit of large zonal flow and small β-effect. Two studies of particular relevance to the next two chapters are Dyachenko et al. (1992), in which a wave-kinetic description of the interaction between large-scale vortices and small-scale planetary waves was developed, and Manin and Nazarenko (1994), where a phase space equation was used to study the interaction between scale-separated zonal flows and planetary waves in the limit of small β-effect [16][38].

In the next two chapters, the aim is to make use of the phase space view more directly than has been done in previous studies. First, a phase space planetary wave equation is derived that includes all effects of the mean flow on wave propagation. It is shown that the equation can be used to generalise previous results in real space wave-mean flow theory. Theoretical arguments, combined with phase space analysis of a numerical model, are then used to give an intuitive picture of jet formation and asymmetry in some simple wave-mean flow interaction examples.

2.3 Summary

What have we covered in this review chapter? The main results are summarised below for convenience.

- Quasigeostrophy (QG) is an approximation to the Navier-Stokes equations valid for rotating, stratified planetary-scale fluids.
- On average, kinetic energy moves to larger wavenumbers in three-dimensional turbulence. Kinetic energy moves to smaller wavenumbers and (potential) enstrophy to larger ones in two-dimensional and QG turbulence.
- In a turbulent two-layer QG fluid with large-scale baroclinic forcing, energy transfer from baroclinic to barotropic modes occurs optimally at the internal deformation wavenumber, k_D.
- When the β-effect is present, the upscale energy transfer at medium and small wavenumbers is altered by planetary wave motion. Zonal jets somehow form as a result.

As has been emphasised throughout this chapter, much of the established ideas on turbulent fluid motion are heuristic, based as they are on scale analysis and intuitive guesses. Cascade theory does a fairly good job of predicting the slope of energy spectra in the idealised cases of three and two-dimensional isotropic turbulence. However, its ability to describe the β-plane jet formation case is limited at best. When vertical structure is included in the dynamical equations, the shortcomings of the theory become even more apparent.

Two alternative theoretical approaches are the wave-mean flow formalism of Eliassen & Palm (1961) and others, and the phase space approach of Dyachenko et al. (1992) and Manin and Nazarenko (1994). In the next two chapters, we discuss a new derivation that combines these two approaches.

Chapter 3

Phase space approach I: Theory

3.1 Overview

In this chapter, we take a phase space approach to the problem of planetary wave – zonal flow interaction. The aim of the approach is to create a more intuitive description of jet formation than has previously been possible with conventional real and spectral space techniques. To this end, we will first be reducing the fully nonlinear equations of Chapter 2 to as simple a form as possible, without removing the parts that are essential to the phenomena we are interested in.

In Section 3.2, previous results in quasigeostrophic wave-mean flow theory, the starting point for the new approach, are briefly discussed. In Section 3.3, a quantum-mechanical tool, the Wigner distribution, is introduced and used to derive a 'quantum' Boltzmann equation that describes the transport of planetary waves in real and spectral space simultaneously. With an assumption of spatial scale separation between the planetary waves and zonal flow, a phase space transport equation is then derived that is more general than those used in other studies [16][38]. In particular, integration of the equation over wavenumber allows generalised versions of previous real space conservation laws to be derived. In Chapter 4, a simple numerical simulation will be introduced that demonstrates the utility of the phase space view in analysing wave-mean flow problems. The following two chapters are based on a paper [69] that is in preparation for publication.

3.2 Review of basic wave-mean flow theory

In this section we briefly review some of the established theoretical results on wave-mean flow interaction. For a more detailed and thorough analysis than that given here, the text [2] is recommended. As discussed in Chapter 2, the essential features of many large-scale geophysical flows can be captured by the quasigeostrophic potential vorticity (QGPV) equation

$$\frac{Dq}{Dt} = \frac{\partial q}{\partial t} + J[\psi, q] = -\kappa q \tag{3.1}$$

where ψ is the velocity streamfunction and $q = \left(\partial_{xx} + \partial_{yy} + \partial_z \left(\left(f_0^2/N^2\right)\partial_z\right)\right)\psi + \beta y$ is the quasigeostrophic potential vorticity as before.

For convenience, in this chapter we work with (3.1) in Cartesian coordinates, according to the

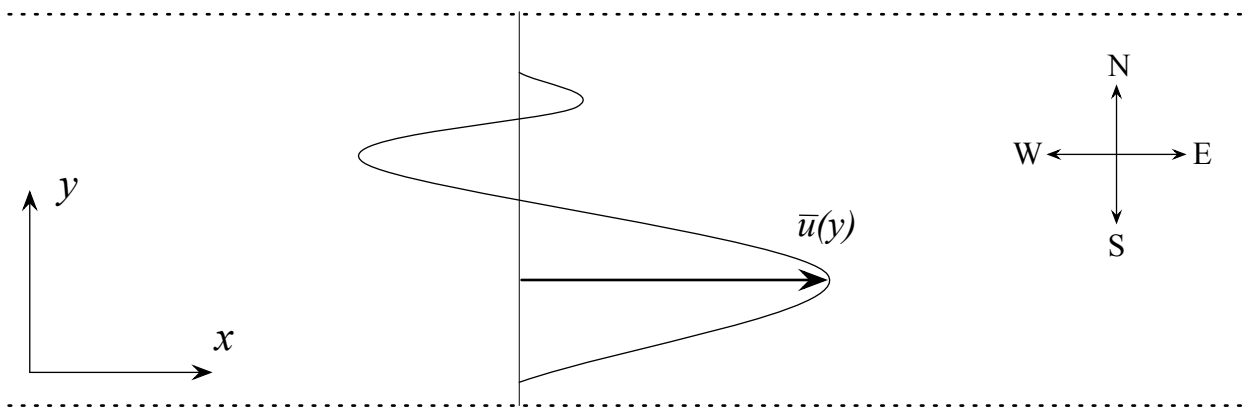

Figure 3.1: Schematic of the theoretical setup: a β-plane model periodic in the x-direction and open in the y-direction. As discussed in Chapter 2, the β-plane approximates fluid motion on the midlatitudes of a planet, with x and y equivalent to east-west and north-south directions respectively.

standard β-plane model. We also focus on the situation where the system is unbounded in the y (north-south) direction. The theoretical setup is summarised in Figure 3.1.

As discussed in Chapter 2, the linearised form of (3.1) has planetary wave solutions. With vertical structure included, the dispersion relation (2.32) becomes

$$\sigma = \frac{-\beta k_x}{k_x^2 + k_y^2 + k_z^2} \tag{3.2}$$

when no zonal flow or damping is present. In (3.2), k_z is understood to be an eigenvalue of the usual vertical structure equation such that $\partial_z \left(\left(f_0^2 / N^2 \right) \partial_z \Psi \right) = -k_z^2 \Psi$, subject to suitable boundary conditions.

As we wish to study the interaction between jets and planetary waves, it is natural to define an average in the x (east-west) direction such that any quantity decomposes into a mean flow and disturbance field: $f(\mathbf{x}, t) = \overline{f(y, z, t)} + f'(\mathbf{x}, t)$. By averaging (3.1) we can derive

$$\begin{aligned} \frac{\partial \overline{q}}{\partial t} &= -\overline{J[\psi', q']} - \kappa \overline{q} && (3.3) \\ &= -\overline{u' \partial_x q'} - \overline{v' \partial_y q'} - \kappa \overline{q} && (3.4) \\ &= -\frac{\partial}{\partial y} \overline{v' q'} - \kappa \overline{q} && (3.5) \end{aligned}$$

for the mean flow, as $\overline{J[\overline{\psi}, \overline{q}]} = 0$. The third line follows with the observation that $\partial_x u' + \partial_y v' = 0$, as u' and v' are geostrophic velocities, determined entirely by the streamfunction ψ'.

For the disturbance equation, we subtract (3.5) from (3.1) to get

$$\frac{\partial q'}{\partial t} + \overline{u} \frac{\partial q'}{\partial x} + \gamma v' = \overline{J[\psi', q']} - J[\psi', q'] - \kappa q'. \tag{3.6}$$

Here $\gamma = \partial_y \overline{q}$ is the *total* gradient of zonal potential vorticity. The left hand side of (3.6) describes the evolution of planetary waves in the presence of a zonal flow, while the right describes non-conservative effects and wave-wave interactions. As we are primarily concerned with wave-mean

flow interaction, we assume from here onwards that the wave-wave terms in (3.6) are small. In Chapter 4, where we discuss the numerical simulation of a generic jet-wave interaction problem, the situations where this assumption begins to fail will be made clear.

For moderate disturbance amplitudes, it can be shown that the *wave action*, defined as $n \equiv \frac{1}{2}\overline{q'^2}/\gamma$, is a conserved quantity. This can be seen through multiplication of (3.6) by q'/γ, which firstly results in

$$\frac{\partial n}{\partial t} + \overline{v'q'} = -2\kappa n. \tag{3.7}$$

if terms of order q'^3 and greater are neglected. If spatial scale separation between zonal flow and waves is then assumed and the waves are taken to be monochromatic, a real space transport equation for wave action can be written

$$\frac{\partial n}{\partial t} + \nabla_m \cdot (\mathbf{v}_m n) = -2\kappa n, \tag{3.8}$$

where $\nabla_m = (\partial_y, \partial_z)$ and $\mathbf{v}_m$ is the meridional (y, z) group velocity of the waves. For further details of the derivation of (3.7), see [2].

Equation (3.8) simply states that in the absence of damping ($\kappa = 0$), n is a conserved quantity that travels at the group velocity $\mathbf{v}_m$. As we will see, n can be interpreted as a density of planetary wavepackets, analogous to the density of fluid particles ρ. Thus equation (3.8) is directly analogous to (2.2), which states that *mass* is conserved and transported at the fluid velocity $\mathbf{u}$.

Note that our definition of n depends on the potential vorticity gradient, γ, remaining non-zero. If γ changes sign somewhere in the domain, it is possible that the zonal flow may be unstable. The problems associated with defining n in these cases is discussed in more detail in [44].

The final established result of importance to the rest of this chapter is the powerful *non-acceleration theorem*, which states that in the absence of forcing or damping, the rate of change of zonal potential vorticity and wave action are directly tied to each other

$$\frac{\partial}{\partial t}\left(\overline{q} - \frac{\partial n}{\partial y}\right) = 0. \tag{3.9}$$

Equation (3.9) can be proved by use of the Taylor identity [2], or by combining equations (3.5) and (3.7) and setting $\kappa = 0$. In Chapter 4, where a simple wave-mean flow numerical simulation is introduced, (3.9) will be extremely helpful for interpreting and understanding the results.

3.3 The 'quantum' Boltzmann equation

Having described the basic features of the planetary wave-mean flow problem, we now wish to extend the scope of the analysis. The aim is to construct a generalised phase space transport equation for the planetary waves, leaving any scale separation approximations until as late as possible in the derivation. As has been emphasized, phase space equations have already been used to study zonal jet formation in several previous studies. The difference here is that a) we use a new, simpler derivation that for the first time incorporates all the effects of the mean flow on the waves and b) we directly compare the scale-separated predictions with the results of a more general numerical simulation.

Perhaps the best known example of a phase space transport equation is the Boltzmann equation of classical mechanics. It describes the (smoothed) collective interaction of an ensemble of point particles in phase space, due to a field that is a function of the position of every particle. For example, in stellar dynamics, the Boltzmann equation is used to describe the motion of an ensemble of stars, with each star's motion determined by the mean gravitational field due to all the others.

In quantum mechanics, the *quantum* Boltzmann equation is needed to describe the collective interaction of an ensemble of particles. Due to the uncertainty principle, quantum particles cannot simultaneously have a well-defined position and momentum, and hence do not occupy single points in phase space.

As fluid mechanical wavepackets are not pointlike particles in phase space either, if we wish to construct a general equation for their motion, we must initially take the quantum-mechanical route. The central difference between a quantum system and a fluid one is that in the fluid case, any wavefield can be decomposed into *any number of wavepackets*, as the base packet amplitude can be chosen arbitrarily. While wave action, a *continuous* quantity analogous to wavepacket number density, is conserved, the discrete notion of 'number of wavepackets' is nonsensical, strictly speaking, in a classical fluid context.

In the case of quasilinear planetary waves, interaction can only occur indirectly through modification of the zonal flow profile. It is appropriate for this problem, therefore, to view the zonal flow as the 'mean field' through which the wavepackets couple, analogous to the gravitational field in the stellar case.

We begin the derivation of the planetary wave Boltzmann equation by writing the disturbance equation (3.6) in terms of a new variable $\phi \equiv q'/\sqrt{2\gamma}$. If we neglect terms of order ϕ^2 and higher, (3.6) then takes the form

$$i\frac{\partial \phi}{\partial t} = \hat{G}\phi, \tag{3.10}$$

where the wave operator $\hat{G}$ is defined as

$$\hat{G}[\hat{\mathbf{x}}, \hat{\mathbf{k}}, t] \equiv \sqrt{\gamma}\frac{-\hat{k}_x}{\hat{k}_x^2 + \hat{k}_y^2 + \hat{k}_z^2}\sqrt{\gamma} + \overline{u}\hat{k}_x - i\kappa \tag{3.11}$$

and the position and wavevector operators are

$$\hat{\mathbf{x}} = \mathbf{x} \qquad \text{and} \qquad \hat{\mathbf{k}} = \left(-i\partial_x, -i\partial_y, -i\sqrt{\partial_z\left(\left(f_0^2/N^2\right)\partial_z\right)}\right) \tag{3.12}$$

respectively, as we are working in a position space representation. Note that the denominator in (3.11) is simply the potential vorticity inversion operator, such that

$$-\left(\hat{k}_x^2 + \hat{k}_y^2 + \hat{k}_z^2\right)^{-1} q = \left(\partial_{xx} + \partial_{yy} + \partial_z(f_0^2/N^2)\partial_z\right)^{-1} q = \psi. \tag{3.13}$$

When scale separation *is* assumed, operators become real numbers, and the large-scale zonal flow 'sees' wavepackets as phase space points with exact values of $\mathbf{x}$ and $\mathbf{k}$. Then, (3.11) simply becomes the generalised dispersion relation for small-scale planetary waves in the presence of a zonal flow and damping

$$\hat{G}[\hat{\mathbf{x}}, \hat{\mathbf{k}}, t] \to \omega(y, z, \mathbf{k}, t) = \frac{-\gamma k_x}{k_x^2 + k_y^2 + k_z^2} + \overline{u}k_x - i\kappa. \tag{3.14}$$

To progress towards the phase space transport equation, we now need to utilise a tool from quantum mechanics: the Wigner distribution. It is defined in three dimensions as

$$\mathcal{N}_{\phi,\phi}(\mathbf{x},\mathbf{k},t) = \frac{1}{(2\pi)^3}\int_{-\infty}^{+\infty} \phi^*\left(\mathbf{x}-\frac{1}{2}\mathbf{x}_1,t\right) e^{-i\mathbf{k}\cdot\mathbf{x}_1}\phi\left(\mathbf{x}+\frac{1}{2}\mathbf{x}_1,t\right)\mathrm{d}^3\mathbf{x}_1 \tag{3.15}$$

or alternatively in spectral space as

$$\mathcal{N}_{\phi,\phi}(\mathbf{x},\mathbf{k},t) = \frac{1}{(2\pi)^3}\int_{-\infty}^{+\infty} \Phi^*\left(\mathbf{k}-\frac{1}{2}\mathbf{k}_1,t\right) e^{i\mathbf{x}\cdot\mathbf{k}_1}\Phi\left(\mathbf{k}+\frac{1}{2}\mathbf{k}_1,t\right)\mathrm{d}^3\mathbf{k}_1 \tag{3.16}$$

where $\Phi(\mathbf{k},t) = (2\pi)^{-3/2}\int_{-\infty}^{+\infty}\exp[-i\mathbf{k}\cdot\mathbf{x}]\phi(\mathbf{x},t)\mathrm{d}^3\mathbf{x}$ is the Fourier transform of ϕ. $\mathcal{N}_{\phi,\phi}$ can broadly be thought of as a phase space distribution for the function ϕ, but it has some fairly weird properties — not least of which being that it can take *negative* values. However, its projections onto real and spectral space are always positive-valued.

As an example, let us examine the simple wavepacket function

$$\phi(y) = e^{-((y-y_0)/\Delta y)^2 + il_0 y} \tag{3.17}$$

In this case, the Wigner function only varies in (y,k_y) space, where it takes the form

$$\begin{aligned}\mathcal{N}_{\phi,\phi}(y,k_y) &= \frac{1}{2\pi}\int_{-\infty}^{+\infty}\phi^*\left(y-\frac{1}{2}y_1\right)e^{-ik_y y_1}\phi\left(y+\frac{1}{2}y_1\right)\mathrm{d}y_1 &(3.18)\\ &= \left(\Delta y/\sqrt{2\pi}\right)e^{-2((y-y_0)/\Delta y)^2-((k_y-l_0)\Delta y)^2/2} &(3.19)\end{aligned}$$

i.e., that of a two-dimensional gaussian. Both $\phi(y)$ and $\mathcal{N}_{\phi,\phi}(y,k_y)$ for this example are plotted in Figure 3.2, along with the Fourier transform amplitude $|\Phi(k_y)|$.

By taking a time derivative of (3.15) and using (3.10), we may write

$$i\frac{\partial\mathcal{N}_{\phi,\phi}}{\partial t} = \mathcal{N}_{-\hat{G}\phi,\phi} + \mathcal{N}_{\phi,\hat{G}\phi}. \tag{3.20}$$

Then, by defining the *phase space* operators $\hat{\mathbf{X}} = \mathbf{x} + \frac{i}{2}\nabla_{\mathbf{k}}$ and $\hat{\mathbf{K}} = \mathbf{k} - \frac{i}{2}\nabla_{\mathbf{x}}$ (see e.g., [63]) and noting that

$$\hat{\mathbf{X}}\mathcal{N}_{\phi,\phi} = \mathcal{N}_{\phi,\hat{\mathbf{x}}\phi} \qquad \hat{\mathbf{K}}\mathcal{N}_{\phi,\phi} = \mathcal{N}_{\phi,\hat{\mathbf{k}}\phi}, \tag{3.21}$$

and hence clearly

$$\hat{\mathbf{X}}^n\mathcal{N}_{\phi,\phi} = \mathcal{N}_{\phi,\hat{\mathbf{x}}^n\phi} \qquad \hat{\mathbf{K}}^n\mathcal{N}_{\phi,\phi} = \mathcal{N}_{\phi,\hat{\mathbf{k}}^n\phi}, \tag{3.22}$$

the fairly weak assumption that $\hat{G}[\hat{\mathbf{X}},\hat{\mathbf{K}},t]$ can be expanded in powers of the two operators $\hat{\mathbf{X}}$ and $\hat{\mathbf{K}}$ allows us to arrive at

$$i\frac{\partial\mathcal{N}_{\phi,\phi}}{\partial t} = \left(\hat{G}[\hat{\mathbf{X}},\hat{\mathbf{K}},t] - \hat{G}^*[\hat{\mathbf{X}},\hat{\mathbf{K}},t]\right)\mathcal{N}_{\phi,\phi}. \tag{3.23}$$

Equation (3.23) is the 'quantum' Boltzmann equation, describing the transport of planetary wave action in phase space. Although it does not depend on any assumption of scale separation between

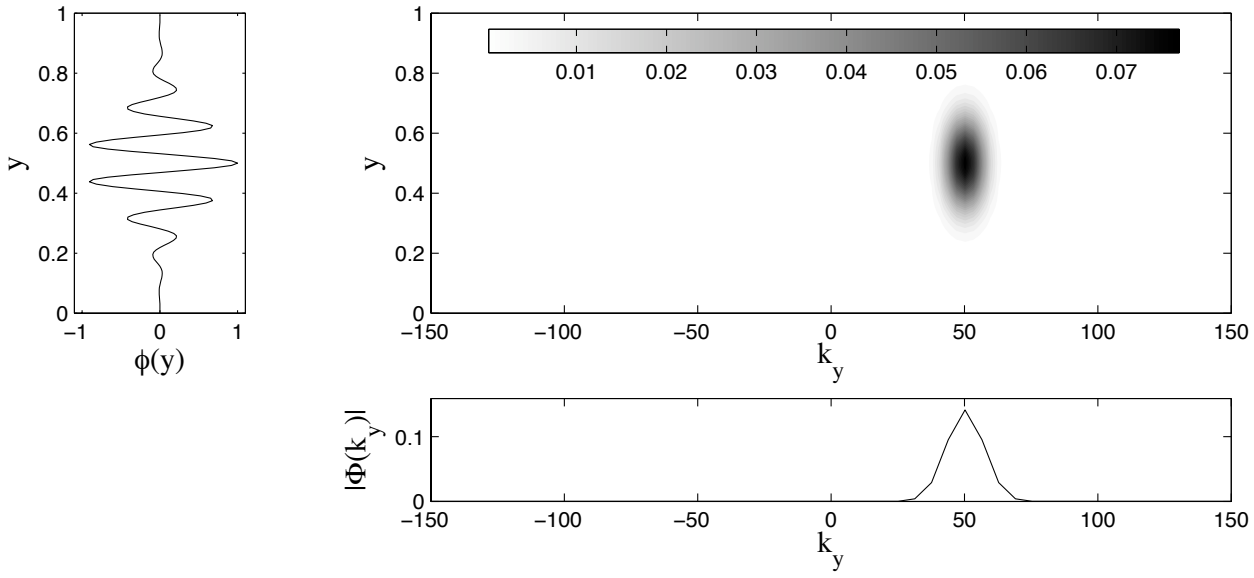

Figure 3.2: A real space function $\phi(y)$ (left), its normalised Fourier power spectrum $|\Phi(k_y)|$ (bottom right) and the magnitude of the associated Wigner distribution $\mathcal{N}_{\phi,\phi}$ (top right). In this example $l_0 = 50$, $y_0 = 0.5$ and $\Delta y = 0.2$.

zonal flow and waves, we can easily show that it reduces to a more familiar Boltzmann[1] equation via a Taylor expansion of the operator $\hat{G}$ about $\mathbf{x}$ and $\mathbf{k}$. Truncation of the Taylor expansion at first order allows us to write

$$\hat{G}[\hat{\mathbf{X}}, \hat{\mathbf{K}}, t] \approx \omega(\mathbf{x}, \mathbf{k}, t) + \frac{\partial \omega}{\partial \mathbf{x}} \cdot \frac{i}{2} \frac{\partial}{\partial \mathbf{k}} - \frac{\partial \omega}{\partial \mathbf{k}} \cdot \frac{i}{2} \frac{\partial}{\partial \mathbf{x}}. \tag{3.24}$$

A similar expansion for $\hat{G}^*[\hat{\mathbf{X}}, \hat{\mathbf{K}}, t]$ and substitution into (3.23) then leads to

$$\frac{\partial \mathcal{N}}{\partial t} + \mathbf{v} \cdot \frac{\partial \mathcal{N}}{\partial \mathbf{x}} + \mathbf{F} \cdot \frac{\partial \mathcal{N}}{\partial \mathbf{k}} = \Gamma[\mathcal{N}] \tag{3.25}$$

where $\mathbf{v}$ and $\mathbf{F}$, the group velocity of, and force on, a wavepacket respectively, have their usual definitions as $\mathbf{v} = \nabla_{\mathbf{k}} \omega$ and $\mathbf{F} = -\nabla_{\mathbf{x}} \omega$. For brevity, we write $\mathcal{N} \equiv \mathcal{N}_{\phi,\phi}$ from here.

Equation (3.25) is equivalent to (3.23) in the geometric optics limit of small-scale disturbances[2]. It describes the collective motion of an ensemble of point-like wavepackets through phase space. The right hand side of (3.25) contains all nonconservative terms: according to our derivation, $\Gamma[\mathcal{N}] = -2\kappa\mathcal{N}$. However, if the effects of wave-wave interactions were to be included, Γ would also contain more complicated terms describing collisions between wavepackets. For the general case of planetary waves on an arbitrary zonal flow, these terms are not known. They have been derived, however, for small-scale planetary waves in the *absence* of zonal flow by Reznik [53]. As the interaction between waves and zonal flow is our main interest here, we stick to the case where wave-wave terms can be neglected.

[1]Note that when $\kappa = 0$, (3.25) is conservative, and is more commonly referred to as a *Vlasov* equation.

[2]In other studies, the set of simplifications that lead to geometric optics is often referred to as the *WKBJ approximation* (e.g., [2][63]). However, precise definitions of the WKBJ limit vary. For simplicity, therefore, we only use the term 'scale-separation' to refer to the Taylor expansion that reduces (3.25) to (3.23) here.

For later use, we note that for small-scale planetary waves, we can differentiate (3.14) to obtain group velocities and rates of change of wavenumber or 'forces'

$$\begin{aligned} \mathbf{v} &= \frac{d\mathbf{x}}{dt} = \left(-\frac{\gamma}{|\mathbf{k}|^2} + \overline{u} + \frac{2\gamma k_x^2}{|\mathbf{k}|^4}, \frac{2\gamma k_x k_y}{|\mathbf{k}|^4}, \frac{2\gamma k_x k_z}{|\mathbf{k}|^4} \right) \\ \mathbf{F} &= \frac{d\mathbf{k}}{dt} = \left(0, \frac{k_x}{|\mathbf{k}|^2}\frac{\partial \gamma}{\partial y} - k_x \frac{\partial \overline{u}}{\partial y}, \frac{k_x}{|\mathbf{k}|^2}\frac{\partial \gamma}{\partial z} - k_x \frac{\partial \overline{u}}{\partial z} \right), \end{aligned} \tag{3.26}$$

where we have written $|\mathbf{k}|^2 = k_x^2 + k_y^2 + k_z^2$ etc. Note finally that if we define the wave action n (see equation (3.7)) to be the projection of $\mathcal{N}$ onto (y, z) real space

$$n(y, z, t) \equiv \overline{\int_{-\infty}^{+\infty} \mathcal{N}(\mathbf{x}, \mathbf{k}, t) \mathrm{d}^3\mathbf{k}}, \tag{3.27}$$

we can recover the results of standard wave-mean flow theory outlined in Section 3.2. By integrating (3.25) over $\mathbf{k}$, making use of the fact that $\nabla_{\mathbf{x}} \cdot \mathbf{v} + \nabla_{\mathbf{k}} \cdot \mathbf{F} = 0$ and assuming that $\mathcal{N} \to 0$ as $|\mathbf{k}| \to \infty$, we arrive at

$$\frac{\partial n}{\partial t} + \nabla_m \cdot (\langle \mathbf{v}_m \rangle n) = -2\kappa n, \tag{3.28}$$

where

$$\langle \mathbf{v}_m \rangle \equiv \frac{1}{n} \overline{\int_{-\infty}^{+\infty} \mathbf{v} \mathcal{N} \mathrm{d}^3\mathbf{k}} \tag{3.29}$$

is the phase space averaged (y, z) group velocity for the planetary waves. Equation (3.28) is a generalisation of (3.8) to a broadband distribution of small-scale waves. It is interesting to note that its derivation from (3.25) is directly analogous to the derivation of the equation of continuity (2.2) from the Boltzmann equation in fundamental fluid dynamics.

3.4 Discussion

In this chapter we have derived basic theoretical results necessary for the phase space approach to understanding jet formation. Starting from standard wave-mean flow theory, we have used the Wigner distribution to describe a broadband ensemble of planetary waves as a continuous ensemble of wavepackets. In the limit of small-scale waves and large-scale zonal flow, we have shown that the derived quantum Boltzmann equation (3.23) reduces to a transport equation of the same basic form as those used in other studies (e.g., [16]).

The analysis presented here generalises previous work on the subject in several ways. First, use of the Wigner distribution allows (3.25) to be derived in a systematic and rigorous way, and makes clearer the interesting links between wave-mean flow theory and quantum mechanics. Second, use of the variable $\phi \equiv q'/\sqrt{2\gamma}$ ensures the correct form for the phase space wave action density, $\mathcal{N}$, allowing previous real space wave-mean flow results to be derived directly from the planetary Boltzmann equation. The analyses of [16] and others, where the equation was derived by an entirely different method, neglected the important contribution of the zonal flow to the total potential vorticity gradient γ.

The main limitation of the analysis in this chapter has been the restriction to wave-mean flow interactions only. Wave-wave and turbulent interactions can play a very important role in the overall development of fluid flows on the β-plane, and any eventual general theory should aim to

take them into account. To this end, it would be most interesting in future work to extend phase space analysis techniques to a study of more strongly nonlinear planetary-scale turbulence.

As a first step, such a study would require the derivation of a Boltzmann equation for fully coupled planetary waves in the presence of an arbitrary zonal flow. As discussed in [38], there are difficulties involved in this, as a standard derivation requires knowledge of the planetary wave normal modes, which for the general disturbance equation (3.6) have never been derived analytically. However, progress could perhaps be made for scale-separated waves by deriving a fully nonlinear quantum Boltzmann equation, and carrying out the expansion (3.24) to second order.

Chapter 4

Phase space approach II: Numerical simulation

Never make a calculation until you know the answer.
—John Archibald Wheeler

In this chapter, we introduce a simple wave-mean flow numerical simulation that allows us to test the validity of the Boltzmann equation derived in Chapter 3. The aim of this chapter is to explore the phase space behaviour of planetary waves using a series of simple and idealised examples. First, the linear features of wavepacket propagation on a β-plane are explored and understood. Then, some more interesting situations involving wave-mean flow interaction are introduced. When we begin to consider these quasilinear examples, it will be seen that jet formation emerges very naturally as a result of the motion of wavepackets in phase space.

4.1 Model setup

The essential features of the wave-mean flow problem can be captured by restricting the planetary wavefield to a single x-wavenumber, $k_x = k_0$, but allowing it to be broadband in k_y. This is justified by noting that according to (3.26), the zonal mean flow cannot move planetary wavepackets to different k_x and also that in a wave-mean flow context, their x-position is clearly irrelevant. For simplicity, in this chapter we also restrict the model to the single layer barotropic case, although it should be noted that all of the theory presented in the previous section is also applicable to mixed barotropic / baroclinic flows, which in general will vary with height as well as latitude and longitude. In Chapter 8, the numerical model described here is extended to two layers, in order to model the results of the rotating annulus experiment described in the next two chapters.

For barotropic planetary waves, only the y and k_y dimensions of phase space are of relevance. In particular, the equation for phase space velocity vectors (3.26) simplifies to the two components

$$v_y = \frac{2\gamma k_x k_y}{|\mathbf{k}|^4}, \qquad F_y = \frac{k_x}{|\mathbf{k}|^2}\frac{\partial \gamma}{\partial y} - k_x \frac{\partial \overline{u}}{\partial y}. \tag{4.1}$$

To investigate equations (3.5) and (3.6) numerically, we write the disturbance vorticity as $q' =$

$\mathrm{Re}[Q(y)e^{ik_0x}]$. This allows the derivation of the simplified equations

$$i\frac{\partial Q}{\partial t} = k_0\left(\overline{u}Q + \gamma\Psi\right) - i\kappa Q, \qquad \Psi \equiv -\left(\hat{k}_y^2 + k_0^2\right)^{-1} Q \tag{4.2}$$

and

$$\frac{\partial \overline{u}}{\partial t} = \overline{v'q'} - \kappa\overline{u} = -\frac{k_0}{2}\left(\mathrm{Im}[\Psi]\mathrm{Re}[Q] - \mathrm{Im}[Q]\mathrm{Re}[\Psi]\right) - \kappa\overline{u} \tag{4.3}$$

for waves and mean flow respectively[1]. We emphasise at this point that $\hat{k}_y = -i\partial_y$ is an operator, as defined in (3.12), and hence (4.2) and (4.3) make no explicit scale separation assumption.

For all the numerical results presented here, (4.2) and (4.3) were solved using an explicit 4^{th} order Runge-Kutta method. The code used was designed to halt whenever a) the Rayleigh-Kuo criterion $\beta - \overline{u}(y)'' < 0$ for barotropic instability or b) the 'rule of thumb' wave-breaking criterion $|u'|_{max} > \omega/k_x$ were satisfied[2]. This ensured that the original physical assumptions behind the model were not broken during the simulation.

As the simulation described in this chapter is highly idealised and not intended to directly model real planetary flows, dimensionless units are used throughout this section. For comparison, however, we note that for a midlatitude slice of Jupiter's atmosphere, when scaled into units of planetary rotation period T_J and radius r_J, the mean zonal wind speed is approximately $\overline{u} = 0.01\ r_J\ T_J\ ^{-1}$ and the β parameter is $\beta = 5 - 10\ r_J\ ^{-1}\ T_J\ ^{-1}$, depending on latitude. For all simulations here we used $\beta = 10$, and the maximum zonal wind speeds of barotropically stable jets were of order $\max[\overline{u}] = 0.001$. Thus we are investigating a fluid dynamical regime with slightly weaker zonation, generally, than that observed on the gas giant planets.

4.2 Linear planetary wavepacket motion

Firstly, we study the extremely simple case of a near-infinitesimal wavepacket with no initial zonal flow and no Ekman damping ($\kappa = 0$). Initial disturbance vorticity is

$$Q = Q_0 \exp\left[il_0 y - (y - y_0)^2/(\Delta y)^2\right], \tag{4.4}$$

with $l_0 = k_0 = 60$, $y_0 = 0.25$ and $\Delta y = 0.1$. In Figure 4.1, the magnitude of the phase space distribution $|\mathcal{N}_{\phi,\phi}|$ is plotted above zonal velocity $\overline{u}$ for a series of timesteps. As can be seen, when the wavepacket has wavevector such that $k_x k_y > 0$, it drifts northwards due to the β-effect.

Weak zonal jets also form as a result of this motion. By the barotropic version of the nonacceleration theorem (3.9)

$$\frac{\partial \overline{u}}{\partial t} = -\frac{\partial n}{\partial t} \tag{4.5}$$

we see that latitudinal planetary wavepacket motion *must always cause jets to form in this way.* For extra clarity, the process is described schematically in Figure 4.2. Even in the quasilinear examples to follow, (4.5) ensures that the motion of wavepackets and the growth of zonal jets are always fundamentally linked.

[1] Prof. C. Jones (private communication) has noted an interesting analogy between equations (4.2) and (4.3), and those derived previously in an idealised study of deep Jovian convection. See [1] for details.

[2] See [8], Chapter 11 for a discussion of the wave-breaking criterion.

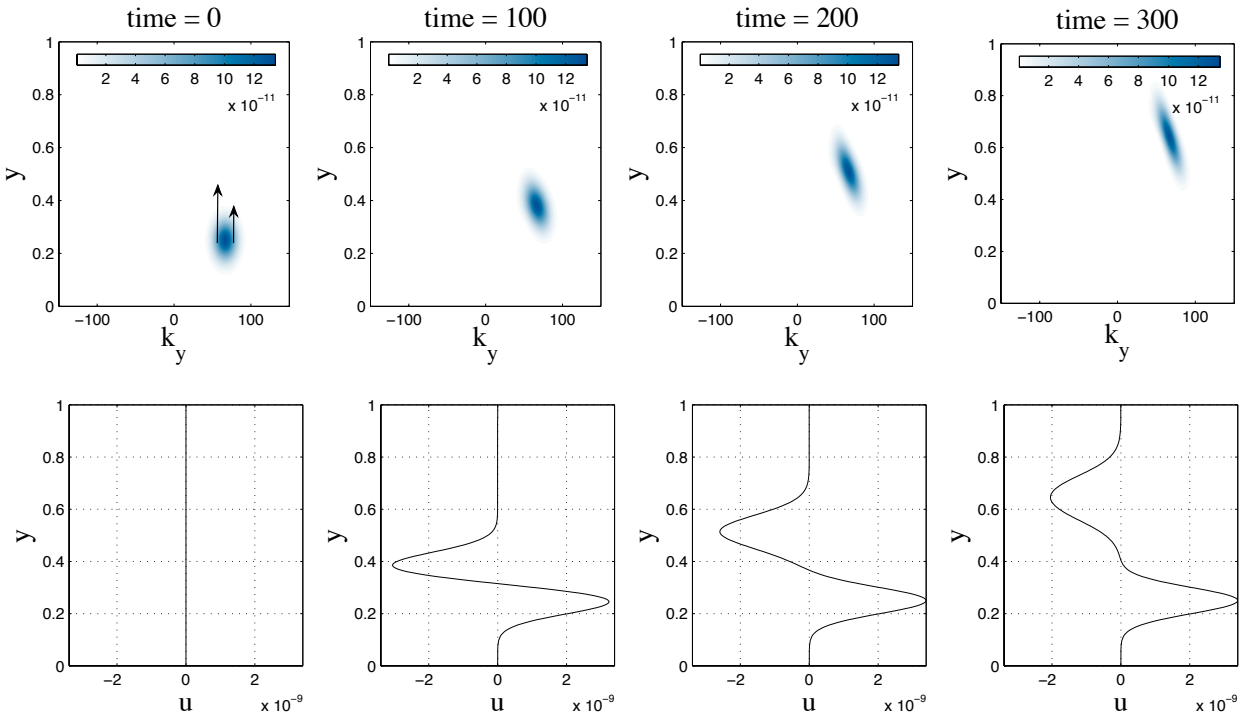

Figure 4.1: A planetary wavepacket on a β-plane with positive k_x and k_y will move northwards. As group velocity depends on k_y, the wavepacket becomes tilted in phase space (top row), although its volume remains approximately the same. Note the small-amplitude zonal flow (bottom row) induced by the wavepacket motion.

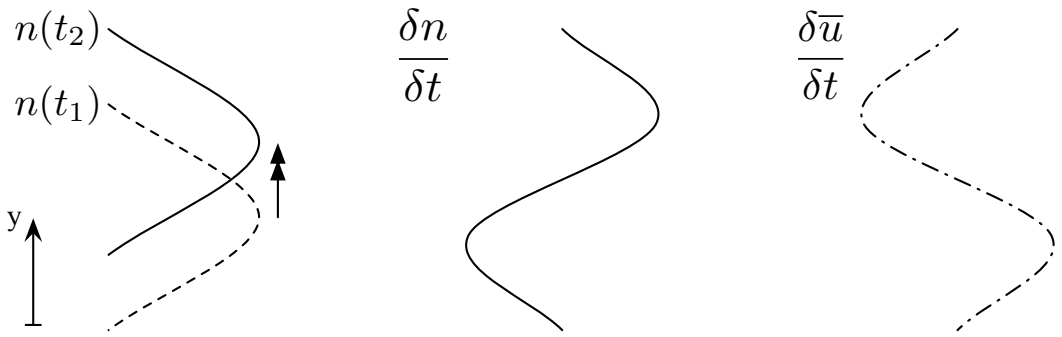

Figure 4.2: Schematic explanation of the jet formation seen in Figure 4.1. If a planetary wavepacket is moving northwards such that in time $\delta t = t_2 - t_1$, $\delta n = n(t_2) - n(t_1)$, then the nonacceleration theorem (4.5) ensures the zonal flow produced $\delta \overline{u}$ will be of the form shown.

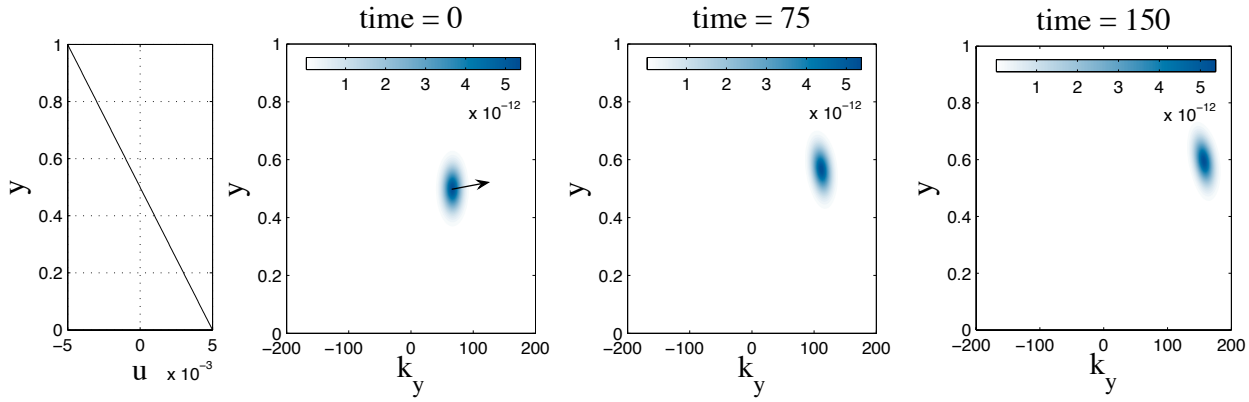

Figure 4.3: In the presence of a shear flow that decreases linearly with latitude (far left), a planetary wavepacket with positive k_x will move toward higher wavenumbers, losing energy to the zonal flow in the process. Note the slight northward drift of the wavepacket; this is due to the β-effect shown in Figure 4.1.

The group velocity calculated from (4.1) agrees closely with the observed velocity of the wavepacket peak (the difference is less than 3% in the example shown). However, note the stretching of the wavepacket in phase space. This is due to the dispersive nature of the planetary waves, as determined by (3.2). Essentially, the group velocity v_y on the left hand side (in phase space) of the wavepacket is greater than that on the right — this is shown schematically by the arrows on the first plot in Figure 4.1.

The second basic case of interest is that of an infinitesimal wavepacket on a linearly sheared zonal flow, $\overline{u} = -\Lambda(y - y_0)$. Here, $\Lambda = 0.01$, $y_0 = 0.5$ and all other parameters are as in the previous example. As shown in Figure 4.3, in this situation a wavepacket with $k_x > 0$ is forced towards higher k_y wavenumbers, losing energy to the zonal flow in the process. As $\beta = \gamma$ in this example, the enstrophy of the wavepacket remains constant and hence energy is transferred upscale, while enstrophy moves downscale. Again, scale-separated predictions match the observed value closely for this case.

4.3 Wave-mean flow interactions and jet asymmetry

More interesting and subtle phenomena occur when we allow the wavepacket to be of large enough amplitude for coupling with the zonal flow, but not wave-breaking, to occur (see Figure 4.4). Then, we expect it to initially move northwards, with two zonal jets forming due to the non-acceleration theorem as in the first example. However, as the zonal flow becomes stronger, it begins to influence wavepacket propagation through a) the shear effect described in the second example and b) alteration of the basic potential vorticity gradient $\gamma = \beta - \partial_{yy}\overline{u}$ (see equation (4.1)). As the initial zonal flow gradient in the centre of the channel is negative, the wavepacket is forced to higher k_y wavenumbers, reducing its group velocity and hence the growth rate of the zonal flow. This process continues until the zonal flow either removes most of the wavepacket energy and reaches a quasi-steady state, or sharpens to the extent that it becomes barotropically unstable.

For reference, the real space eddy streamfunction ψ' and (unaveraged) momentum flux quantity $u'v'$ at the end of the simulation are plotted in Figure 4.6. These variables were derived after computation, and are included here simply to illustrate the equivalence of the phase and real space pictures.

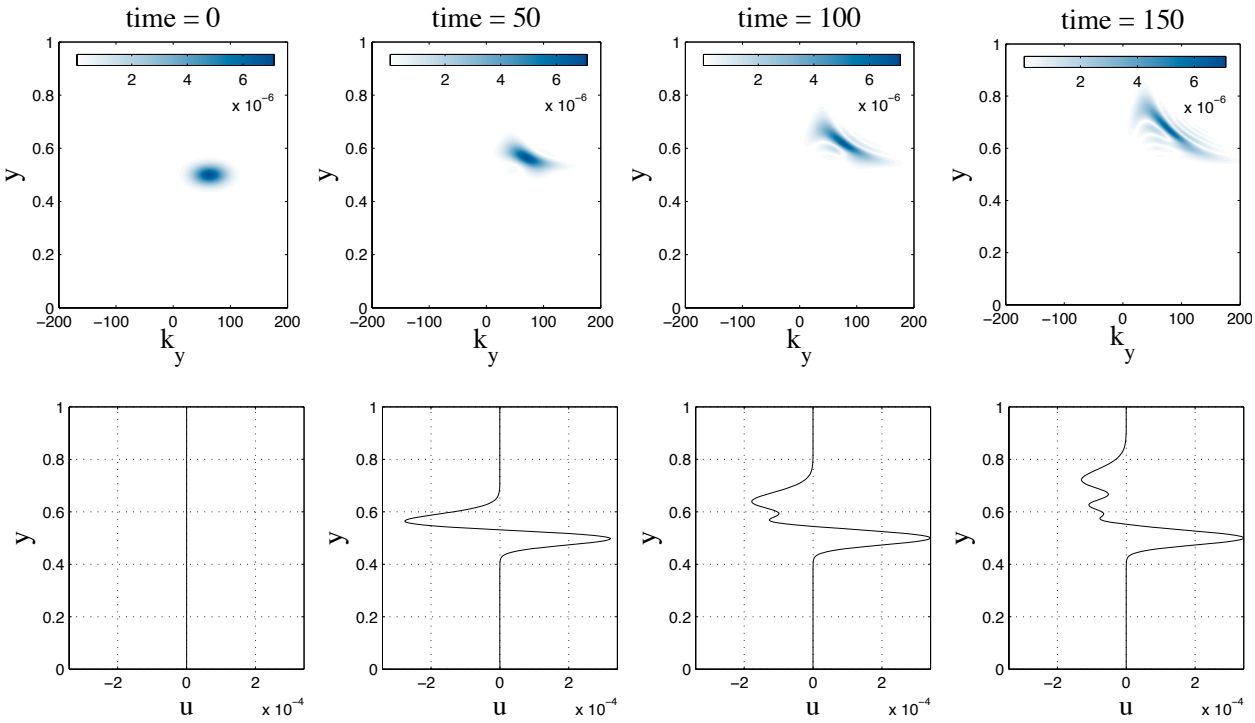

Figure 4.4: Quasilinear evolution of a wavepacket ($Q_0 = 0.12$, $y_0 = 0.5$, $\Delta y = 0.05$, all other parameters as in first example). Initially, the wavepacket moves as in Figure 4.1, but the zonal shear it produces modifies its motion as time progresses. By $t = 100$, the Wigner distribution had become negative-valued in places.

It is fascinating to note that east-west jet asymmetry occurs regardless of the wavevector $\mathbf{k}$ sign of the initial wavepacket. As expected from (4.1) and shown in Figure 4.5, if the product $k_x k_y$ is negative, the packet initially moves south, and the initial induced jets are of opposite sign. However, whatever the sign of k_x and k_y, jet formation always pushes some wave action to higher *absolute* wavenumber values $|k_y|$. Combined with the fact that the wavepacket propagates away from the jet in a direction dependent on $k_x k_y$, the result is that in each case, the eastward jet becomes sharper than the westward one.

This phenomenon can also be explained via a conservation of energy argument; jet formation increases zonal flow energy, which necessitates energy *loss* by the wavepacket. As the zonal flow cannot alter k_x, this can only be achieved through transport of wave action to higher absolute k_y. Thus, east-west asymmetry appears to be a quite generic feature of wave-forced jets on the β-plane that does not require the existence of critical layers for its occurrence. The fundamental cause of the phenomenon is evidently the chiral (left / right hand) symmetry breaking due to the fact that we are working in a rotating coordinate frame. This is manifested in the quasigeostrophic equation (3.1) through the positive-valued β parameter. We note that evidence of quasigeostrophic jet asymmetry has also been found in several previous studies, including those of Haynes [25] and Chekhlov et al. [12].

Use of the Wigner distribution allows us to examine in detail the regions where the scale separation approximation (equation (3.25)) does badly, at any time during the simulation. In Figure 4.7, for an example quasilinear wavepacket in phase space (initial conditions $l_0 = k_0 = 30$, $y_0 = 0.5$,

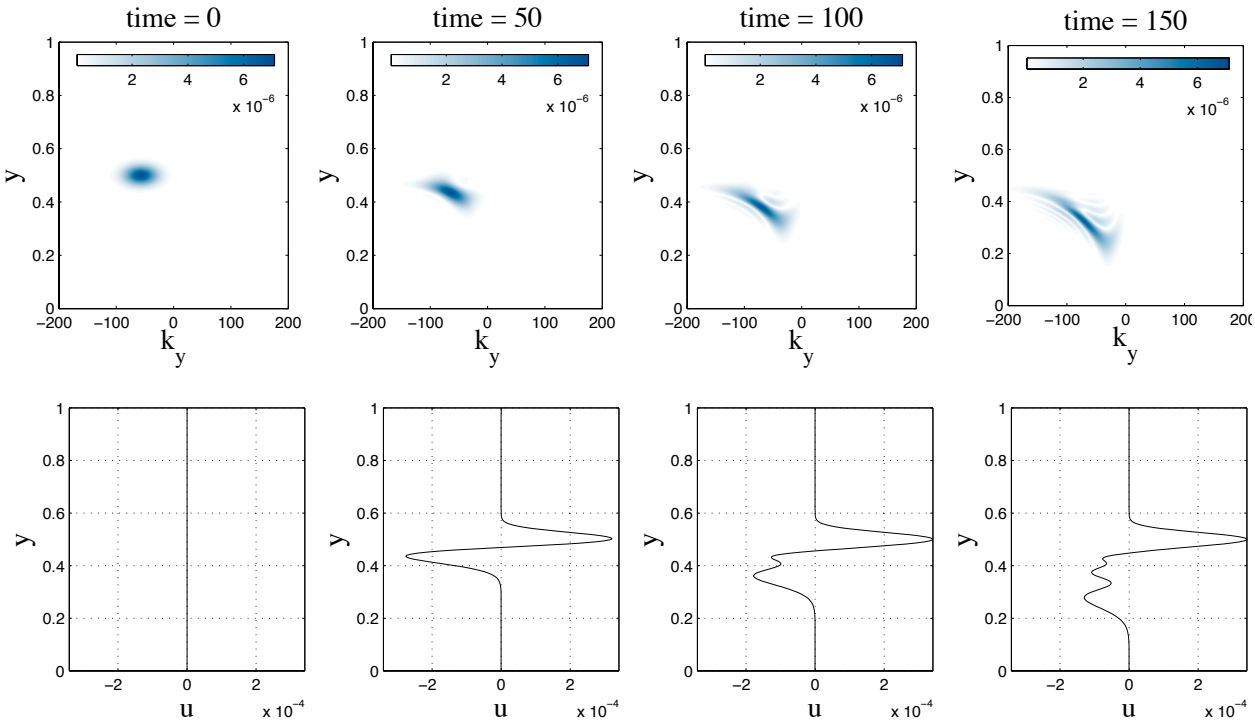

Figure 4.5: The same simulation as Figure 4.4, with the initial k_y value of the wavepacket reversed. Initially, the induced jets are of opposite sign, but when east-west asymmetry develops, the eastward jet becomes the sharper one as in the previous case.

$\Delta y = 0.05$ and $Q_0 = 0.3$), the actual time rate of change of the Wigner distribution $\partial \mathcal{N}_{\phi,\phi}/\partial t$ at $t = 50$ is plotted alongside the scale-separated estimate of rate of change, which was calculated numerically for a single timestep according to (3.25). The agreement between the two quantities is good near the centre of the wavepacket, with serious deviations only beginning to occur in the lower wavenumber region, where rapid fluctuations in the distribution are occuring (bottom left of the centre and right hand side plots). It is interesting that for many cases like this one, where wavepacket – zonal flow scale separation could not be assumed, the scale-separated estimate of $\partial \mathcal{N}_{\phi,\phi}/\partial t$ continued to agree surprisingly well with the real value. In the next section, it will be seen that scale-seperated estimates of steady-state energy were also found to work well, even when the assumptions behind them did not strictly apply.

4.4 Steady-state jets

If Ekman damping is present and the planetary wavepacket is continually forced, in many cases the system will eventually settle into a steady state. To investigate steady-state jet behaviour, we add a term to the right hand side of equation (4.2) of the form $+i\kappa Q_f(y)$. This ensures that the disturbance quantity Q is continually relaxed to the profile Q_f, which for the simulation discussed here is defined as $Q_f = Q_0 \exp[il_0 y - (y - y_0)^2/(\Delta y)^2]$. Such a profile could correspond to a topographically forced planetary wave, or an (idealised) local region of excitation due to other processes, such as convection or baroclinic instability.

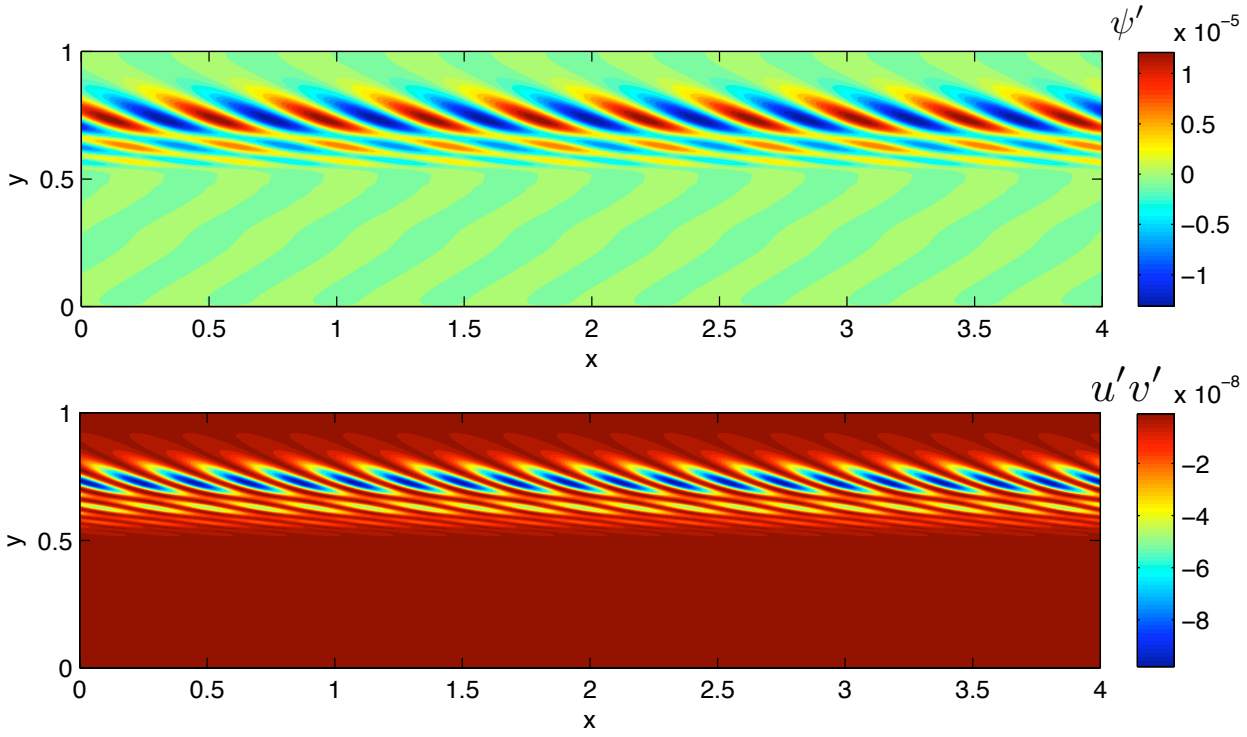

Figure 4.6: Real space eddy streamfunction $\psi' = \mathrm{Re}[\Psi e^{ik_0 x}]$ (top) and momentum flux $\overline{u'v'}$ (bottom) at $t = 500$ for the run shown in Figure 4.4. As can be seen, northwards motion of a positive wavepacket causes a negative eddy momentum flux in real space.

Figure 4.8 shows a plot of wavepacket and zonal jet total kinetic energy as a function of time, for a simulation with $Q_0 = 1 \times 10^{-1/2}$ and damping set at $\kappa = 0.01$. It can be seen that after a period of rapid initial wavepacket growth, the zonal flow begins to gain energy by moving wave action to higher wavenumbers. This causes the total eddy energy, and hence the total system energy, to slowly decrease until a steady state is reached.

For a small-scale wavepacket, we expect the steady-state zonal velocity to be given by

$$\kappa\overline{u} = \overline{v'q'} \approx \frac{\partial}{\partial y}\left(\int_{-\infty}^{+\infty} \mathcal{N}(y, k_y) v_y \mathrm{d}k_y\right) \tag{4.6}$$

where v_y is the group velocity in the y-direction and $\mathcal{N}(y, k_y)$, as defined in (3.18), is the projection of the Wigner distribution (3.15) onto two-dimensional (y, k_y) phase space.

Now if the amplitude of the steady-state wavepacket is small, we expect it to be relatively undistorted by the zonal jets it produces, and hence approximate the standard form

$$\mathcal{N}(y, k_y) = \mathcal{N}_0 e^{-2((y-y_0)/\Delta y)^2 - ((k_y - l_0)\Delta y)^2/2} \tag{4.7}$$

where $\mathcal{N}_0$ is the steady-state peak wavepacket value. Provided that the variation of group velocity with k_y is small over the width of the wavepacket, (4.6) can then be integrated to give an estimate

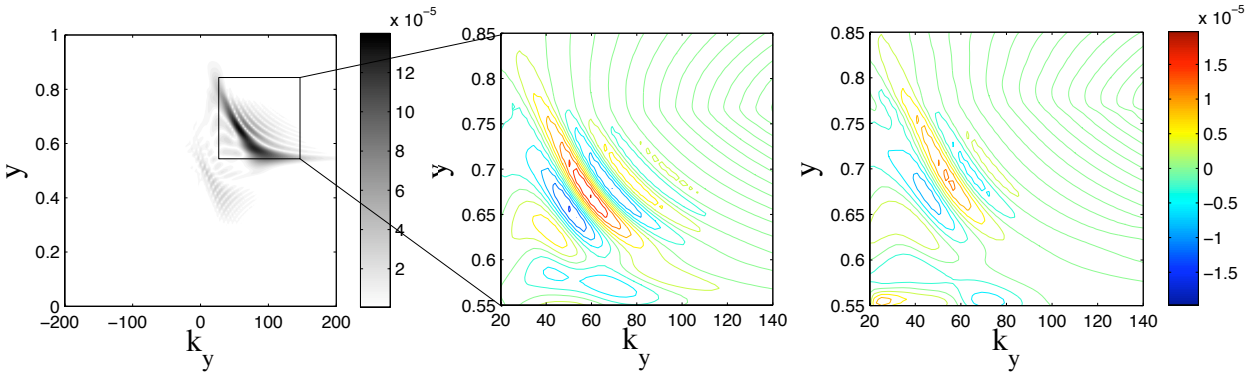

Figure 4.7: Magnitude of Wigner distribution $|\mathcal{N}_{\phi,\phi}|$ (left) plotted alongside actual local time rate of change $\partial\mathcal{N}_{\phi,\phi}/\partial t$ (center) and scale-separated $\partial\mathcal{N}/\partial t$ (right) for a generic wavepacket motion problem. The same contour scale has been used for the second two plots.

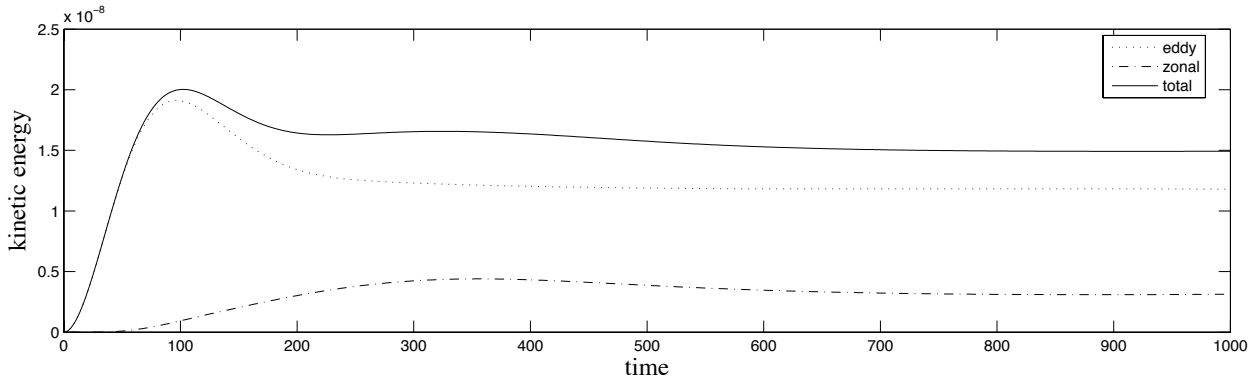

Figure 4.8: Eddy, zonal and total kinetic energies as a function of time for a simulation with planetary wavepacket forcing and Ekman damping of both zonal flow and eddies.

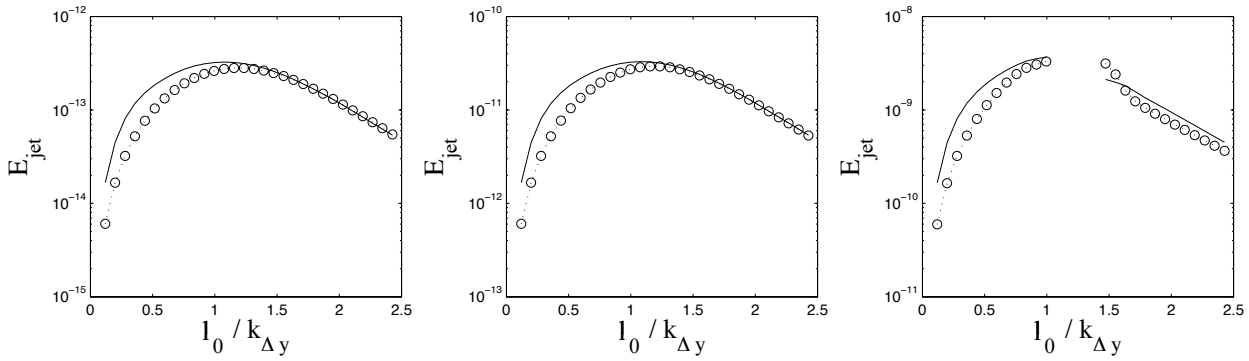

Figure 4.9: Total steady-state jet kinetic energy as a function of scale separation for the relaxation problem described in the text. Solid and dotted lines show linear analytical predictions and numerical results, respectively. Eddy forcing amplitudes were $Q_0 = 1 \times 10^{-3/2}$, 1×10^{-1} and $1 \times 10^{-1/2}$ for the left, centre and right hand side plots respectively. The right hand side plot has fewer data points because wave-breaking begins to occur at high forcing amplitudes.

of the total kinetic energy of the jet

$$E_{jet} \equiv \int_{jet} \frac{1}{2}\overline{u}^2 \mathrm{d}y \tag{4.8}$$

$$\approx \frac{16\pi \mathcal{N}_0^2 v_y^2}{\kappa^2 \Delta y^6} \int_{-\infty}^{+\infty} (y - y_0)^2 e^{-4(y-y_0)^2/\Delta y^2} \mathrm{d}y \tag{4.9}$$

$$\approx \frac{\pi^{3/2} v_y^2 \mathcal{N}_0^2}{\kappa^2 \Delta y^3}. \tag{4.10}$$

We expect (4.8) to be valid in the limit of forcing by small amplitude, scale-separated wavepackets. In Figure 4.9, we have plotted the predictions of (4.8) against numerical jet kinetic energy for varying values of wavepacket scale seperation, defined as $l_0/k_\Delta y$. Calculations were made for three different values of forcing amplitude, and each individual simulation was run for 100 times the relaxation time κ^{-1} to ensure that a steady state was reached. For the plots shown, the east-west wavenumber is fixed at a constant value $k_0 = 40$. As can be seen, the final jet energy rapidly increases to a maximum at around $l_0/k_\Delta y = 1$, and then decreases, as the forcing wavenumber is increased.

As expected, the numerical results closely match the linear predictions only when wavelength is small compared to the jet width. In general, the analytical predictions tend to overestimate total zonal kinetic energy at low values of of $l_0/k_{\Delta y}$, although the difference is surprisingly low, considering that scale separation should only strictly apply for the case $l_0 >> k_{\Delta y}$. In the rightmost plot of Figure 4.9, the forcing amplitude is great enough for wave breaking to occur in some cases; this is the reason for the missing data points in the centre of the plot.

4.5 Discussion

In this chapter, the nonlinear interaction between an arbitrary zonal flow and a broadband distribution of planetary waves has been simulated numerically, and compared with the scale-separated

results derived in Chapter 3. It has been possible to show that jet formation can occur in an *extremely* reduced and simple model. Through phase space analysis, it was possible to explain why and how this jet formation occurs. Furthermore, the phase space view allowed an intuitive explanation of why the fully developed jets begin to develop significant east-west asymmetry.

There are of course many further experiments that could be carried out with the model presented here. For example, the effects of small-scale convection could be crudely parameterised by including a random forcing term in the wave equation (4.2). This would add an extra degree of realism to the jet formation process. It would also perhaps give insight into the problem of *multiple* jet formation, which has not been addressed in this chapter.

In addition, as this model is barotropic, it completely neglects the vertical structure of the jets and waves. In real atmospheres and in the laboratory experiment described in Chapters 5-7, the vertical structure of the flow is an important feature of the overall dynamics. In Chapter 8, therefore, the model is generalised to a two-layer system, in order to simulate the experimental results.

More generally, we note that it is standard in nearly all studies of turbulent flows to take either a real space view of the dynamics, or a spectral one. Both approaches have their respective advantages and drawbacks, but phase space analyses, by use of the Wigner distribution, allow us to take both simultaneously. Hence it is suggested that for many fluid dynamical problems, particularly those involving a mean flow and a disturbance, phase space views of the dynamics have the potential to greatly increase our understanding of the systems' behaviour.

Chapter 5

Experimental setup

The major difference between a thing that might go wrong and a thing that cannot possibly go wrong is that when a thing that cannot possibly go wrong goes wrong, it usually turns out to be impossible to get at or repair.
— Douglas Adams

As was discussed in Chapter 1, the second major part of this project involved the design and construction of an experiment to reproduce the essential features of planetary-scale turbulence in the laboratory. In this chapter, the setup of the experiment is described in detail. We begin with an overview and discussion of the basic apparatus in Section 5.1, also describing some early work carried out to modify the central cylinder. Next, in Section 5.2, the data acquisition system is described, with hardware and software components discussed in detail in separate subsections. Finally, problems that occurred during the commissioning of the experiment, along with their solutions, are summarised in Section 5.3. The following two chapters are based on a paper [70] that has been accepted for publication in *Physics of Fluids*.

5.1 Overview

The basic idea behind the experiment, as discussed in Chapter 1, is to mimic the effects of tropical heating and polar cooling on a mid-latitude air mass by heating and cooling respectively the outer and inner sidewalls of an annulus filled with water, or some similar working fluid. Figure 5.1 shows the general experimental setup; see Figure 5.2 for images of the entire apparatus.

Previous studies have shown that the state of a differentially heated rotating annulus is principally determined by two dimensionless numbers: the Taylor number

$$Ta \equiv \frac{4\Omega^2(b-a)^5}{\nu^2 d} \approx \frac{\left[2\Omega \times \mathbf{u}\right]^2}{\left[\nu\nabla^2\mathbf{u}\right]^2}, \tag{5.1}$$

which is a ratio between Coriolis and viscous effects, and the Hide number

$$\Theta \equiv \frac{\alpha g d \Delta T}{\Omega^2(b-a)^2}, \tag{5.2}$$

which is essentially a ratio between buoyancy and Coriolis effects or 'thermal Rossby number' [27]. In the above equations, a and b are the inner and outer cylinder radii, Ω is the rotation rate, ν

is the viscosity of the working fluid, d is the depth of the annulus, α is the volumetric expansion coefficient, g is gravitational acceleration and ΔT is the temperature difference between inner and outer cylinders. Values of all general parameters for the experiment are given in Table 5.1 below[1].

Table 5.1: General experimental parameters.

Radius of inner cylinder	a	4.5 cm
Radius of outer cylinder	b	14.3 cm
Annulus depth (flat)	d	26 cm
Annulus mean depth (sloping)	$\overline{d}$	21.5 cm
Gravitational acceleration	g	9.81 m s^{-2}
Sloping boundary angle	δ	22°
Kinematic viscosity of fluid A	ν_A	2.04×10^{-6} m^2s^{-1}
Kinematic viscosity of fluid B	ν_B	1.11×10^{-6} m^2s^{-1}
Volumetric expansion coefficient of fluid A	α_A	3.16×10^{-4} K^{-1}
Volumetric expansion coefficient of fluid B	α_B	3×10^{-4} K^{-1}

A large body of previous experimental studies (see e.g., [30], [50]) have shown that the transition to disordered, geostrophically turbulent flow occurs at large Taylor and low Hide numbers. In this work, an existing annulus was modified by reducing the radius of its inner cylinder and hence increasing the channel width $(b - a)$. At high rotation rates, this allowed the apparatus to reach Taylor numbers an order of magnitude greater than have been typically achieved previously.

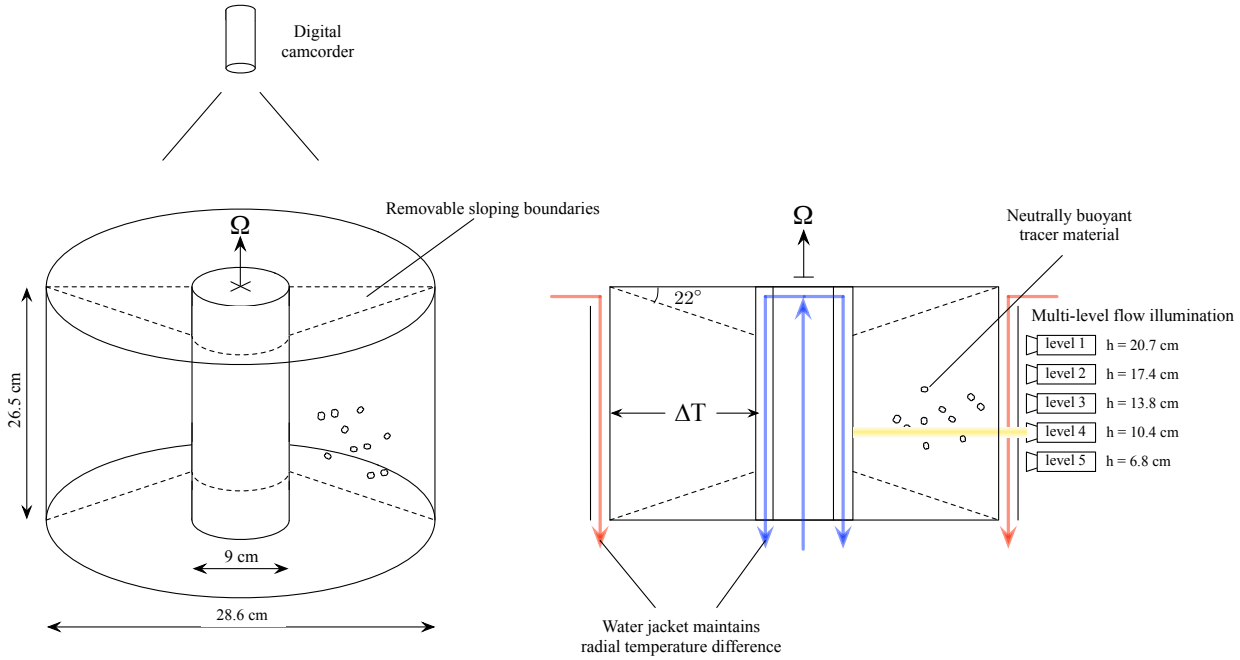

Figure 5.1: Schematic of the experimental apparatus.

[1]Note that the value given for the volumetric expansion coefficient of fluid B, obtained from the oceanographic text [62], is only approximate. The accuracy of this quantity was not critical for any of the analyses described in Chapter 6.

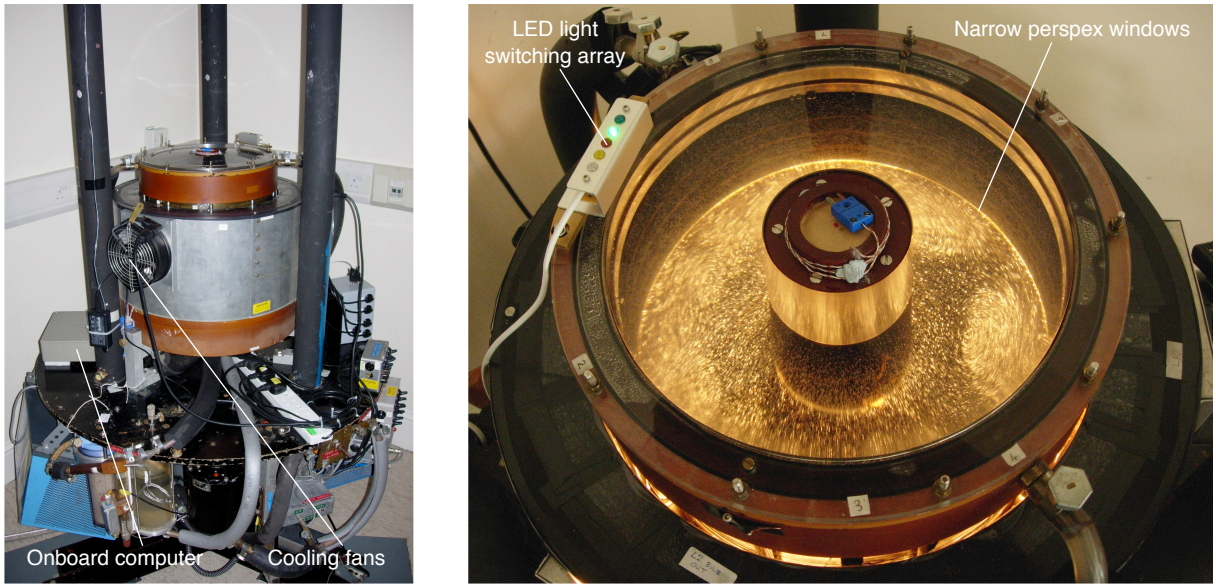

Figure 5.2: a) Side view photograph of the fully assembled experiment. The digital camera is mounted on the black steel tripod (not in view). Locations of cooling fans and the Mac mini computer are indicated. b) Top view photograph of the experiment. Locations of the LED light switching array and perspex windows are indicated.

The working fluid inside the annulus was seeded with neutral buoyancy pliolite tracer particles of radius $350\mu m - 500\mu m$ for visualisation purposes. For most experiments, a 82.5% to 17.5% water / glycerol mix (fluid A) was chosen as the working fluid, to match the mean density of the tracer particles, $\rho = 1.043$ g cm^{-3}. Some experiments were also performed with a NaCl salt solution (fluid B); in this case density was the same but viscosity was only $\nu = 1.111$ cm$^2 s^{-1}$. This allowed a greater Taylor number and hence a potentially more turbulent flow at the same rotation rate as in the previous case. However, the salt solution had a corrosive effect on the brass inner and outer walls of the annulus, and hence was only used for a small number of high rotation rate experiments.

The annulus was placed on a rotating turntable and accurately centered by use of a sighting telescope. The turntable rotation was powered by an analogue motor, which was controlled via negative feedback from a tachometer by a DC servo amplifier system. Thermal control of the annulus was achieved via two closed water circuits, which contained both heating and cooling elements. A EUROTHERM 900 electronic controller kept the temperature of both circuits constant by actively controlling the heating and cooling elements, with feedback provided by temperature sensors placed in each circuit. Typically, fluctuations in measured temperature under steady forcing conditions were less than ± 0.05 K. Filtration units were also included, to keep the water clean and prevent clogging of the inlet holes in the inner and outer annulus walls. In Figure 5.3, the entire thermal control system is summarised as a block diagram.

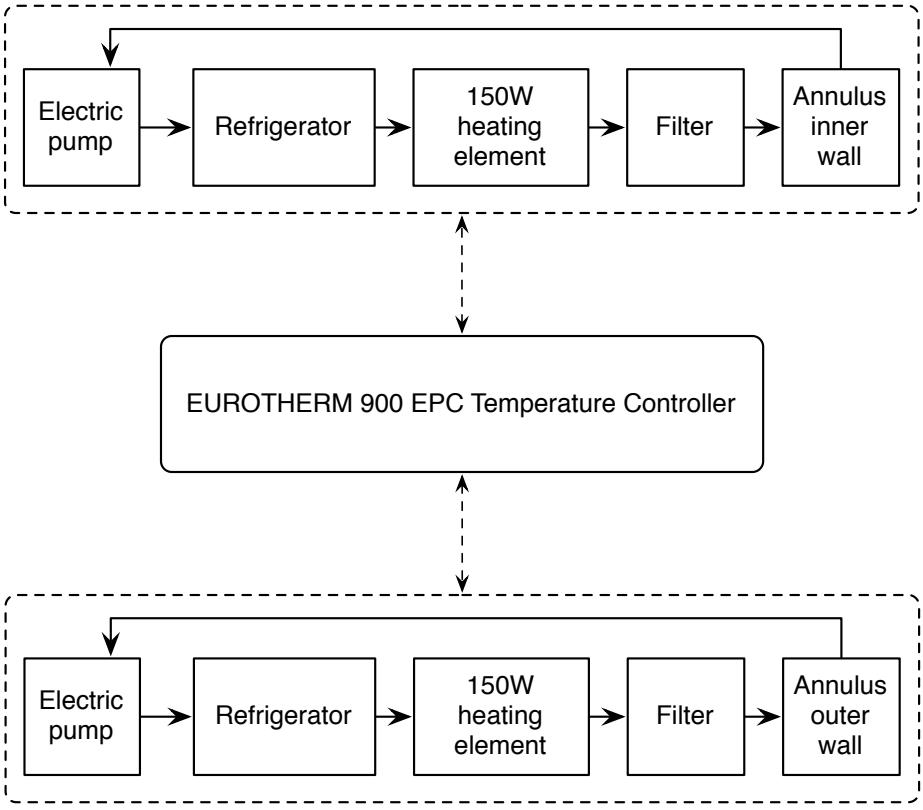

Figure 5.3: Block diagram of the double water jacket temperature control system.

5.1.1 Modification of old apparatus

One of the initial tasks of this DPhil was to modify an existing apparatus for the purposes of investigating highly irregular and turbulent flow regimes. The primary aim of the modification work was to reduce the radius of the inner cylinder, in order to increase the accessible Taylor number range, as described in the previous section. More generally, it was also necessary to repair and upgrade the experimental hardware, much of which was either faulty or obsolete.

Modification of the old annulus required an extensive period of redesign. The original technical drawings for the annulus were entirely hand drawn, so an initial task was to convert these into a modern, digital format. The commercial software package Inventor was chosen for this purpose because of its flexibility and relative ease of use.

Once the structure of the original experiment was fully understood, design of the new inner cylinder began. It was decided to keep much of the internal structure, particularly the water inlet mechanism, the same; the only major change was the removal of O-rings from the cylinder base. Silicone sealant was initially used there, as it was thought to be a more convenient and robust way of keeping the structure watertight. However, O-rings proved to be a far more reliable long-term sealing method; see Section 5.3 for details.

The choice of materials is obviously extremely important in the design of any piece of apparatus. For this experiment, it was decided to use Bear grade Tufnol (layers of cloth bonded with thermosetting resin) for most cylinder parts except the external inner cylinder wall. For this, a material with high thermal conductivity was needed; brass was chosen due to its high availability and low cost. The wall thickness was chosen to be $\delta x = 5$ mm. When combined with the thermal properties of brass (see Table 5.2), this length scale can be used to derive a characteristic time for heat diffusion

$$\tau = \frac{c_p \rho (\delta x)^2}{\sigma_t} = 0.52 \text{ s}. \tag{5.3}$$

This value for τ is smaller than the highest rotation period used in the experiments. As timescales for fluid motion in the annulus at high rotation rate are typically much greater than the rotation period, variations in boundary temperature caused by eddy heat transport were therefore not expected to be significant. For the upper boundaries (flat and sloping), perspex was used, to allow flow visualisation. The design of the upper sloping boundary was made a little more complicated by optical considerations; this issue is discussed further in the next section.

Table 5.2: Thermal properties of brass (taken from the materials database *www.matweb.com*).

Density	ρ	8.75 g cm^3
Thermal conductivity	σ_t	159 W m^{-1} K
Specific heat capacity	c_p	0.380 J g^{-1} K

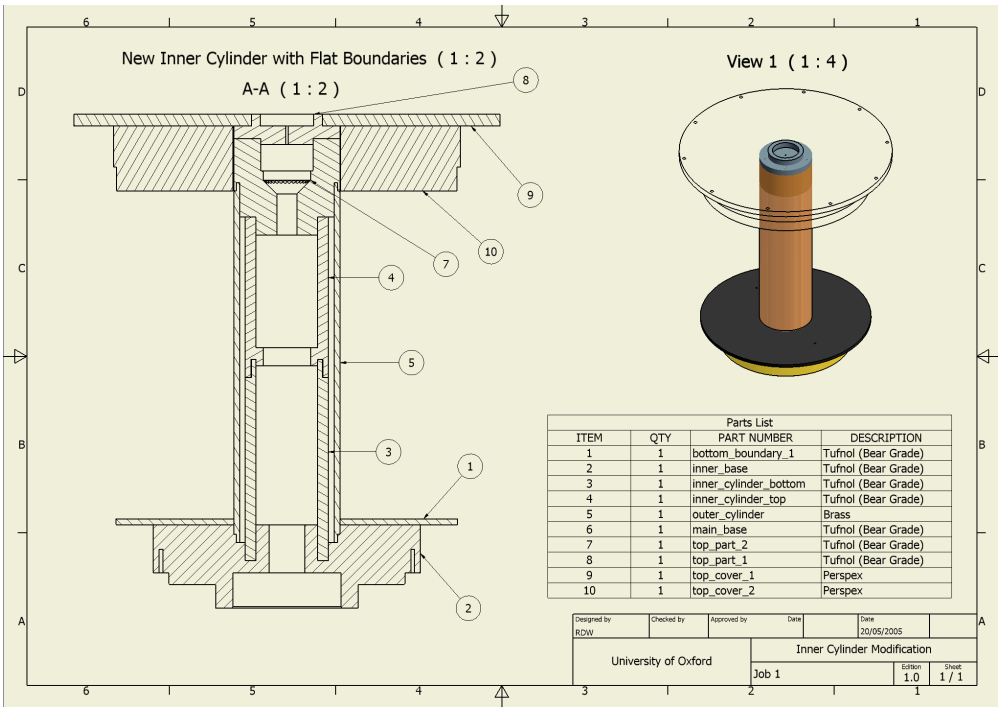

Figure 5.4: Technical drawing of the modified inner cylinder for the flat boundary case.

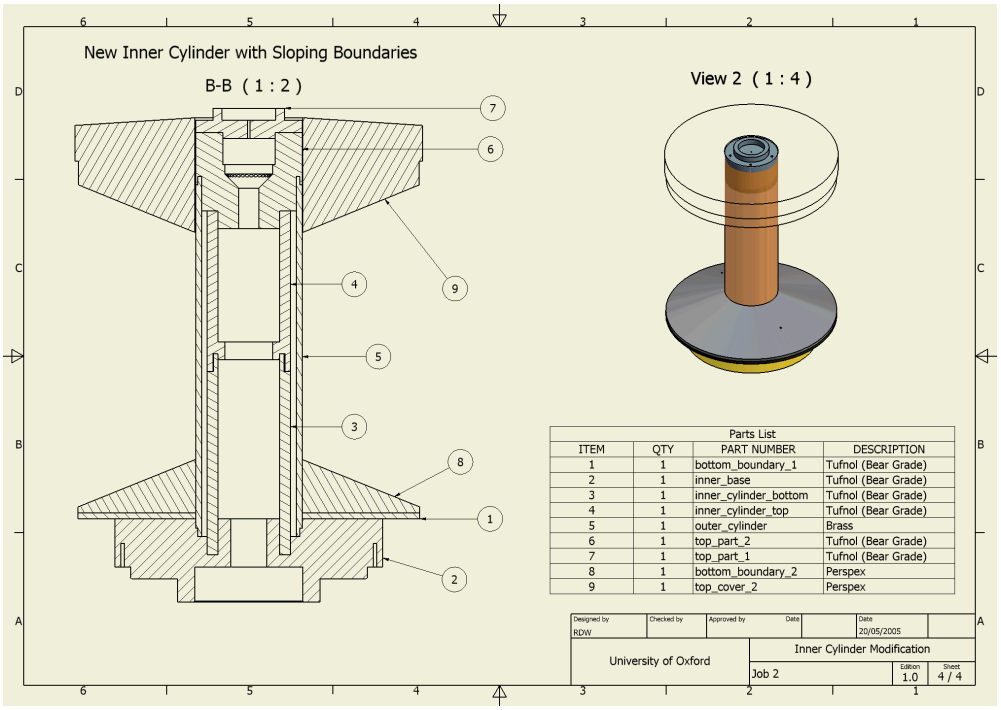

Figure 5.5: Technical drawing of the modified inner cylinder for the sloping boundary case.

5.2 Data acquisition

The problem of acquiring data in fluid dynamics experiments is always a non-trivial one, but for heat-driven turbulent flows it becomes challenging indeed. Full characterisation of the dynamics requires velocity and temperature information on a wide range of scales and for even moderate Reynolds numbers, compromises are usually required.

For velocity field measurement, it was chosen to use flow visualisation via the illumination of neutrally buoyant tracer particles. This 'remote sensing' approach has the great advantage of allowing characterisation of the 2D dynamics of the full annulus, at multiple levels of the flow, using a single camera or camcorder. It also allows greater resolution than would be feasible with other methods, such as *in situ* measurement.

Temperature measurements of the fluid interior, although desirable, ultimately proved to be unfeasible within the budget and time constraints of the project. However, fairly detailed investigations into possible temperature field acquisition methods were made over the course of the DPhil. They are outlined in Section 5.2.3 for the benefit of future experimental research.

5.2.1 Hardware

Given the choice of flow visualisation as the main method of data acquisition, the correct choice of camcorder and storage technology was clearly very important. The existing experimental setup used a Cohu CCD analogue camera with standard PAL output. A rotating slip ring at the top of the turntable assembly was used to transfer the analogue signal into the laboratory frame. From there the signal passed to a television and VHS video recorder where the program DigImage was used to convert the data into digital format for velocity field analysis.

This arrangement was judged to be impractical for a number of reasons. First, much of the technology in use was obsolete, making future repair work or partial modification an extremely difficult prospect. Second, the use of analogue video resulted in an increase of noise due to both the slip-rings and the analogue-digital conversion process. Finally, the digitisation and velocity field extraction process was extremely slow (around 20 minutes for a single timestep), making it ill-suited for analysis of turbulent flows over time.

It was decided to use a radically different setup for video acquisition. The Cohu analogue camera was replaced with a Sony DCR-HC44 MiniDV camcorder, with resolution of 720×576 pixels. A Mac mini computer was installed on the turntable and used to control the camcorder directly, with FireWire used to transfer the video data. The computer's inbuilt wireless ethernet connection was then used to communicate with a Windows PC on a desk nearby. This allowed a) wireless control of data acquisition at arbitrary rotation rates, b) remote real-time visualisation of the flow and c) quick, reliable transfer of data to desktop PC for further processing at the end of each experimental run. Furthermore, the possibility of increased noise due to slip-ring interference was eliminated.

As the refractive indices of air, perspex and the working fluid are different (see Table 5.3), light rays travelling upwards through an upper perspex boundary with a sloping bottom and flat top would be refracted, resulting in a distorted image at the camera. For this reason, the perspex lid was machined with a slope of $\delta_u = 3.5^\circ$ on its upper surface. The angle δ_u was calculated such that to first order, rays travelling vertically from mid-depth and mid-channel to camera height would converge on a central point. Deviations from this approximation were checked by photographing

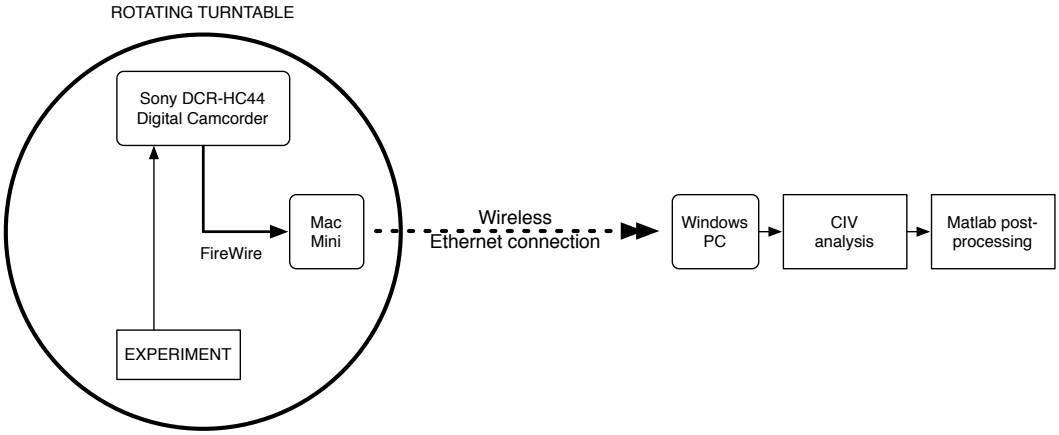

Figure 5.6: Flow diagram indicating the data acquisition hardware and software setup.

a checkerboard pattern in the tank at different depths (see Figure 5.7). The maximum distortion error at the inner and outer walls was a few pixels only, which was judged sufficiently small to be neglected in the analysis.

Table 5.3: Optical properties of materials relevant to the sloping boundary visualisation problem.

Refractive index of air	n_{air}	1.001
Refractive index of perspex	n_p	1.492
Refractive index of working fluid A	n_A	1.357
Refractive index of working fluid B	n_B	1.341

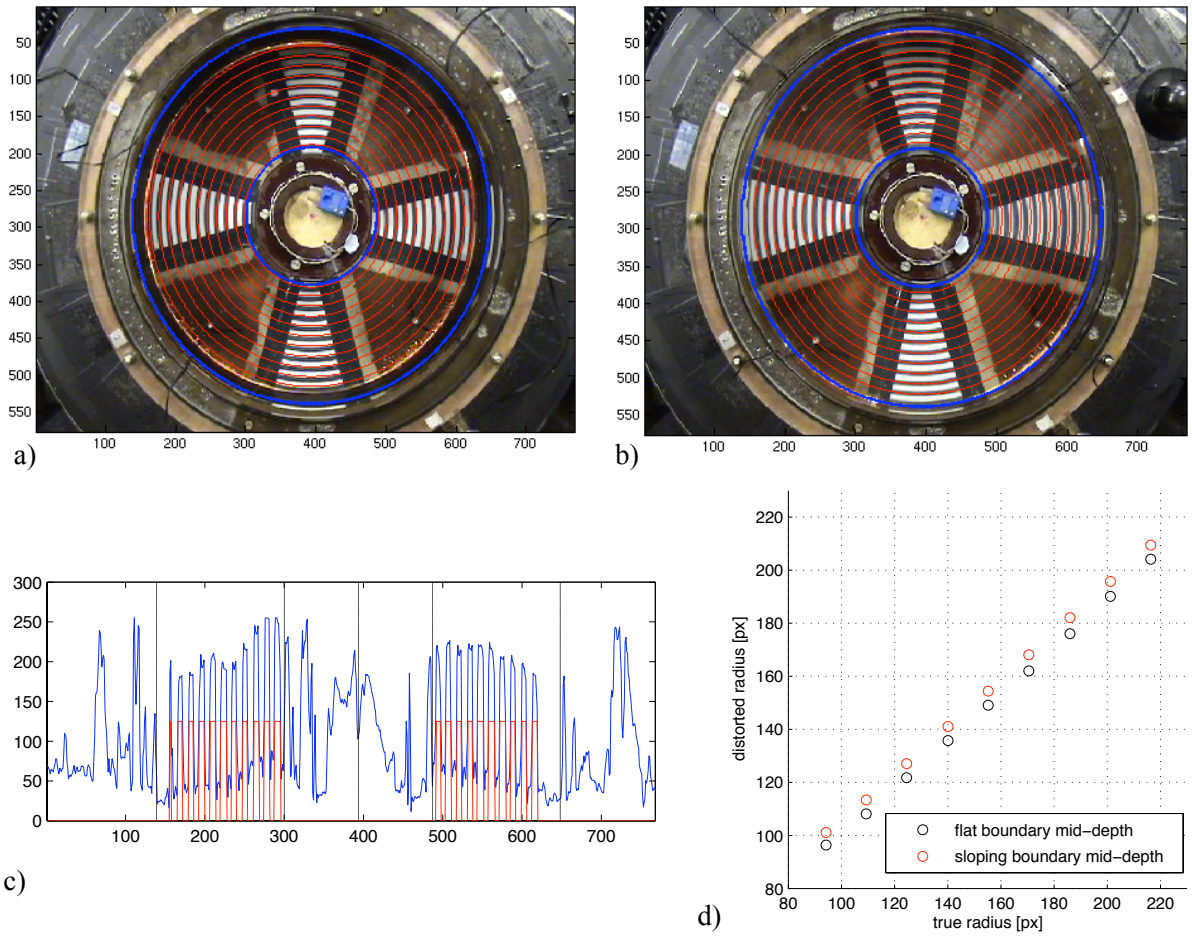

Figure 5.7: Images at mid-depth of the black and white rings used for calibrating the digital camera with a) flat and b) sloping upper boundary present. The superimposed red lines correspond to edges of the radial black stripes, as recognised by the Matlab edge-finding algorithm. c) Plot of total pixel intensity as a function of radius for the flat boundary image with edge-finding superimposed. d) Calibration curves for the flat and sloping boundary images.

Light level switching circuit

To estimate the relative importance of barotropic and baroclinic effects, it is necessary to extract velocity fields at different levels in the fluid. The more levels observed, the greater the vertical resolution that can be achieved. As can be seen from Figure 5.1, the experimental apparatus contained a total of five narrow perspex windows along the entire diameter of the outer cylinder at different height levels. Rings of six 50W halogen lamps behind each window provided illumination in the 2D plane. As the lamps were enclosed, a cooling mechanism was necessary; this was provided by three electric fans mounted on the outer shell of the experimental apparatus (see Figure 5.2).

Early in the DPhil project, a switchbox was constructed to allow the level of illumination to be set manually. However, it was later decided to build a oscillation circuit (Figure 5.8), in order to automate the level switching process and hence allow for a quasi-3D picture of the flow dynamics. The circuit incorporated a multicolour LED array (also marked in Figure 5.2) that was placed in view of the camcorder, effectively tagging each image with a unique level identification. An algorithm was then written in Matlab that automatically sorted flow images by level, based on the total pixel intensity within the region of the relevant LED.

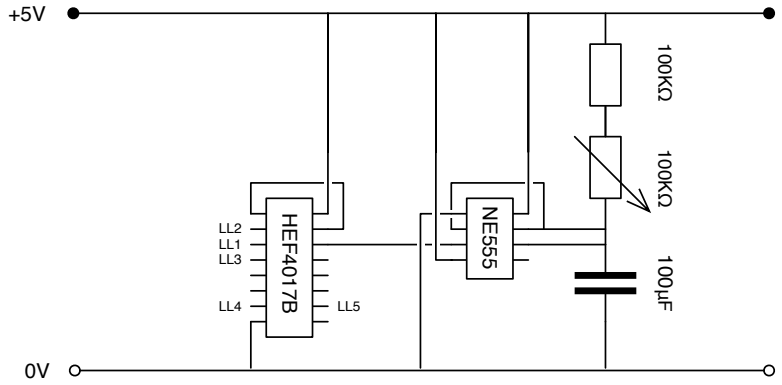

Figure 5.8: Circuit diagram of the light level switching circuit designed by the author and constructed by G. A. Clack. The outputs 'LL1' etc. from the HEF4017B Johnson counter are TTL logic switches for the lamp arrays and associated LEDs.

5.2.2 Software

For frame-selective acquisition of the video data via FireWire on the Mac mini computer, the versatile shareware program BTV Pro was used. Virtual Network Client (VNC) and Secure Shell (ssh) were used to remotely control the Mac mini and transfer video files, respectively — freeware versions of both of these programs are available for download on the internet. Video files were first saved in low-compression DV format and then converted to sequences of 256 grayscale portable network graphics (.png) format images. Typically, it was only necessary to convert video to images at a rate of one frame per second, which greatly reduced the total storage space needed.

Raw images and movies of the flow are excellent for getting an overall view of the dynamics and identifying qualitative features of interest, but for more quantitative analysis, some method for mapping images to velocity fields is required. A freely available software package called Correlation Imaging Velocimetry (CIV) was chosen for this purpose [19]. In brief, CIV works by measuring

the translation, rotation, dilation and shear of arbitrary dye or tracer patterns in a flow. More conventional particle tracking imaging velocimetry (PTIV) techniques simply track individual tracer particles in the flow. The two methods are contrasted in Figure 5.9.

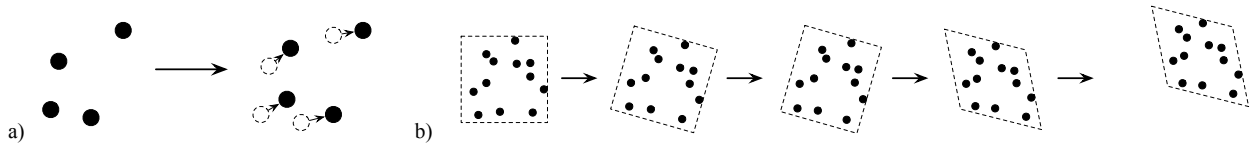

Figure 5.9: a) PTIV tracks tracer particles in order to build a picture of the Lagrangian velocity field. b) During the course of a flows evolution, arbitrary patterns will continuously undergo affine transformations (shown decomposed for clarity). CIV uses image recognition techniques to convert the motion of these patterns to Eulerian velocity fields.

The main disadvantages of PTIV are the high noise levels associated with particle tracking and an inability to accurately observe divergent regions of the fluid[2]. CIV does not suffer from either of these drawbacks. In addition, velocity field resolution is much less dependent on the choice of tracer material. In many circumstances it effectively becomes dependent on the resolution of the camera itself.

The CIV algorithm is iterative, with several steps needed before accurate high resolution velocity fields can be derived. After an initial low resolution image correlation using translation only (CIV1), false velocity vectors are removed from the data according to user-defined criteria, such as degree of correlation. The velocity fields are then interpolated onto a regular grid and the full CIV analysis is performed, usually at higher resolution, with the initial data used by the algorithm as a first estimate. After further false vector removal, the data is then interpolated onto a polar grid. The entire process is summarised as a block diagram in Figure 5.10. As an example, Figure 5.11 shows images and plots of various quantities produced at different steps in the process for a typical experimental dataset.

As the digital camcorder used a MiniDV format, the raw video data was outputted in a partially compressed form. The error introduced by this was tested in the following way. Raw, uncompressed demonstration flow images (see Figure 5.12) were taken from the CIV website[3] and artificially compressed in Matlab using the same Discrete Cosine Transform algorithm (DCT) that is used for the MiniDV video format.

Both original and compressed images were then processed in CIV, and the resulting kinetic energy fields compared (see Figure 5.13). As can be seen, the two fields are qualitatively very similar. However, the compressed image clearly has an increased noise component at small scales.

To investigate the dependence of the noise component on scale, the two-dimensional Fourier power spectra of the velocity fields were also computed (also in Figure 5.13). One-dimensional power spectra for both cases were then derived in a standard way by binning data points according to their absolute wavenumber $|\mathbf{k}|$. The results are plotted in Figure 5.14. As can be seen, the two quantities match extremely closely until around $|k| = 0.1$ rad px^{-1}. In general, compression artificially increases kinetic energy at high wavenumbers by adding small-scale noise to the images.

[2]By definition, tracer particles will move away from a divergent region. In flows optimised for CIV analysis the particle density is much higher, so this is rarely as big a problem as for PTIV.

[3]*http://www.civproject.org*

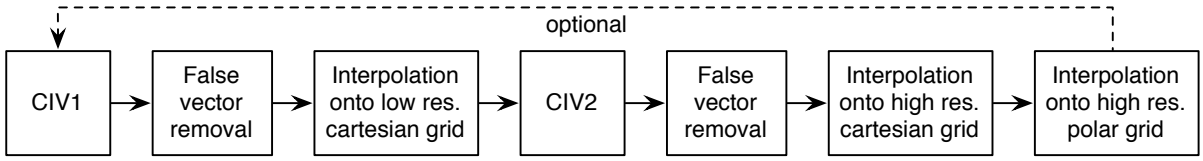

Figure 5.10: Block diagram of the main CIV algorithm.

As a result of this investigation, it was decided to limit spectral diagnostics of experimental data to modes with wavenumber greater than this value (in rad px^{-1}), where the compression error reaches around 10%. As will be seen in Chapter 6, this did not affect any of the main conclusions of our analysis.

Finally, for all higher level diagnostics on the experimental data, the commercial scientific software Matlab was used. Specific algorithms developed for experimental data processing are described in more detail in the next chapter.

5.2.3 Temperature data

From a theoretical point of view, temperature measurements of the interior flow in this experiment are extremely useful, as knowledge of velocity and temperature fields simultaneously allows one to derive potential vorticity. As described in Chapter 2, knowledge of the potential vorticity field can often give great insight into the dynamics of the fluid.

Two different methods were attempted for the acquisition of temperature information in the experiment. In the end, partly due to time and financial constraints, neither method proved accurate or reliable enough to provide useful information on the flow dynamics. The progress made is briefly described here, on the premise that it may provide a useful starting point for future experimental research.

The first and most ambitious method attempted involved the use of particle imaging thermometry (PIT) [14]. PIT is a technique whereby thermochromic liquid crystals are encapsulated in a transparent, neutrally buoyant polymer and then suspended in the fluid. The colour of the liquid crystals changes with temperature over a preset range. This allows a calibrated colour camera to visualise the local temperature of the illuminated region of the fluid.

PIT has the great advantage of providing two-dimensional maps of temperature at multiple levels, at potentially even higher resolution than the velocity fields derived by CIV. However, the technique requires high quality video equipment to obtain low-noise temperature data. Extremely bright light sources, such as ultra-bright LED arrays, are also required in order to obtain good quality results.

As a preliminary study, a small sample of thermochromic tracer particles was purchased from Hallcrest[4] and tested in a relatively high temperature difference ($\Delta T = 6\mathrm{K}$) experiment. The quoted colour range of the particles was 10K, centred on 293K, and characteristic particle size was of order 50-100 μm. An example image produced from this experiment, with fluid illumination at mid depth, is shown in Figure 5.15.

As can be seen, there is no discernable large-scale variation of colour with radius. In general it was

[4]Product details are available at *http://www.hallcrest.com/*.

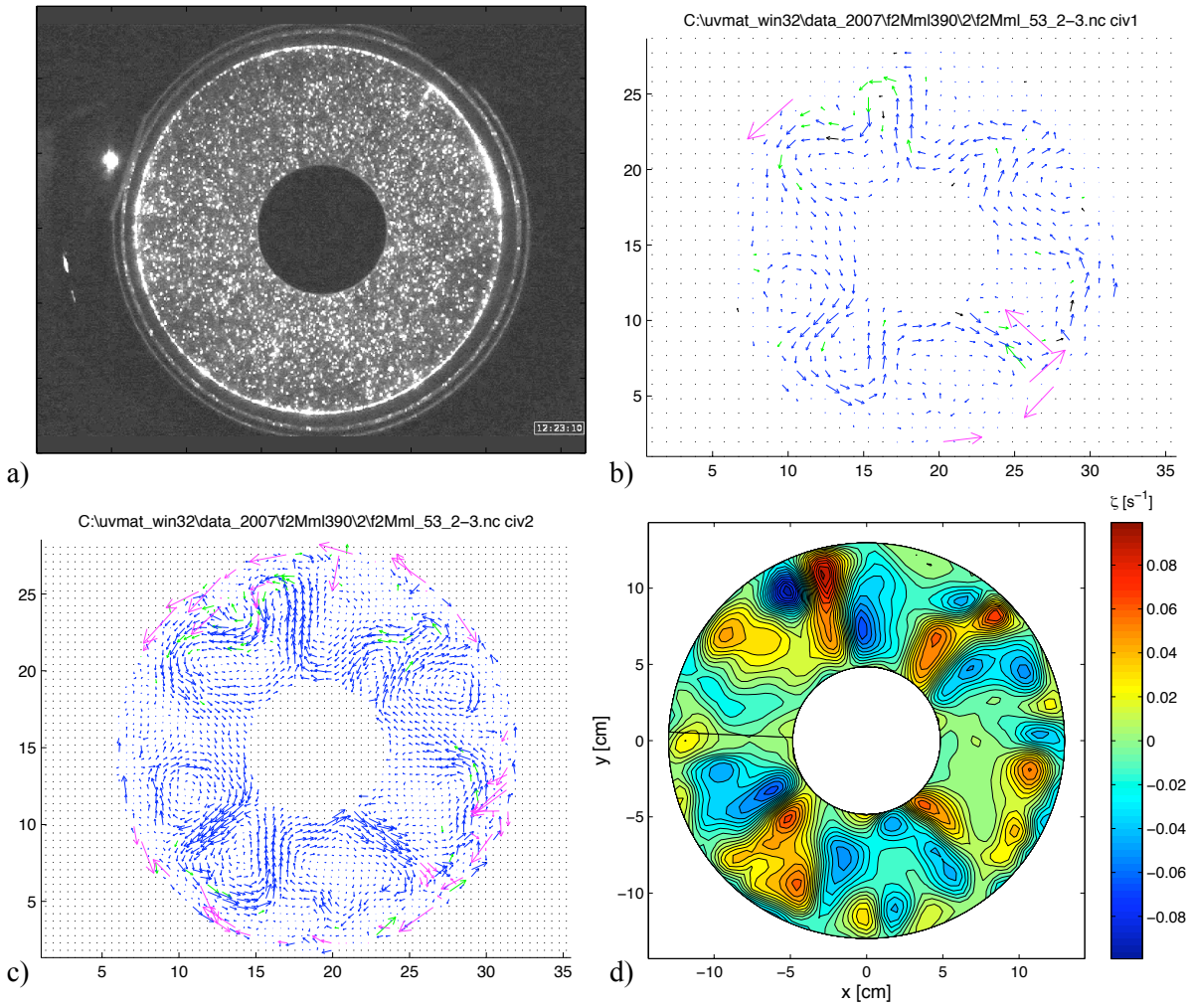

Figure 5.11: a) Raw image at mid-depth, b) CIV1 c) CIV2 velocity fields and d) final vorticity field in polar coordinates for data from a high rotation rate, flat boundary experiment. In b) and c), blue velocity vectors are well-correlated, green ones have average correlation, and pink ones are false vectors.

found that the halogen lamps did not provide sufficient illumination for the liquid crystals, with the result that any physical variations in tracer particle colour were below the noise threshold of the digital camcorder. Replacing the lighting and visualisation system was not judged possible within the budget of the DPhil, and hence the PIT method was reluctantly abandoned.

The second temperature acquisition method attempted involved placing thermocouples directly in the fluid. There are several disadvantages to this approach. First, the electronics required for each thermocouple means that in practice, the fluid temperature can only be recorded at a small number of points. Second, thermocouples must be connected to wires, and the presence of wires in the working fluid may affect its motion.

When the thermocouples were tested in the experiment, it was found that the flow was slightly altered by the presence of wires, although the effect was relatively slight. More seriously, the thermocouples were found to be corroding, and gave noisy, unpredictable signals for only a few

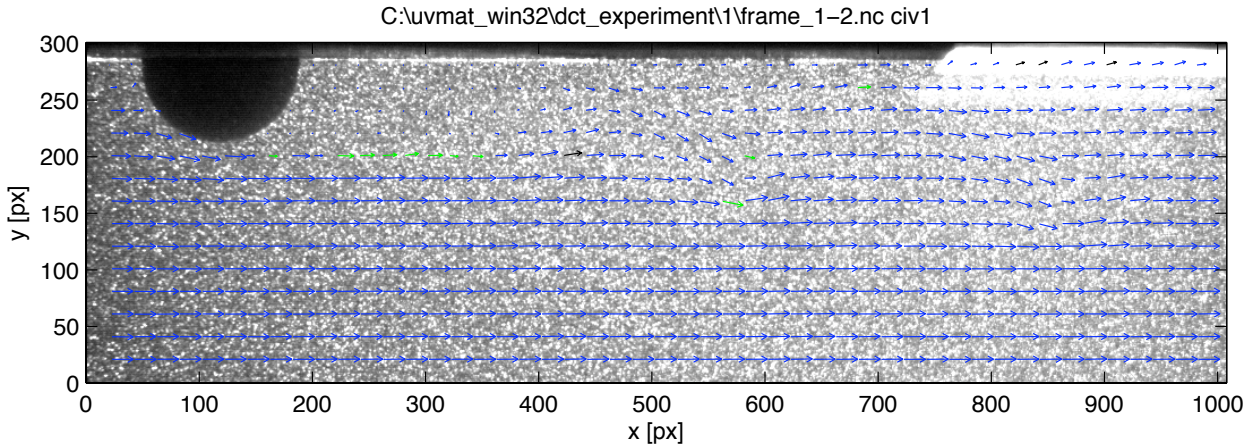

Figure 5.12: Uncompressed image downloaded from CIV website for test purposes, with derived CIV2 velocity field superimposed.

hours before shutting down completely. Many attempts were made to fix this problem; the metal walls of the annulus were electrically grounded, more robust thermocouple wire was used, and finally the wire was coated in vacuum-grade protective varnish. Unfortunately none of these alterations increased the reliability and accuracy of the thermocouples to a satisfactory degree.

Due to these two problems it was decided not to use thermocouples to measure the interior fluid temperature, although some thermocouples were still used to check the temperature of the inner and outer annuls walls. In general, PIT appears have much greater potential as a method for measuring the temperature of the fluid interior, as long as accurate calibration of the colour images is possible. If temperature measurements are desired in future experimental work, it is therefore recommended that this method be pursued first.

5.3 Experimental problems

Throughout the course of the DPhil, experimental progress was severely impeded by equipment failure. Both the annulus and the rotating rig itself required fairly extensive repair, the details of which are summarised for future reference in this section.

Problems with the annulus were primarily due to a combination of equipment age and poor original design. Concerning the latter, a most serious problem involved the use of diametral O-ring seals in the outer water jacket of the annulus, which were inadequate given the large outer wall radius (14.5 cm). The apparatus had clearly failed several times in the past, as multiple layers of silicone sealant had been applied to the outside of the seal, presumably in an unsuccessful attempt to halt the leakage. After several months of experimentation, a solution was proposed whereby new O-rings were placed in a different location in the wall that allowed for compressive sealing. All silicone was removed and Apiezon T grease was applied to increase the reliability of the seal. The second annulus leakage problem occurred in the newly manufactured inner cylinder. The reasons for the leak were similar; silicone was used instead of O-rings as a sealant. The solution involved a chamfered aluminium bracket fitted around the base of the cylinder, as shown in Figure 5.16.

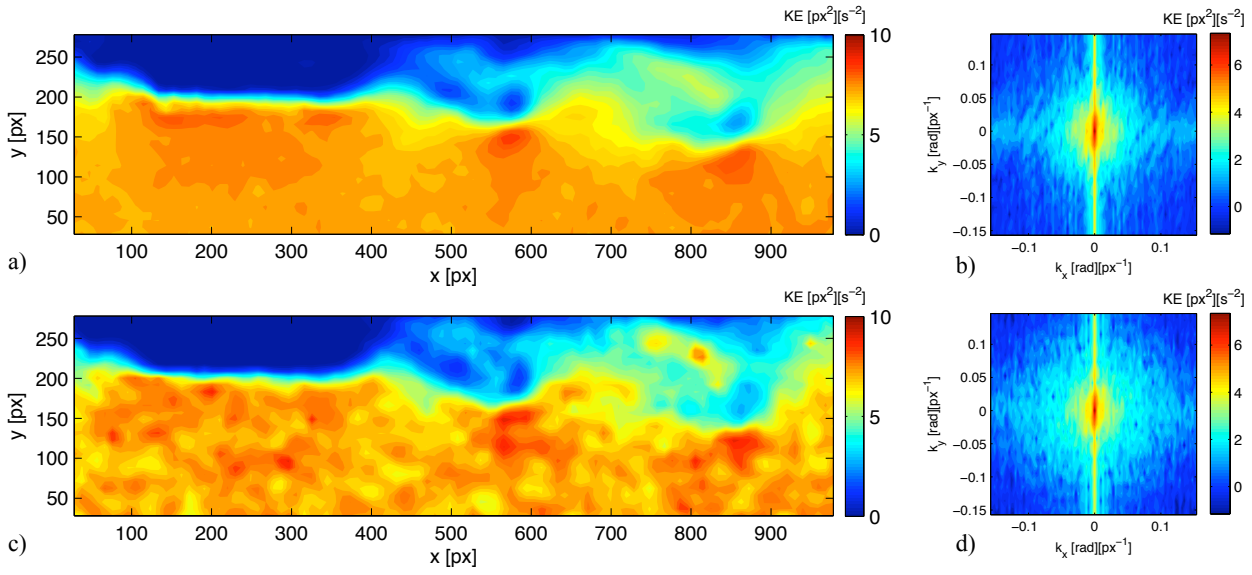

Figure 5.13: a) Kinetic energy in real space and b) spectral space for the uncompressed CIV test images. c), d) The same plots for images compressed using the DCT algorithm.

The second set of experimental problems involved equipment on the turntable itself. Some of these were minor: both water filters and one of the ceramic heaters in the thermal control circuit required replacement, the Eurotherm temperature controller caused oscillations and required manual calibration, and the camcorder mount was unstable and needed modification. A most persistent problem was non-constant rotation of the turntable, which caused a rapid 'wobble' of the zonal mean flow velocity. Extensive work was carried out in an attempt to correct this. First, the experimental annulus was leveled and centred using a spirit gauge and tripod-mounted sighting telescope. Second, the turntable was removed from its base with the use of a crane and the bearings and brushes of the DC motor were replaced. Electrical repair of the power slip-ring was also carried out at this time by technical staff.

Unfortunately neither of these attempted solutions completely removed the oscillations. In a final attempt to correct the problem, a load sensor placed underneath one support leg of the rotating rig. By this method, it was determined that the mass distribution of equipment on the table was non-uniform. This problem was corrected by bolting various lead counterweights around the turntable perimeter, until an even mass distribution was achieved.

After all these measures, only very small oscillations at high rotation rate still remained. These oscillations were high frequency and low amplitude in comparison to the observed fluid motion in the annulus, and it was judged that their effect on the dynamics would be extremely small. Indeed, in CIV-derived velocity fields the oscillations could not be distinguished from the background noise due to other effects, such as the non-optimal lighting system, and the camcorder data compression discussed in Section 5.2. In the analysis of the experimental data in Chapter 6, therefore, their effects are neglected.

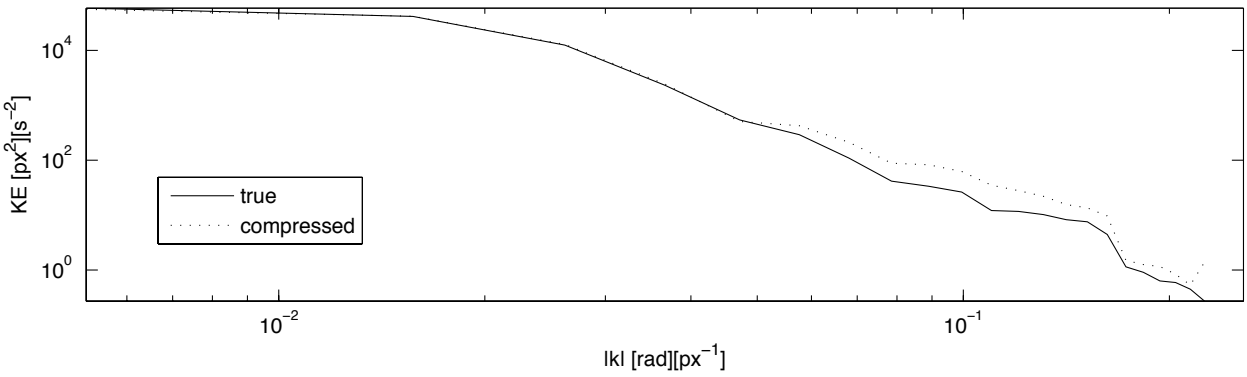

Figure 5.14: One-dimensional kinetic energy spectra for velocity fields derived from compressed (black line) and uncompressed (red line) images.

5.4 Discussion

In this chapter, a comprehensive description of the experimental setup was given. As the data acqusition system involved new technology and methods, particular attention was paid to describing it in detail. A brief summary was also given of the problems encountered during the setup and calibration phase of the experimental project. Finally, some research performed on the implementation of a multi-level two-dimensional temperature acquisition system was also described.

The apparatus described here is innovative in many respects. The flow visualisation setup in particular proved extremely successful, validating the use of digital camcorders and wireless technology in rotating fluid dynamics experiments. Also, the combination of simple electronics and an image sorting algorithm allowed for the automated reconstruction of effectively four-dimensional velocity fields from the raw experimental data.

However, there are still many ways in which this experimental setup could be improved in the future. Use of an industrial FireWire camera, for example, would allow more flexible data collection, and would eliminate the problems caused by video compression. Replacement of the halogen lamps with an array of ultra-bright LEDs would also simplify the setup, as it would remove the need for the exterior cooling fans. Furthermore, the *combination* of a high quality camera with LED lighting would make it much easier to create a reliable particle imaging thermometry system in the future.

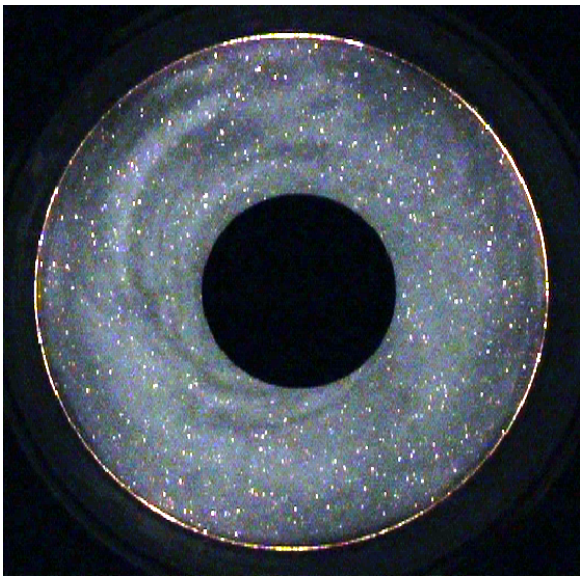

Figure 5.15: Image of working fluid at mid-depth with PIT tracers added, for an experiment with $\Omega = 2$ rad s^{-1} and $\Delta T = 6$K. Image brightness has been increased for clarity.

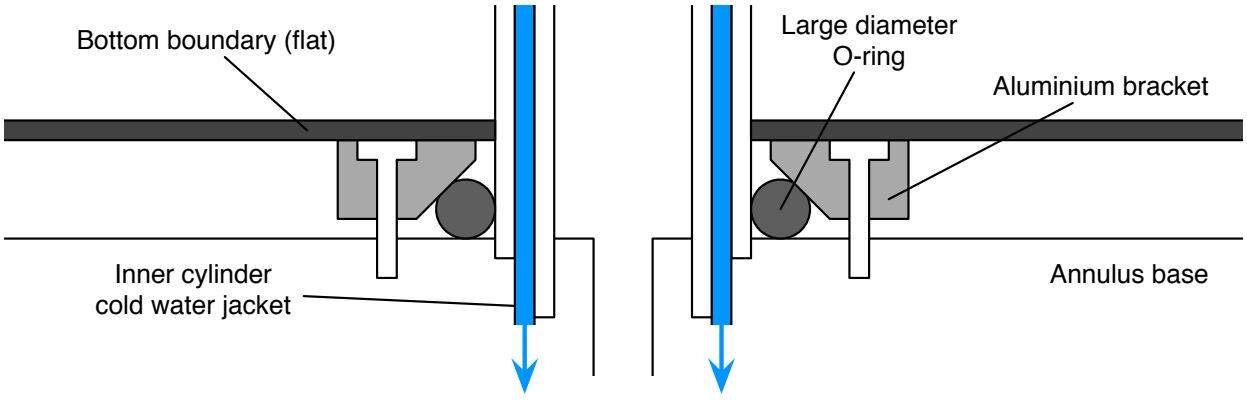

Figure 5.16: Schematic of the double seal O-ring designed and installed with the help of G. A. Clack.

Chapter 6

Experimental results

In this chapter, the main experimental results of this DPhil are presented. In the first section, the entire set of experiments performed is summarised in terms of a regime diagram, and general flow features and properties are discussed. Next, a series of increasingly sophisticated analyses are performed on a selection of the most interesting datasets, with the central aim of gaining insight into the turbulent jet formation process.

6.1 General flow features

As was discussed in Chapter 5, the experiments presented here were designed to investigate a parameter space region of high Taylor and low Hide number. The locations in parameter space of all experiments are shown in Figure 6.1. Also shown, for comparison, is a regime diagram from a previous laboratory study by Hignett et al., performed at lower Taylor number [30]. In this investigation, rotation rate and temperature difference were varied from $\Omega = 0.65$ rad s^{-1} to 3.9 rad s^{-1} and $\Delta T = 1$K to 4K to cover the parameter space range indicated. For reference, the Taylor and Hide numbers for all Ω and ΔT combinations studied are also given in Tables 6.1 and 6.1.

Ω[s^{-1}]/ΔT [K]	0.65	1.3	2.6	3.9	3.9*
1	1.412×10^7	5.649×10^7	2.260×10^8	-	-
2	1.412×10^7	5.649×10^7	2.260×10^8	5.084×10^8	1.714×10^9
4	1.412×10^7	5.649×10^7	2.260×10^8	5.084×10^8	1.714×10^9

Table 6.1: Taylor number as a function of rotation rate and temperature difference. The asterisk in the final column indicates 'fluid B' experiments.

Ω[s^{-1}]/ΔT [K]	0.65	1.3	2.6	3.9	3.9*
1	0.199	0.050	0.012	-	-
2	0.397	0.099	0.025	0.011	0.011
4	0.794	0.199	0.050	0.022	0.022

Table 6.2: Hide number as a function of rotation rate and temperature difference. The asterisk in the final column indicates 'fluid B' experiments.

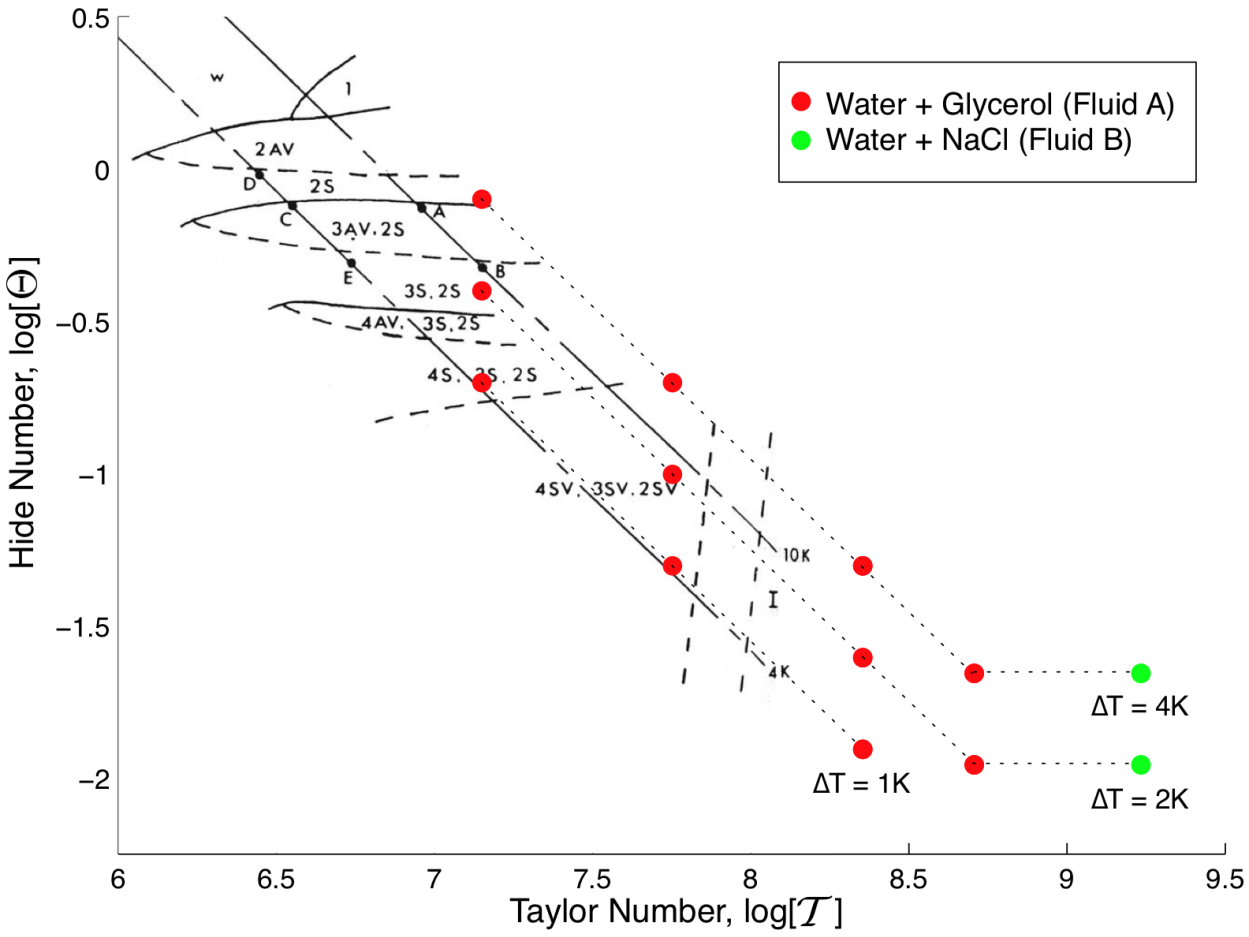

Figure 6.1: Logarithmic parameter space diagram showing the position of all experiments conducted as a function of Taylor and Hide number ($\mathcal{T}$ vs. Θ). Also shown in black is a regime diagram derived from a previous experimental study (see [30] for details).

As can be seen, only a total of four lower viscosity 'fluid B' experiments (one flat and one sloping experiment at two points in parameter space) were carried out. The reason for this was that the salt contained in fluid B slowly corroded the metal annulus walls over time, making extensive data collection extremely impractical.

As the principal interest of this investigation was the (statistically) steady-state properties of the flow, each experiment was run for two hours, with data collection occurring only in the second hour. The Ekman spinup time, defined as $\tau_{Ek} = h/\sqrt{2\nu\Omega}$, varies between 160 and 65 seconds for the experiments presented here; thus a minimum of 22 spinup times (40 for the high rotation rate experiments) passed before data collection in each case. Visual inspection of mid-level streak images during data collection typically revealed little qualitative change in the flow fields after half an hour of run time.

As a further test of flow stationarity, total energy and enstrophy were plotted as a function of time for each dataset after CIV processing. It was found that in all cases, these quantities did not exhibt any significant monotonic trend over the period observed. An example plot, for a flat boundary experiment with rotation rate $\Omega = 3.9$ rad s^{-1} and forcing $\Delta T = 2$K, is shown in Figure 6.2.

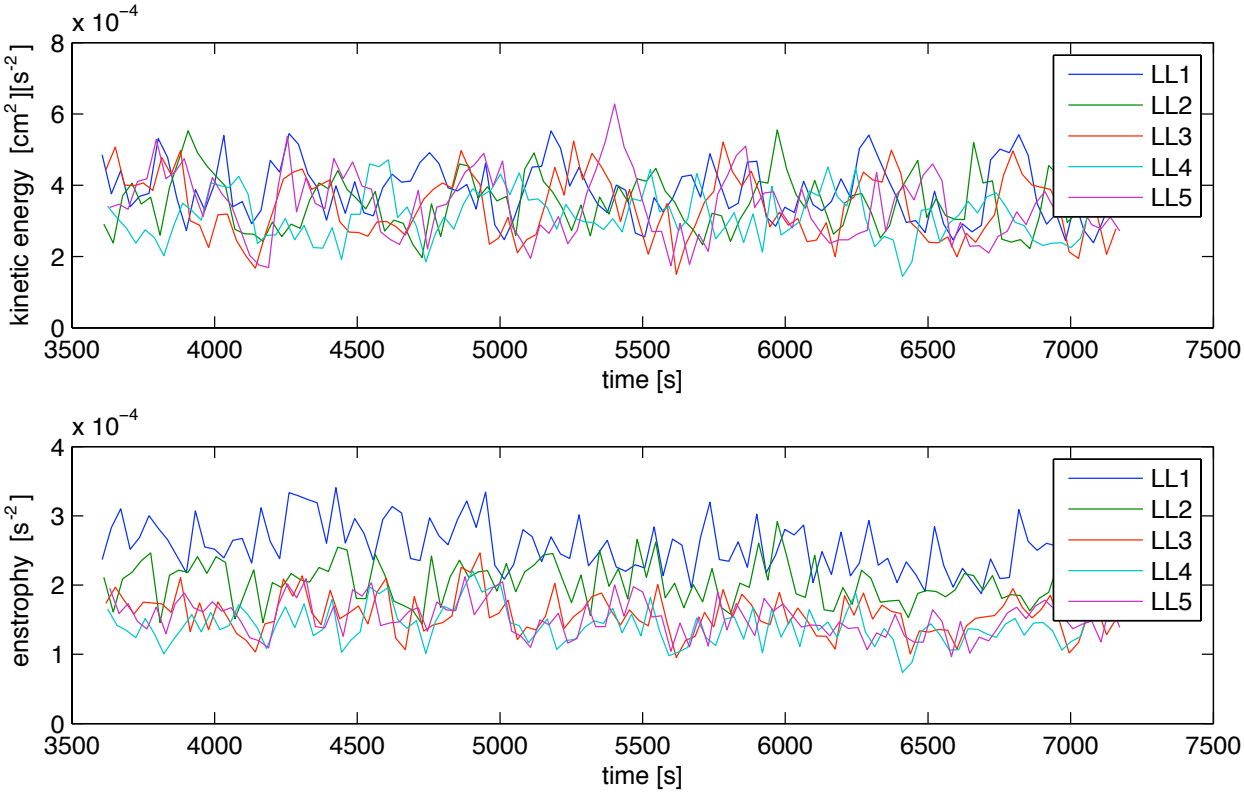

Figure 6.2: Total energy (top) and enstrophy (bottom) at five different depths for a high Taylor number flat boundary experiment. The codes 'LL1' etc. correspond to the light levels indicated in Figure 5.1.

To give a rough idea of the qualitative flow features before CIV analysis, streak images of the experiment at mid-depth were produced by time-averaging sets of raw images outputted from the digital camcorder. Figure 6.3 shows such images of the flow for flat and sloping boundary experiments at a) low and b) high rotation rates. Each image was taken after approximately 30 minutes of evolution time, with an averaging time of 20 seconds.

The top streak images in Figure 6.3 are from experiments where the rotation rate is low enough for the flow to be chaotic rather than fully turbulent, at least in the flat boundary case. There, the flow appears to be in a structurally vacillating 'wavenumber 4' state (4SV), which is in agreement with the parameter space diagram recorded in [30] (Figure 6.1). In the sloping case, a wavy jet close to the outer boundary is apparent, with the inner half of the channel dominated by a chain of moving vortices.

The bottom streak images in Figure 6.3 show more complicated behaviour. The flows for both are fairly rapidly fluctuating; the flat boundary case, in particular, exhibits varying radial and azimuthal eddy motion, with no single wavenumber dominating.

In the sloping case, the large-scale domain spanning eddies are replaced by apparent wave-like motion and weak zonal jets. It is interesting to note that the bottom-right image in Figure 6.3 is somewhat reminiscent of the streak images reported previously in a quite different setup [13]; there, a rotating parabolic dish was heated from below and allowed to cool convectively at its upper

surface. However, little quantitative velocity field information was derived for that experiment, making further comparison difficult.

Figure 6.4 shows CIV-derived contour plots of near-instantaneous vertical vorticity component $\zeta = r^{-1}\left(\partial_r(ru_\theta) - \partial_\theta u_r\right)$ at three different depths in the fluid, for experiments with the same parameters as those displayed in Figure 6.3. Three-dimensional visualisation of this type helps to highlight the dramatic difference between the flow in the flat and sloping boundary cases — note in particular the pronounced wavelike appearance of the latter plots (bottom) in Figure 6.4. Animations of the vorticity field show that the wave crests are travelling westward, as expected for disturbances that are qualitatively similar to atmospheric planetary waves. In Section 6.2, we discuss a temporal spectral analysis of the velocity field data that shows that to a large extent, these flows are indeed dominated by wavelike motion.

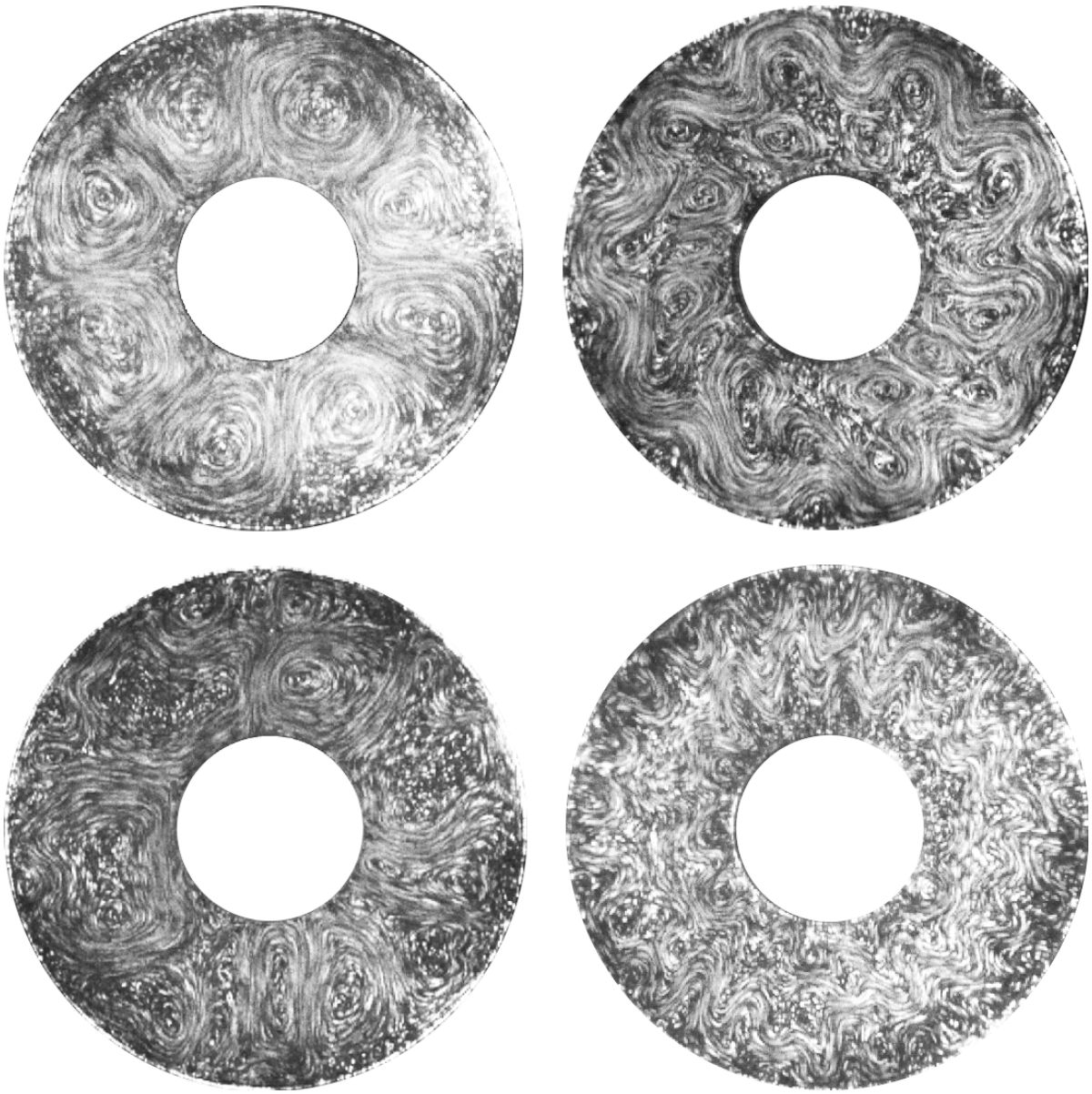

Figure 6.3: Streak image comparison of the mid-depth flow in flat (left) and sloping (right) boundary cases for low rotation rate $\Omega = 1.3$ rad s^{-1} (top) and high rotation rate $\Omega = 3.9$ rad s^{-1} (bottom).

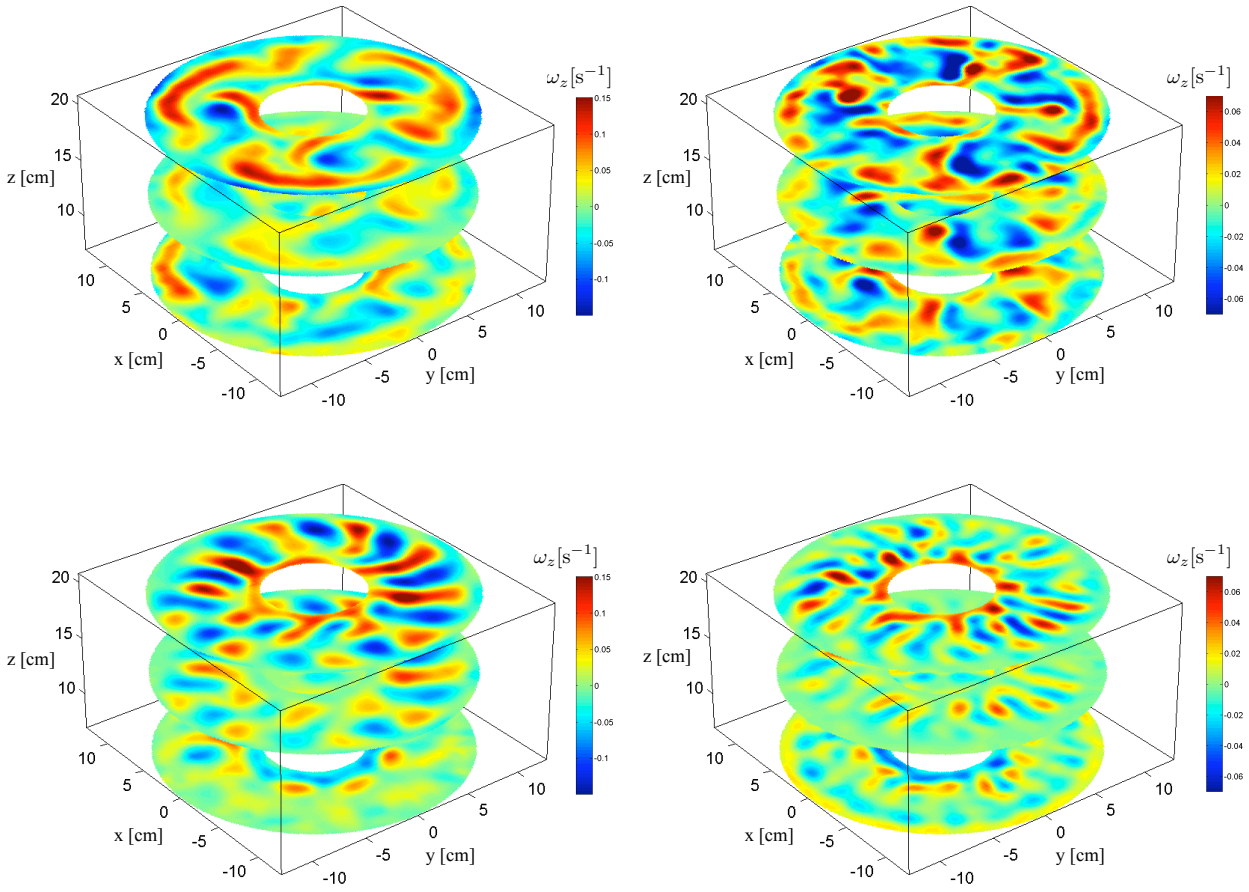

Figure 6.4: Multilevel snapshot of vertical vorticity component at levels 1, 3 and 5, time $t = 3600$s for flat boundary (left) and sloping boundary (right) experiments with $\Omega = 1.3$ rad s^{-1} (top) $\Omega = 3.9$ rad s^{-1} (bottom) and $\Delta T = 2K$ in all cases. Note that in the slow flat boundary experiment (top left), azimuthal wavenumber 3, not 4, is dominant. The data there is from a different experimental run to the streak image in Figure 6.3, although the temperature difference and rotation rate in both cases was identical. This demonstrates the hysteretic properties of the system, as observed previously by other researchers (e.g., [28] [29]).

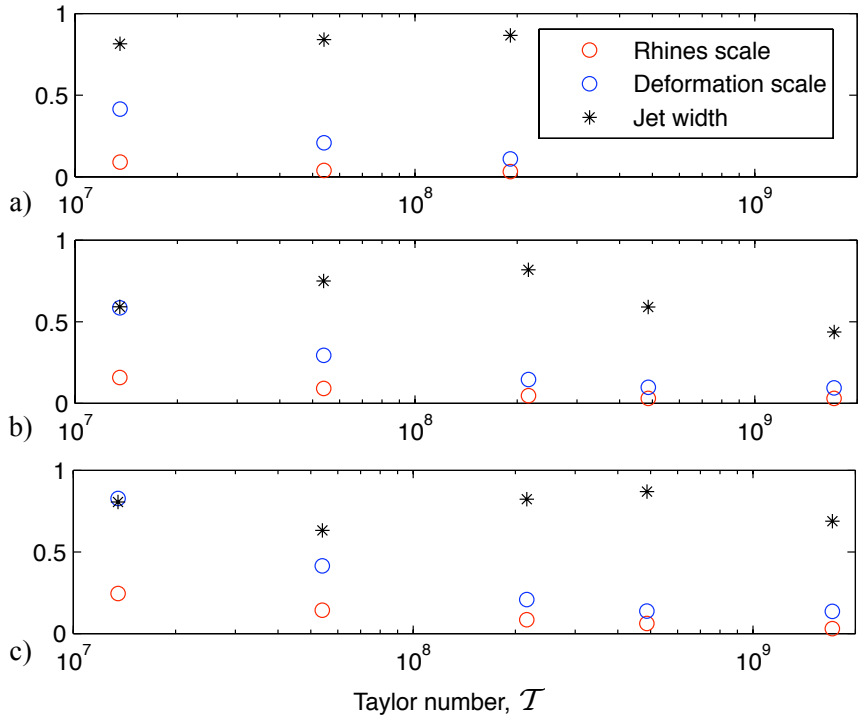

Figure 6.5: Relevant length scales in units of channel width $(b-a)$ as a function of Taylor number for a) $\Delta T = 1K$, b) $\Delta T = 2K$ and c) $\Delta T = 4K$ sloping boundary runs.

A selection of relevant length scales as a function of Taylor number for all the sloping boundary experiments is plotted in Figure 6.5. The Rhines scale (2.59) was calculated using a time and volume averaged value for the root mean square flow speed U. The jet scale was crudely estimated by Fourier transforming the zonal and temporal mean of the azimuthal velocity $\overline{u}_\theta$ in radius. The location of the peak of the resulting power spectrum was then taken to be the characteristic jet wavenumber, with jet scale the inverse $L_{jet} = \pi/k_{jet}$.

The first internal deformation radius in the experiments is defined as

$$L_d = \frac{\sqrt{\alpha g d \Delta T_z}}{\Omega} \tag{6.1}$$

where ΔT_z is the vertical temperature difference. Although we do not have internal temperature information for these experiments, an upper bound on the deformation radius $L_{max} > L_d$ can be derived by replacing ΔT_z in (6.1) with the imposed horizontal temperature gradient ΔT. This quantity is also plotted in Figure 6.5.

Note that this 'horizontal deformation scale' decreases with Taylor number, becoming less than $1/10^{\text{th}}$ of the channel width for the highest rotation rate experiments. The Rhines scale for the sloping boundary runs also decreases with Taylor number, primarily because β increases with Ω. Neither length scales are good *quantitative* predictors for the observed jet width, although note that for Taylor numbers greater than $\mathcal{T} \approx 2 \times 10^8$ for the $\Delta T = 2K$ runs, all three scales are at least decreasing in the same direction.

In the $\Delta T = 1K$ experiments, the observed flow was generally extremely weak. A large number of

particles would generally sink to the bottom or rise to the top of the annulus before data acquisition began, increasing the errors on the CIV-derived velocity fields. In addition, zonal jet formation was not conclusively observed. It is most likely that Ekman and viscous damping dominated over nonlinear effects in those cases, suppressing the jet formation process. In the $\Delta T = 4K$ experiments, acquisition of high-quality data was possible. However, even at high rotation rates *multiple* zonal jets did not usually form (the one exception to this was a high rotation fluid B experiment — see Figure 6.8). It was only in the $\Delta T = 2K$ experiments that multiple zonation was conclusively observed.

In Figures 6.6, 6.7 and 6.8, instantaneous mid-depth vorticity ζ (left) and zonal velocity $u_\theta = r\dot{\theta}$ (right) after 1.5 hours run time are plotted for a range of $2K$ and $4K$ temperature difference experiments.

Several important flow features may be seen from these plots. Firstly, in both flat and sloping boundary experiments, the scale of spatial variations in both fields tends to decrease with rotation rate. In the flat boundary experiments, the azimuthal wavenumber $m = 3$ flow that is dominant at low rotation rates becomes replaced by an unstructured flow, with no evidence of coherent zonal structure formation found in any of the cases.

In the sloping boundary experiments, however, alternating jets appear at higher rotation rates; the 'fluid B' experiments, in particular (Figure 6.8), have a clear 2-3 jet structure. It is most interesting to note that regions where the jets are strong tend to correspond to those where wave activity, as visible in the instantaneous vorticity fields, is highest. Also clearly apparent is the increase in wavenumber (both azimuthal and radial) of the vorticity fields with rotation. These issues are examined further in the next two sections.

The velocity and vorticity snapshots are from flows that were approximately in a statistically steady state. It is therefore also of interest to examine time-averaged zonal velocity profiles. In Figures 6.9 and 6.10, time and zonal-averaged zonal velocity $\overline{u}_\theta$ is plotted as a function of r and z for a variety of cases. All time averages performed in this chapter and the next involved from 100 to 220 instantaneous fields, depending on the temperature difference. Larger temperature differences resulted in greater horizontal velocities, and hence required more rapid sampling. In every case, the total averaging time was one hour.

As can be seen, the low rotation rate, flat boundary zonal velocity profiles show a strongly vertically sheared zonal flow. This is of course the thermal windshear, predicted from geostrophic arguments (recall the discussion of Chapters 1 and 2), which causes eddy growth in the annulus when it is baroclinically unstable. Note, however, that this shear is weakened in the centre of the channel. This is due to nonlinear interaction with the finite amplitude eddies. As all the energy of the eddies is ultimately derived from the vertical shear of the zonal flow, it is inevitable from a conservation of energy argument that they must weaken it as they grow.

As rotation rate is increased, the effect of the eddies becomes more and more important. In the highest Taylor number case (bottom right of Figure 6.9), the now turbulent eddy motion has distorted the zonal flow profile to such an extent that it is mainly vertically coherent (barotropic).

The sloping cases are generally different, although they appear qualitatively similar at low rotation rates. As expected from the mid-level snapshots, there is a noticeable trend towards multiple jet formation as rotation rate is increased. Interestingly, however, even at the highest rotation rates, the jets produced still have a strong baroclinic element. We note that this was also found to be the case in the simplified numerical simulations of the experiment (see Chapter 8).

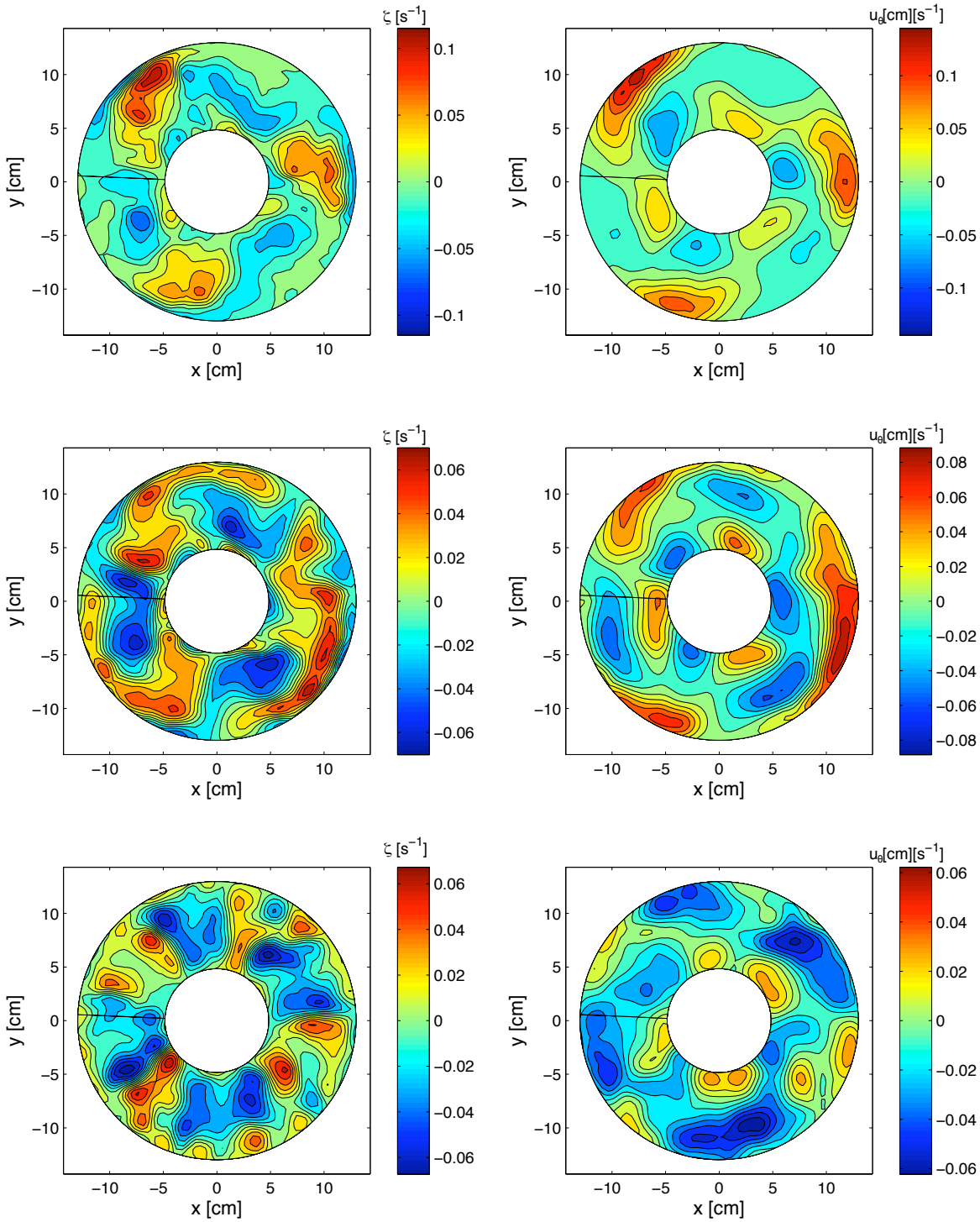

Figure 6.6: Snapshots of mid-depth vorticity (left) and zonal velocity (right) for flat boundary experiments with constant temperature difference $\Delta T = 2K$. Rotation rate is $\Omega = 0.65$, 1.3 and 3.9 rad s^{-1}, increasing from top to bottom.

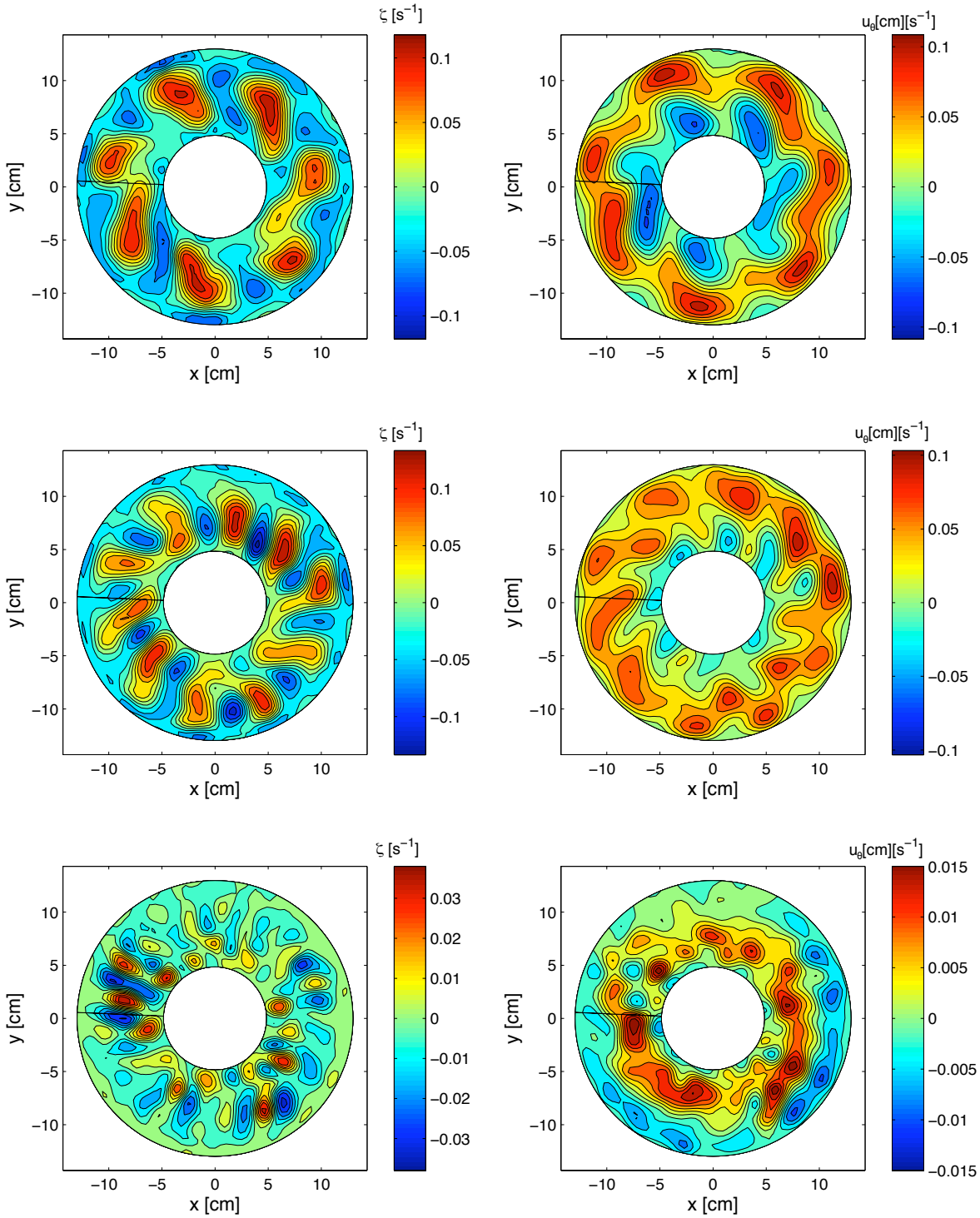

Figure 6.7: Snapshots of mid-depth vorticity (left) and zonal velocity (right) for sloping boundary experiments with constant temperature difference $\Delta T = 2K$. Rotation rate is $\Omega = 0.65$, 1.3 and 3.9 rad s^{-1}, increasing from top to bottom.

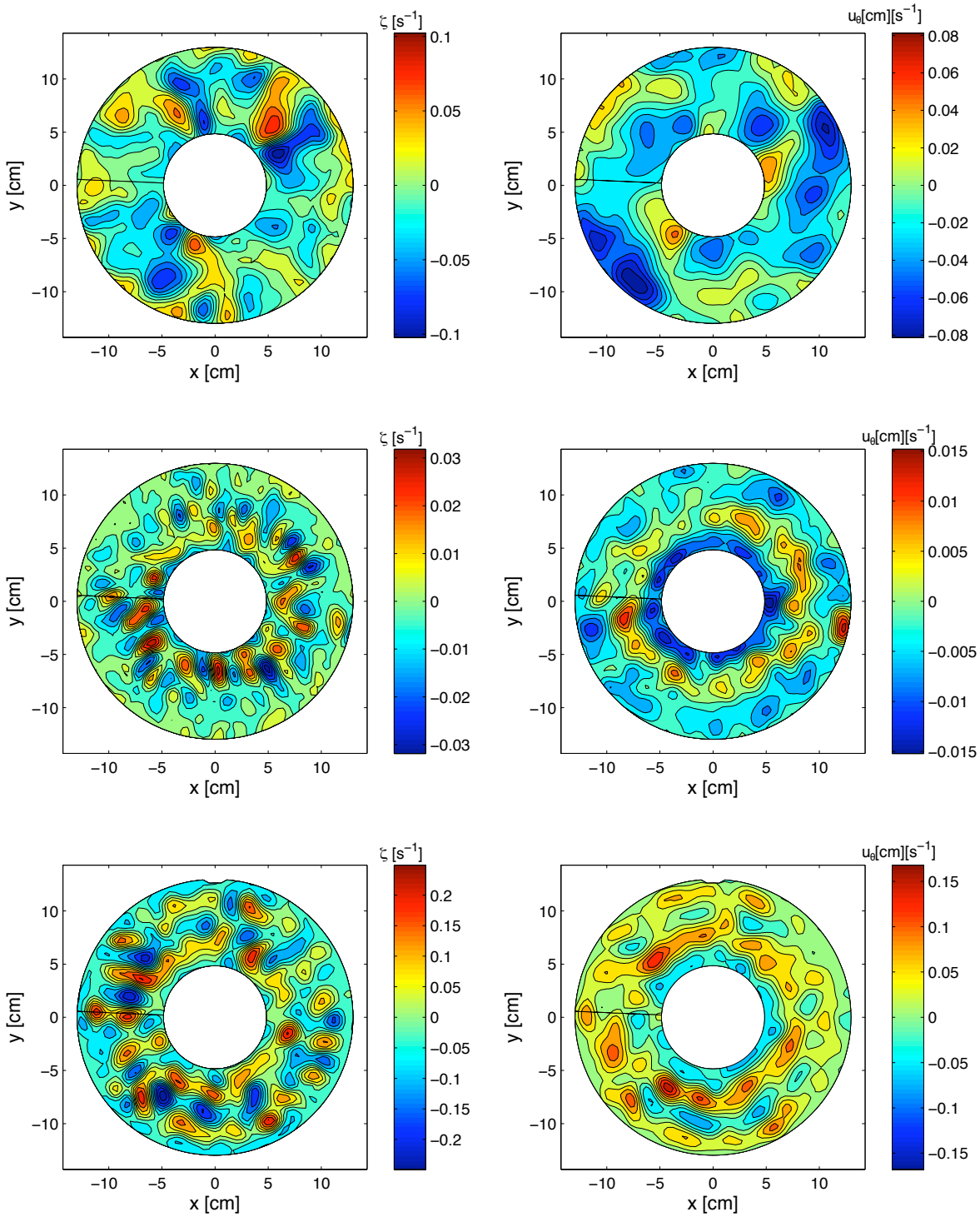

Figure 6.8: Snapshots of mid-depth vorticity (left) and zonal velocity (right) for a selection of low viscosity 'fluid B' experiments at high rotation rate $\Omega = 3.9$ rad s^{-1}. From top to bottom they are: flat boundary $\Delta T = 2K$, sloping boundary $\Delta T = 2K$ and sloping boundary $\Delta T = 4K$.

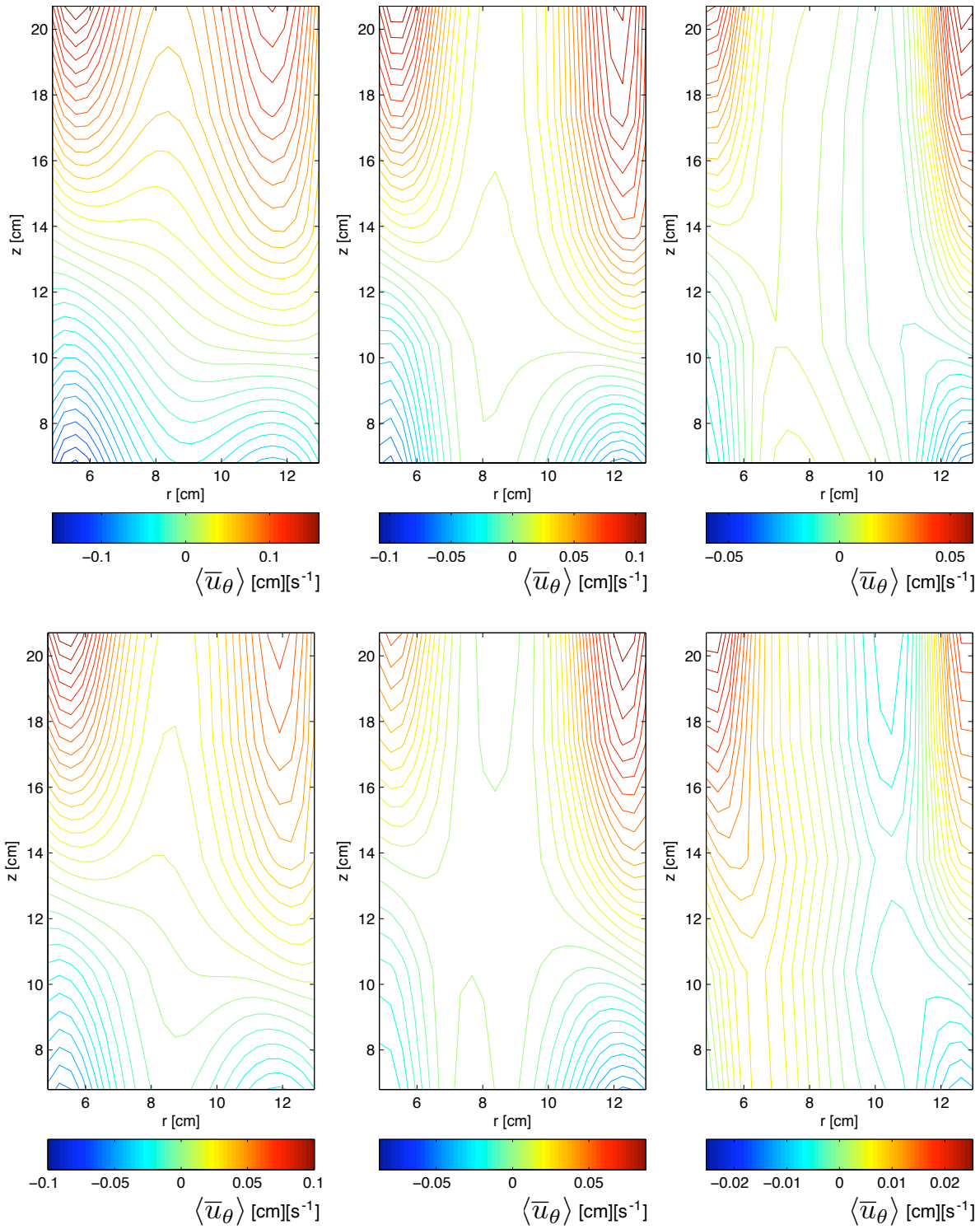

Figure 6.9: Time-averaged zonal velocity as a function of r and z for $\Delta T = 4K$ (top) and $\Delta T = 2K$ (bottom) flat boundary experiments, with increasing rotation rate $\Omega = 0.65$, 1.3 and 3.9 rad s^{-1} from left to right.

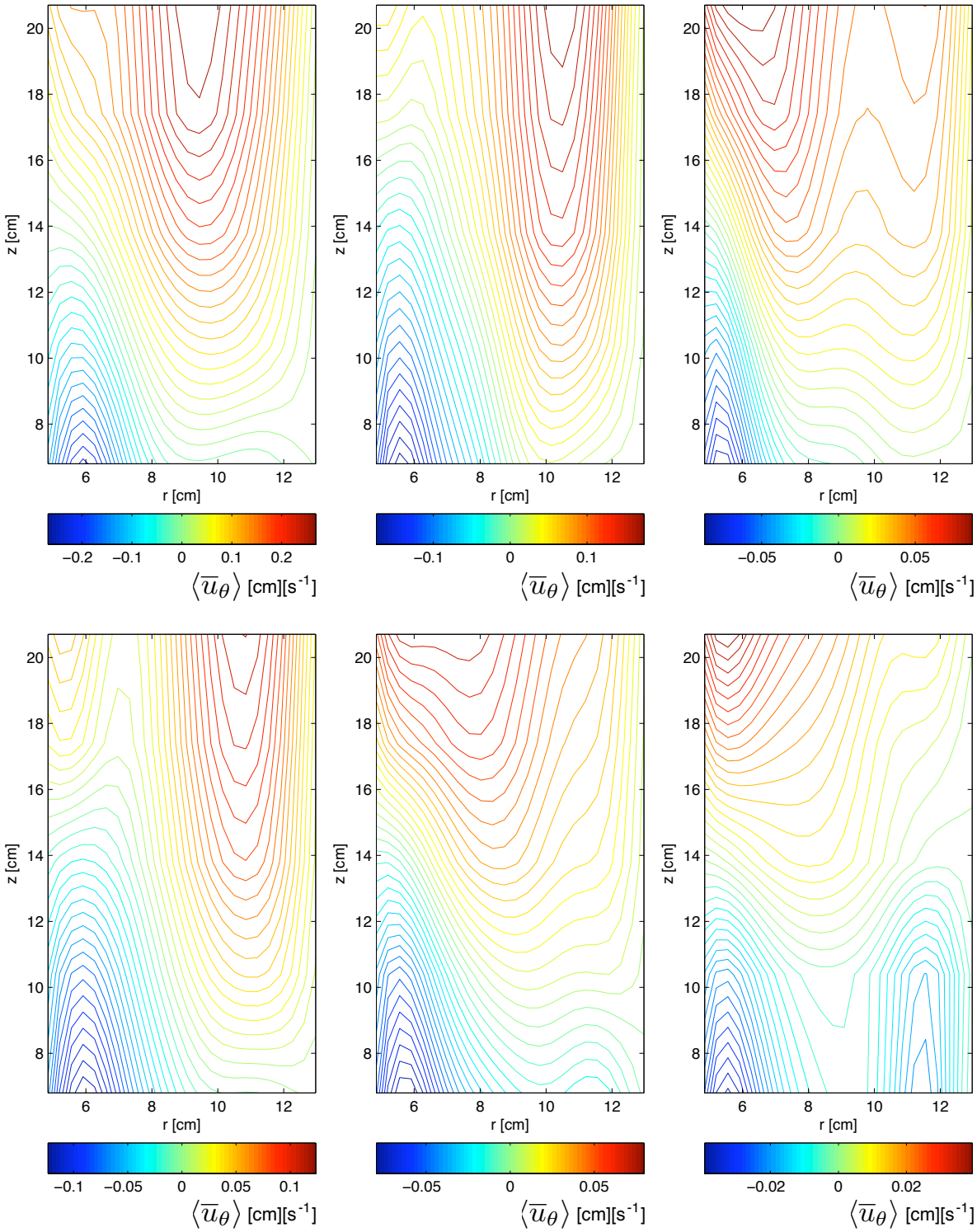

Figure 6.10: Time-averaged zonal velocity as a function of r and z for $\Delta T = 4K$ (top) and $\Delta T = 2K$ (bottom) sloping boundary experiments, with increasing rotation rate $\Omega = 0.65$, 1.3 and 3.9 rad s^{-1} from left to right.

6.1.1 Eddy-mean flow interaction

As discussed in Chapter 3, the effect of eddies, be they wavelike or turbulent, on zonal mean quantities, can be written in terms of the averaged correlation of the various eddy fields. In this section we examine the eddy (angular) momentum flux, $\langle\overline{u_r' u_\theta'}\rangle$, and temperature flux, $\langle\overline{u_r' T'}\rangle$ for the experimental data, and compare them to the observed time-averaged zonal flow profiles.

Due to the problems discussed in Chapter 5, temperature information could only be derived in an indirect way via the quasigeostrophic approximation. First, streamfunction ψ' was derived numerically from the eddy vorticity fields, by computing the inverse laplacian $\psi' = \nabla^{-2}\zeta'$ with boundary conditions $\psi'|_{r=a,b} = 0$. The calculation was performed using standard matrix inversion methods in the Matlab software package. For further details of the calculation, see Appendix B.

To relate T' to ψ', the definition of geostrophic streamfunction $\psi' \equiv p'/2\Omega\rho_0$ can be used. When combined with the hydrostatic approximation $dp' = -g\rho' dz$ and the linearised temperature-density relationship $\rho' = -\rho_0\alpha T'$, this allows us to write the approximate relationship between eddy temperature and streamfunction as

$$T' = +\frac{2\Omega}{g\alpha}\frac{\partial\psi'}{\partial z}. \tag{6.2}$$

In Figure 6.11, time and zonal averaged eddy heat and momentum fluxes are plotted beside the time-averaged zonal flow for a selection of the most interesting experiments. The fluxes were calculated at mid-depth for these plots. Interestingly, however, the differences between mid-depth and vertically averaged values were small in most cases.

First, note that for all experiments the eddy heat flux $\langle\overline{u_r' T'}\rangle$ is negative, indicating that the eddies are *always* transporting heat from larger to smaller radii. This is expected, as the radial temperature gradient is the only energy source in the experiment. Indeed, the baroclinic instability can be regarded as a heat engine, creating jet and eddy motion through the conversion of thermal to kinetic energy.

In all of the sloping boundary cases (Figures 6.11(b-e)), the eddy momentum flux $\langle\overline{u_r' u_\theta'}\rangle$ is converging onto same-sign zonal flow, indicating that barotropic eddy processes are forcing the jet in each case. However, in Figure 6.11(a) (the flat boundary case) positive eddy momentum flux is converging on a *negative* zonal jet. This is an indication that the zonal flow may be losing kinetic energy to the eddies there.

In flows with significant vertical and horizontal variation such as those analysed here, assessment of the net exchange of total energy between eddies and zonal flow is generally non-trivial [46]. To gain further clues as to the nature of jet-eddy interaction, however, we can use the *Rayleigh-Kuo instability criterion*

$$\beta - \partial_r\left(r^{-1}\partial_r\left(r\overline{u_\theta}^{\theta z}\right)\right) \leq 0 \tag{6.3}$$

where $\overline{u_\theta}^{\theta z}$ is the vertically and zonally averaged velocity, to assess whether or not the purely barotropic zonal mode is dynamically unstable.

In the course of the experimental analysis, the Rayleigh-Kuo criterion for barotropic instability was analysed for all datasets. It was found that it was usually satisfied in the high rotation rate flat boundary experiments, but never in the sloping ones. It is judged likely, therefore, that the positive momentum flux convergence seen in Figure 6.11(a) is due to barotropic (or mixed barotropic / baroclinic) instability of the negative zonal flow.

More sophisticated eddy-mean analyses of flows with non-trivial vertical structure make use of the of the Eliassen-Palm (E-P) flux formalism described in Chapter 3 [2]. In a cylindrical coordinate system, with increasing radius equivalent to a 'southward' direction, the E-P flux divergence is defined as

$$\begin{aligned} \nabla_m \cdot \mathbf{F} &= r^{-1}\partial_r\left(rF_r\right) + \partial_z F_z \\ &= -r^{-1}\partial_r\left(r\langle\overline{u_r' u_\theta'}\rangle\right) - \partial_z\left((f_0/d_z T_0)\langle\overline{u_r' T'}\rangle\right) \end{aligned} \tag{6.4}$$

Unfortunately, there is an unknown quantity in (6.4) — the vertical temperature gradient $d_z T_0$. As was discussed in Chapter 5, it ultimately proved impossible to acquire any temperature information in the experiments. Therefore, only a crude estimate of $d_z T_0$ based on the mean imposed *horizontal* temperature gradient $\Delta T/(b-a)$ is possible here.

In Figures 6.13 and 6.14, for flat and sloping boundary experiments, the time and zonal averaged E-P flux divergence $\nabla_m \cdot \mathbf{F}$ is plotted as a function of r and z, with the zonal mean profile $\overline{u}_\theta$ superimposed. If the zonal flow is entirely maintained by eddy motion, it is expected that $\overline{u}_\theta$ and $\nabla_m \cdot \mathbf{F}$ will be of the same sign in all regions. Conversely, if eddies are acting to weaken the zonal flow anywhere, the two quantities will be of opposing sign. The z-component of the field, $\partial_z F_z$, involved a double derivative of eddy streamfunction ψ', and hence could only be evaluated at three depth levels. The plots of $\partial_z F_z$ (right hand side of Figures 6.13 and 6.14) must be interpreted with caution, due to the indirect way in which eddy temperature was derived. At best, they give a rough guide only to heat flux effects.

The magnitude of the z-component is considerably greater than that of the r-component in all the examples shown. It is likely, therefore, that heat effects were of greater importance in determining the steady-state zonal flow. Note that this was also found to be the case in some previous studies; for example [49], in which an internally heated flat boundary numerical experiment was performed at lower Taylor numbers.

The qualitative features of the divergence fields are also of interest. In the sloping boundary experiments (Figures 6.13(b) and 6.14(b)), there is clear correlation in places between $\overline{u_\theta}$ and both E-P divergence components, $r^{-1}\partial_r\left(rF_r\right)$ and $\partial_z F_z$. This implies that both heat and momentum eddy fluxes are acting to maintain some of the features of the observed zonal flow field.

In the flat boundary experiments, $\overline{u_\theta}$ is mostly anti-correlated with $r^{-1}\partial_r\left(rF_r\right)$ and $\partial_z F_z$. This implies that eddies are weakening the zonal flow, most likely through a combination of baroclinic and barotropic instability. The only exception is the high rotation rate $\partial_z F_z$ field, which does not clearly relate to either the zonal flow or the eddy momentum flux divergence field. For all high rotation rate flat boundary cases, however, the $\partial_z F_z$ field took the general form seen in Figure 6.14(a). It is possible that the change in $\partial_z F_z$ is linked to the transition to turbulence, in which the vertically sheared zonal flow becomes increasingly barotropic.

As the time-averaged zonal acceleration $\partial_t\langle\overline{u}_\theta\rangle$ is expected to be small, $\nabla_m \cdot \mathbf{F}$ was most likely balanced by other effects in the experiments. In the sloping case, where correlation of $\langle\overline{u}_\theta\rangle$ with the E-P flux implied eddy forcing, Ekman and direct viscous damping were probably the main effects acting to keep the zonal flow roughly constant. In the flat case, as eddies were generally acting to weaken the zonal flow, it was probably deriving most of its energy directly from the thermal forcing. However, it is possible that boundary layer effects were also playing a role in the overall energy budget.

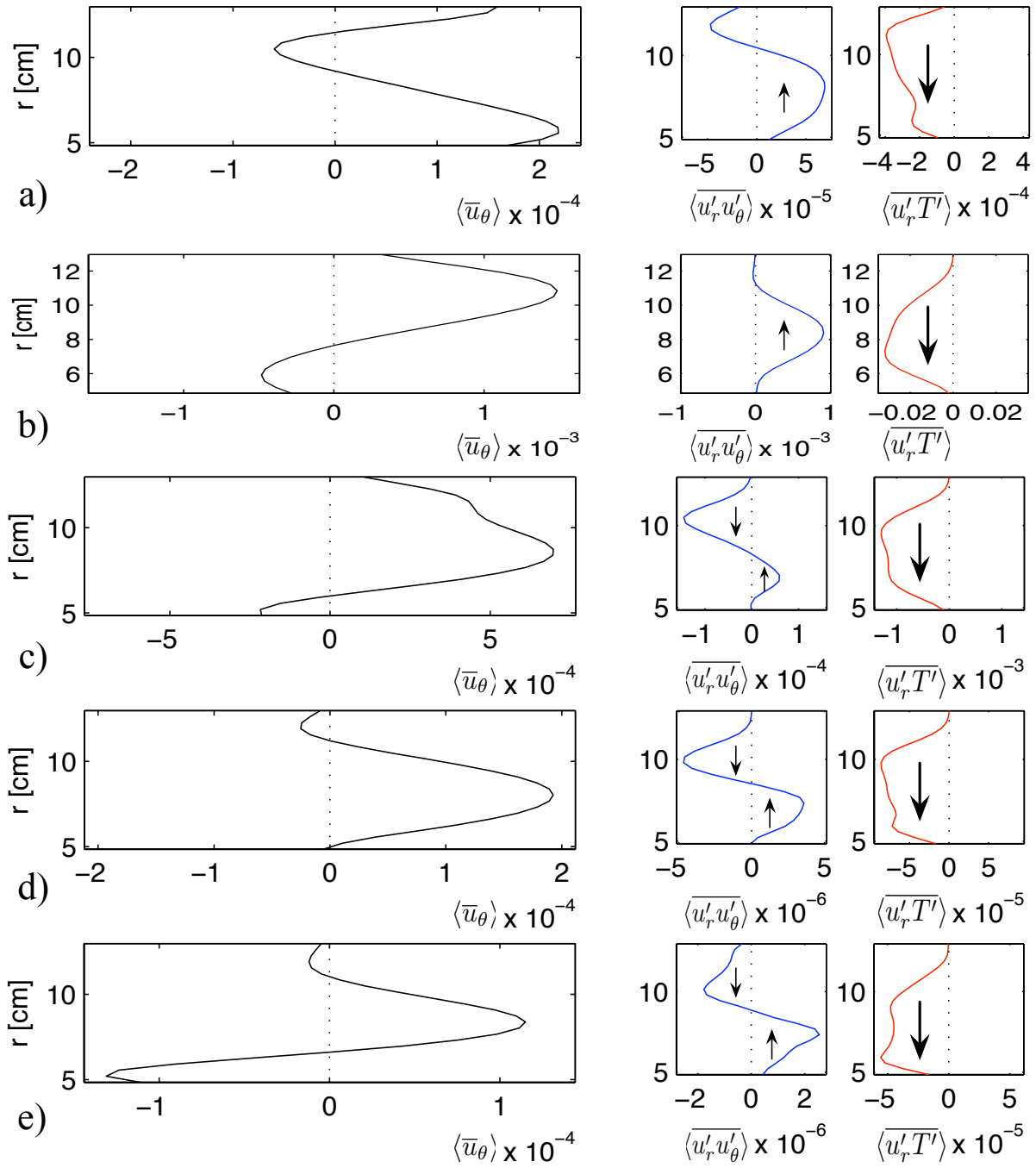

Figure 6.11: Time and zonal averaged zonal velocity $\langle \overline{u}_\theta \rangle$, eddy momentum flux $\langle \overline{u_r' u_\theta'} \rangle$ (center) and approximate eddy heat flux $\langle \overline{u_r' T'} \rangle$ (right) at mid-depth for a selection of experiments with $\Delta T = 2K$. From top to bottom they are: (a) flat boundary, $\Omega = 3.9$ rad s^{-1} (b-d) sloping boundary $\Omega = 0.65$, 1.3 and 3.9 rad s^{-1}, (e) sloping boundary 'fluid B' $\Omega = 3.9$ rad s^{-1}.

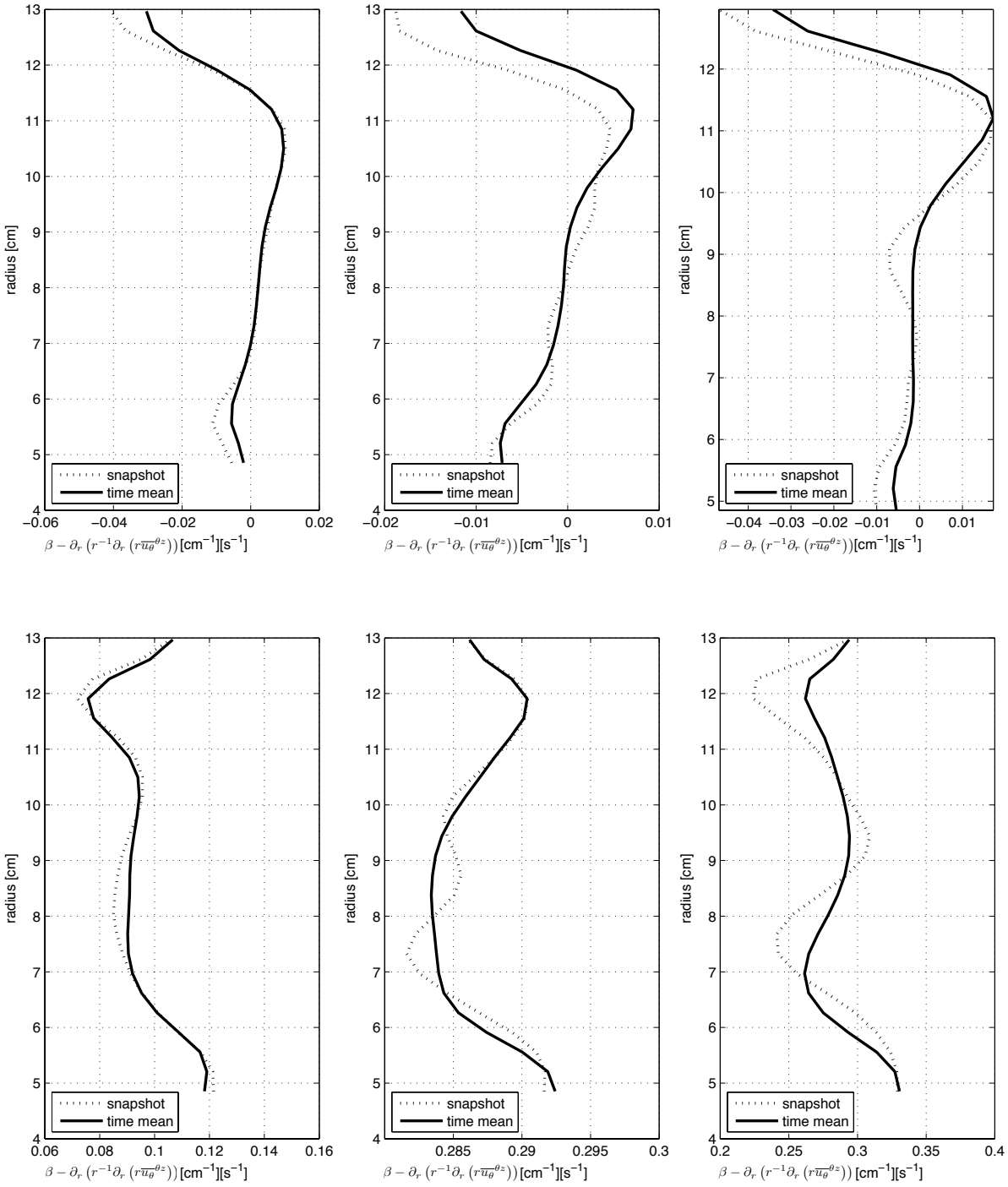

Figure 6.12: Time-averaged and instantaneous barotropic instability parameter $\beta - \partial_r \left(r^{-1}\partial_r \left(r\overline{u_\theta}^{\theta z}\right)\right)$ as a function of r for flat (top) and sloping (bottom) boundary experiments, with $\Delta T = 2K$ and increasing rotation rate $\Omega = 0.65$, 1.3 and 3.9 rad s^{-1} from left to right.

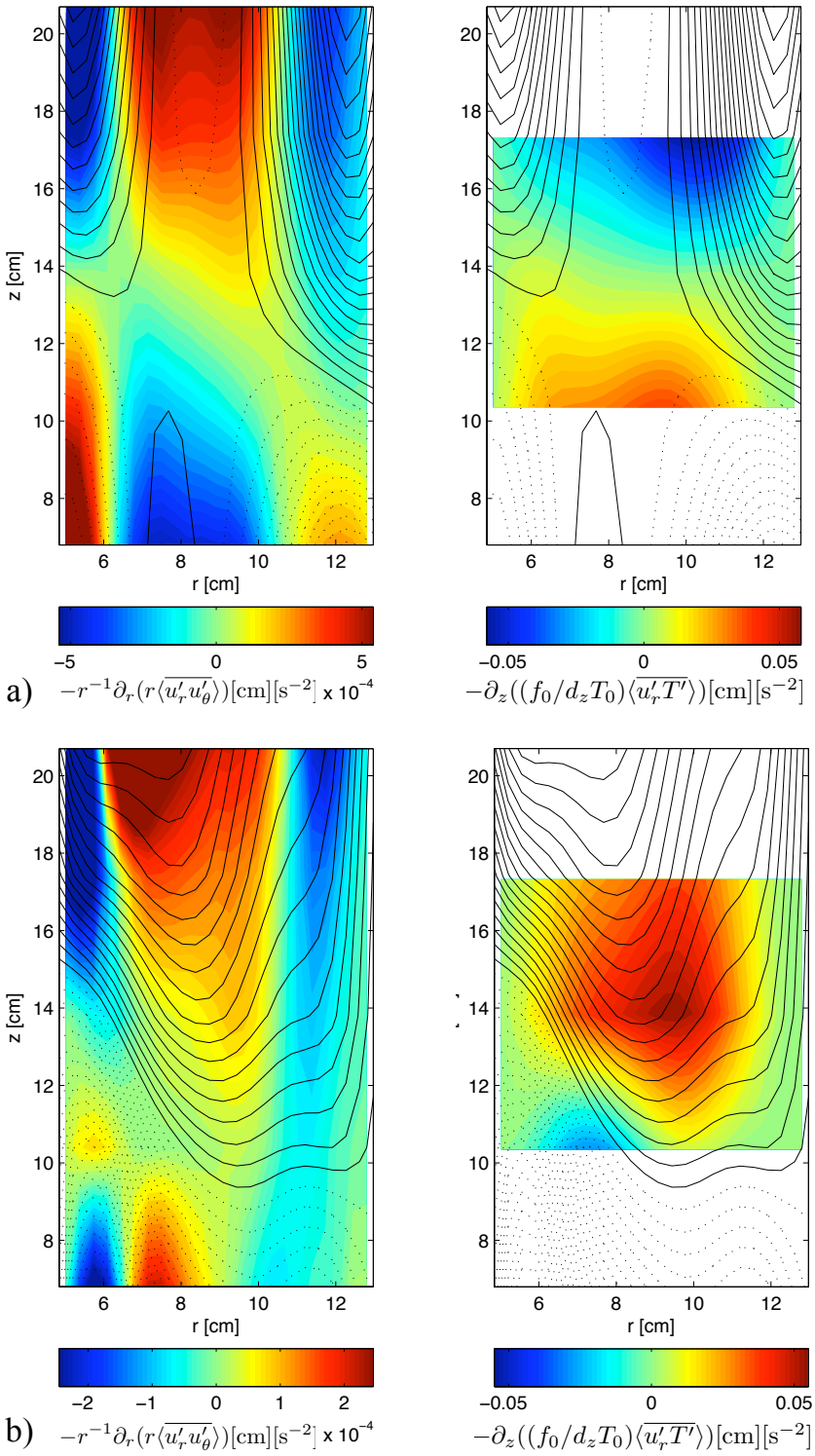

Figure 6.13: Plots of time and zonal averaged E-P flux divergence components $r^{-1}\partial_r\left(rF_r\right)$ (left) and $\partial_z F_z$ (right) for a) flat and b) sloping boundary experiments with temperature difference $\Delta T = 2K$ and rotation rate $\Omega = 1.3$ rad s^{-1}. Time-averaged zonal velocity is overplotted in each case, with solid and dotted lines corresponding to positive and negative values respectively.

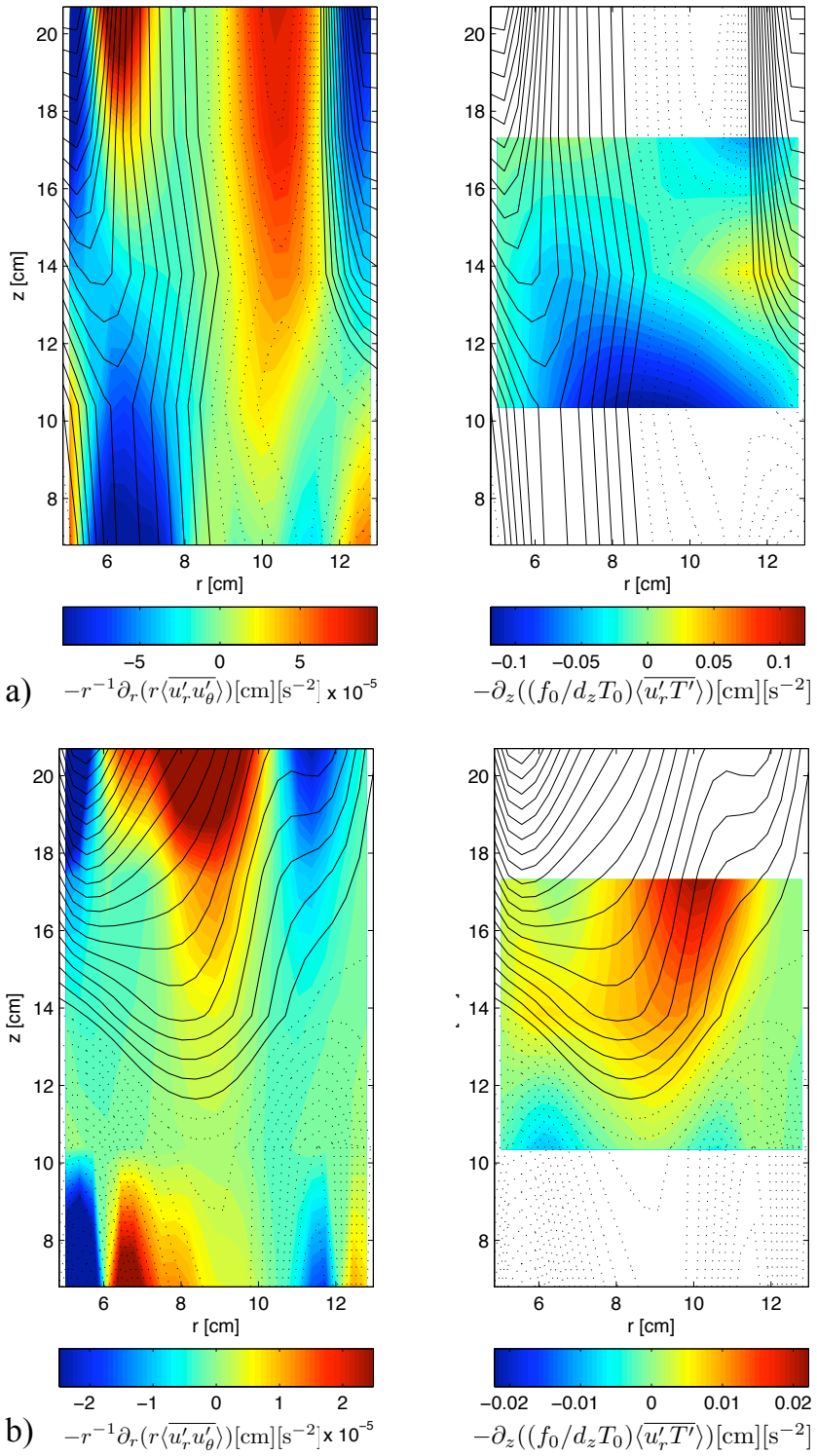

Figure 6.14: Plots of time and zonal averaged E-P flux divergence components $r^{-1}\partial_r\left(rF_r\right)$ (left) and $\partial_z F_z$ (right) for a) flat and b) sloping boundary experiments with temperature difference $\Delta T = 2K$ and rotation rate $\Omega = 3.9$ rad s^{-1}. Time-averaged zonal velocity is overplotted in each case, with solid and dotted lines corresponding to positive and negative values respectively.

6.2 Spectral analysis

In any turbulent or nonlinear flow, the spectral view can provide great insight into the nature of the underlying dynamics. In this section, we examine two-dimensional vertically averaged energy spectra for the flat and sloping boundary experiments.

Spectral analysis of an annular flow is more complicated than the rectangular channel flow case, as the correct eigenmode expansion requires combinations of Fourier and Bessel modes. It can be shown [5] that any single-valued quantity ϕ defined in a 2D annular domain $b \geqslant r \geqslant a$, with boundary conditions of the form $\phi(a,\theta) = \phi(b,\theta) = 0$, can be expanded in terms of the complete, orthogonal basis set

$$\phi(r,\theta) = \sum_{m=-\infty}^{m=+\infty} \sum_{n=1}^{n=\infty} \phi_{mn} K_{mn} = \sum_{m=-\infty}^{m=+\infty} \sum_{n=1}^{n=\infty} \left(\phi^J_{mn} J_m(\gamma_{mn} r) + \phi^Y_{mn} Y_m(\gamma_{mn} r) \right) e^{im\theta} \tag{6.5}$$

where J_m and Y_m are Bessel functions of the first and second kind, and γ_{mn} is a constant that can be determined numerically.

For this analysis, a standard fast Fourier routine was used to perform the azimuthal spectral transform, and a semi-analytical method was used to derive the radial basis modes for the laboratory annulus. Standard numerical linear algebra routines then projected experimental data onto the radial modes. Further details of the method used are given in Appendix B. As the observed flows were in general quite anisotropic, it is of most interest to examine the spectra in two-dimensional wavenumber space. In Figure 6.15 (left column), time-averaged energy spectra are plotted for several experiments as a function of azimuthal and radial wavenumbers m and n.

In the flat boundary case, Figure 6.15(a), kinetic energy decreases rapidly with wavenumber, although there are small peaks of energy at $m, n = (\pm 4, 1)$. In the other plots, which are all from sloping boundary experiments, the concentration of energy in the $(0, 1-3)$ zonal modes is always apparent. However, there are also peaks of energy at higher azimuthal wavenumber (approximately $m = 10$, 15 and 16 for Figures 6.15(b-d)). These peaks are evidently due to the travelling wave structures seen in the mid-level vorticity plots.

The behaviour of the waves can be investigated further by use of a temporal Fourier transform. For convenience, we now use the spatially transformed *vorticity* field ζ_{mn}. The chosen modes are tagged with an asterisk (*) in each case, and the resulting (normalised) power spectra $|\zeta_{mn}(\omega)|^2 / \int |\zeta_{mn}(\omega)|^2 d\omega$ are plotted in Figure 6.15 alongside the 2D spatial energy spectra.

While the flat boundary case has a fairly broadband distribution of frequencies at $(\pm 15, 2)$, centred around $\omega = 0$, the negative frequency peaks for the sloping experiments are clearly apparent. The blue triangles on the plots denote barotropic planetary wave frequencies as given by

$$\omega = \frac{-\beta k}{k^2 + l^2}; \qquad k = \frac{m}{(b+a)/2}, \quad l = \frac{\pi}{b-a} \tag{6.6}$$

and the red bars denote wave drift frequencies as predicted by the linear instability analysis of Hide and Mason [39]. In Hide and Mason's analysis, the frequency of waves in the annulus are given by the real part of the expression

$$\omega_{HM} = \tilde{c}k, \qquad \tilde{c} = \frac{-B \pm \sqrt{B^2 - 4AC}}{2A} \tag{6.7}$$

with

$$\begin{aligned} A &\equiv 1 \\ B &\equiv G\coth G\,(2iF + Q_l + Q_u) \\ C &\equiv -\left(1 + \frac{1}{4}G^2 + F^2 - iF(Q_l - Q_u) - (Q_l + Q_u) + Q_lQ_u - G\coth G(1 - \frac{1}{2}(Q_l + Q_u))\right) \\ F &\equiv \frac{2\nu}{\Omega k d}\frac{G^2}{\Theta} \\ G &\equiv 2\frac{N}{f_0}\sqrt{k^2 + l^2}d \end{aligned} \tag{6.8}$$

where Θ is the Hide number, as defined in (5.2). The buoyancy frequency

$$N^2 = \frac{g\alpha\Delta T_z}{d}, \tag{6.9}$$

which is assumed constant in the analysis, may be related to the horizontal temperature difference ΔT using $\Delta T_z = \chi\Delta T$, where $\chi \leq 1$ is some constant factor. Of course, as no internal temperature measurement was possible, the value of χ is not known. Therefore in Figure 6.15, the analytical prediction (6.7) is plotted for the range of values $0.2 \leq \chi \leq 1$, in order to give a rough guide to the true analytical prediction.

It may be recalled from Chapter 2 that the analogy between the β-effect and sloping boundaries in a heated annulus is qualitative only. Thus, as might be expected, the instability analysis gives a better prediction than the naive barotropic one in general. Indeed, in all plots except Figure 6.15(b), the barotropic prediction is too large to be contained within the horizontal axis of the plots. However, the Hide-Mason prediction still tends to slightly overestimate wave frequency, even with the the vertical temperature gradient uncertainty taken into account. Note that both predictions neglect the effects of annulus curvature. It is not known to what extent this affects their accuracy, although errors due to other approximations (such as the neglect of direct viscous damping and Ekman layer heat transport) may well be more significant.

At high rotation rates, the peaks become broader and more structured (Figures 6.15(d-e)), quite possibly due to an increase in nonlinear mode-mode coupling. Interestingly, qualitatively similar peak broadening and shifting due to nonlinear effects have been observed by Sukoriansky et al. [60], in a numerical study of purely two-dimensional planetary wave turbulence on the surface of a sphere. In the next section, we examine the interaction between modes in more detail via a spectral transfer calculation.

6.2.1 Spectral energy transfer

As a final investigation into the dynamics of the flow, the transfer of kinetic energy in spectral space was calculated. This can be seen as a complement to the Reynolds stress analysis carried out in Section 6.1.1, as the focus will again be the transfer of energy between eddies and zonal flow. However, vertically varying effects are ignored in this section. Instead, the emphasis is now on determining the extent to which barotropic energy exchange between modes is *local* in spectral space.

To keep things simple, only spectral transfer in the azimuthal direction will be examined. This removes the need to calculate triad coefficients involving Bessel functions, which simplifies the algebra considerably.

Given a quasigeostrophic interior flow, the quantity

$$\mathcal{P}_m = -\sum_{m=p+q} \langle T_{mpq} \rangle \tag{6.10}$$

is the time and radius averaged rate of energy transfer into azimuthal mode m due to all barotropic nonlinear interactions. In a steady-state system, it must be balanced by nonconservative effects such as Ekman damping, or by nonlinear interactions of another type, e.g., mixed barotropic-baroclinic. The result (6.10) is derived in full in Appendix C, where the explicit form for the spectral transfer term T_{mpq} is also given.

The sum on the right hand side of (6.10) is the familiar one over all triads satisfying $m = p + q$. It is too complex and time-consuming to study the set of all possible triad interactions, so we choose to examine (6.10) for certain restricted subsets of wavenumbers. In Figures 6.16 and 6.17, $\mathcal{P}_m$ is calculated for the domain $-15 < m < 15$, but with p and q restricted to the wavenumbers marked in grey for each plot. In short, the plots show us the energy input to the entire range of wavenumbers between -15 and 15 *from* the wavenumbers marked in grey in each case.

Due to the importance of the spectral transfer calculation in determining the nature of the jet-eddy interaction, it was decided to extend the analysis to a large number of datasets. The plots in Figure 6.16 are from the same experiments as in Figure 6.15, but those in Figure 6.17 are from different flat and sloping boundary experiments at high rotation rate. The plots appear complicated at first sight, but some general patterns can quickly be determined. In all cases, the transfer of energy is predominately towards smaller azimuthal wavenumber. This is expected based on the theoretical arguments of Chapter 2.

In the flat boundary cases, energy transfer is to a fairly broad range of low wavenumbers, but it is not exactly as expected by inverse cascade arguments. In detail, the picture is quite complex, as significant energy exchange occurs between the lowest wavenumbers. Also, the highest wavenumbers are transferring energy *directly* to the lowest — although the magnitude of the transfer is much less than that for intermediate and low wavenumbers.

The sloping boundary experiments exhibit qualitatively different behaviour. In every case studied, energy transfer to the zonal mode is dominant. For the low rotation rate $\Omega = 0.65$ and 1.3 rad s^{-1} experiments (Figures 6.16(b) and (c)), the region of greatest energy input to the zonal mode also corresponds to the peak wavenumber in the energy spectra (Figure 6.15). At higher rotation rates, the picture becomes a little more complicated. While the $\Delta T = 2K$ experiments (Figures 6.16(d) and (e)) show a decrease in energy input from the intermediate to high wavenumbers, in the $\Delta T = 4K$ experiments (Figures 6.17(d) and (e)) the energy input is the same or greater. The difference implies a possibly greater role for intermediate wavenumbers when forcing is lower. There is still little evidence of strong eddy-eddy interaction, however, even in the two low viscosity fluid B cases.

It is of course possible that significant local energy exchange is occurring in the barotropic-baroclinic interactions, which we have not investigated here. This seems unlikely, however, based on the two-layer argument outlined in Section 2.2. Recall that energy exchange between barotropic and (1^{st}) baroclinic modes is most effective at the deformation wavenumber k_D. At lower wavenumbers, it was argued that interactions between barotropic modes would dominate. As significant barotropic interaction between low wavenumbers was not observed in the sloping boundary experiments, it therefore seems likely that energy input to the zonal flow from baroclinic eddy effects was at least as non-local as in the barotropic case.

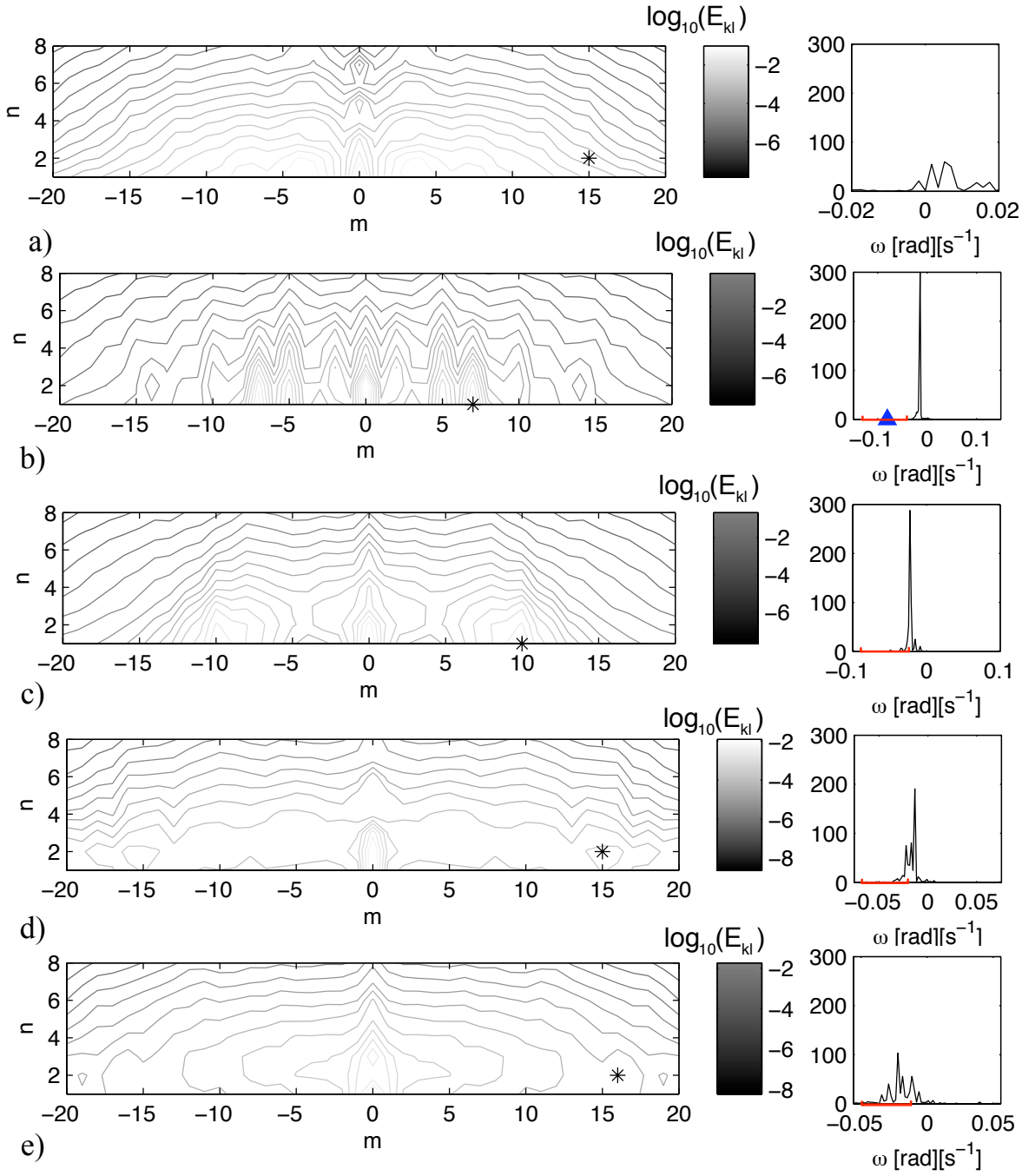

Figure 6.15: Time-averaged two-dimensional contour plots of barotropic kinetic energy in m, n spectral space for the same experiments as in Figure 6.11. Also plotted are temporal Fourier power spectra of spectral vorticity ζ_{mn} for modes marked by an asterisk on the contour plots.

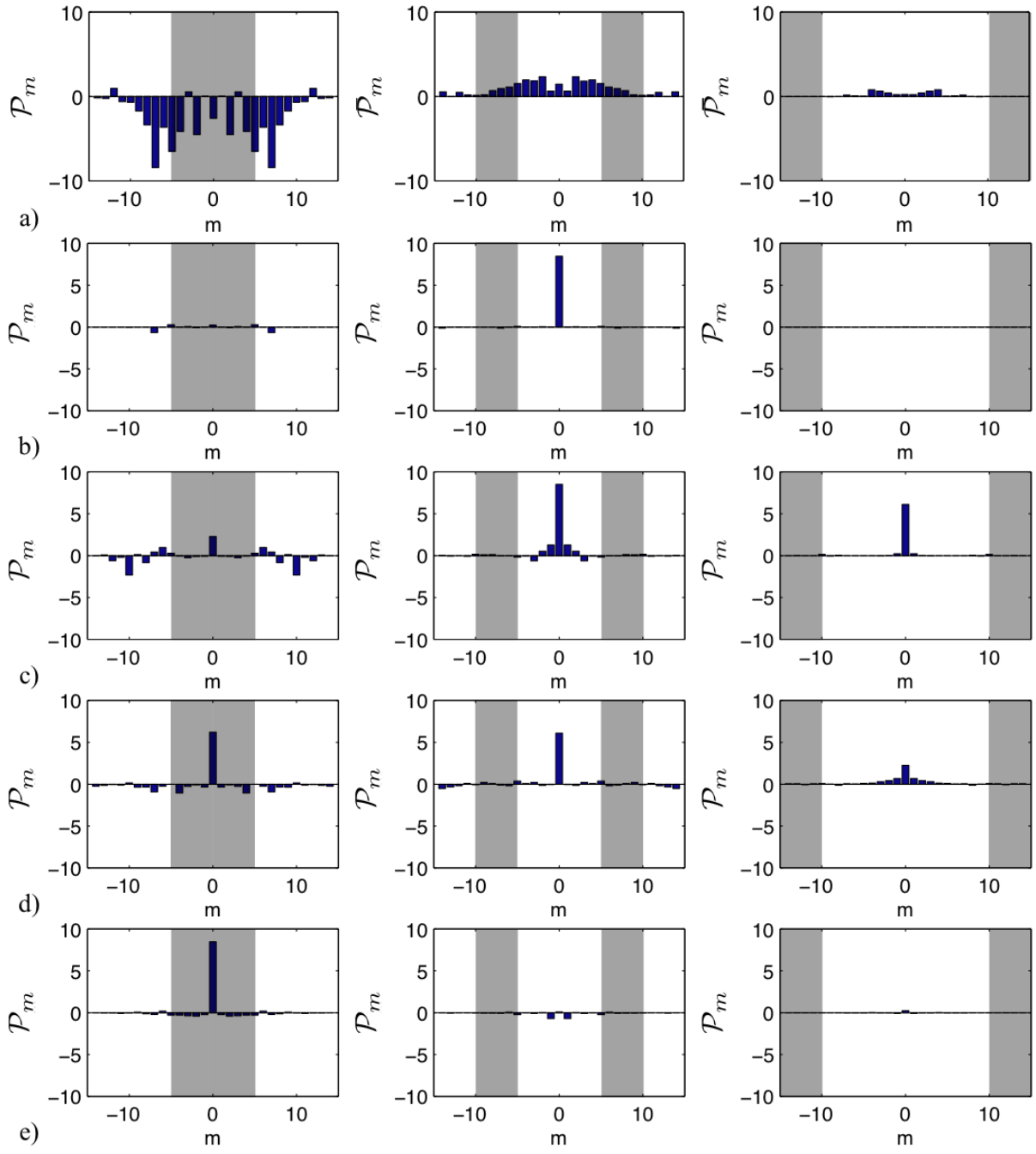

Figure 6.16: Normalised azimuthal spectral energy transfer $\mathcal{P}_m$ as a function of radius and azimuthal wavenumber for the same experiments as in Figure 6.11. For each plot, the areas marked in grey are those from which the wavenumbers p, q are selected.

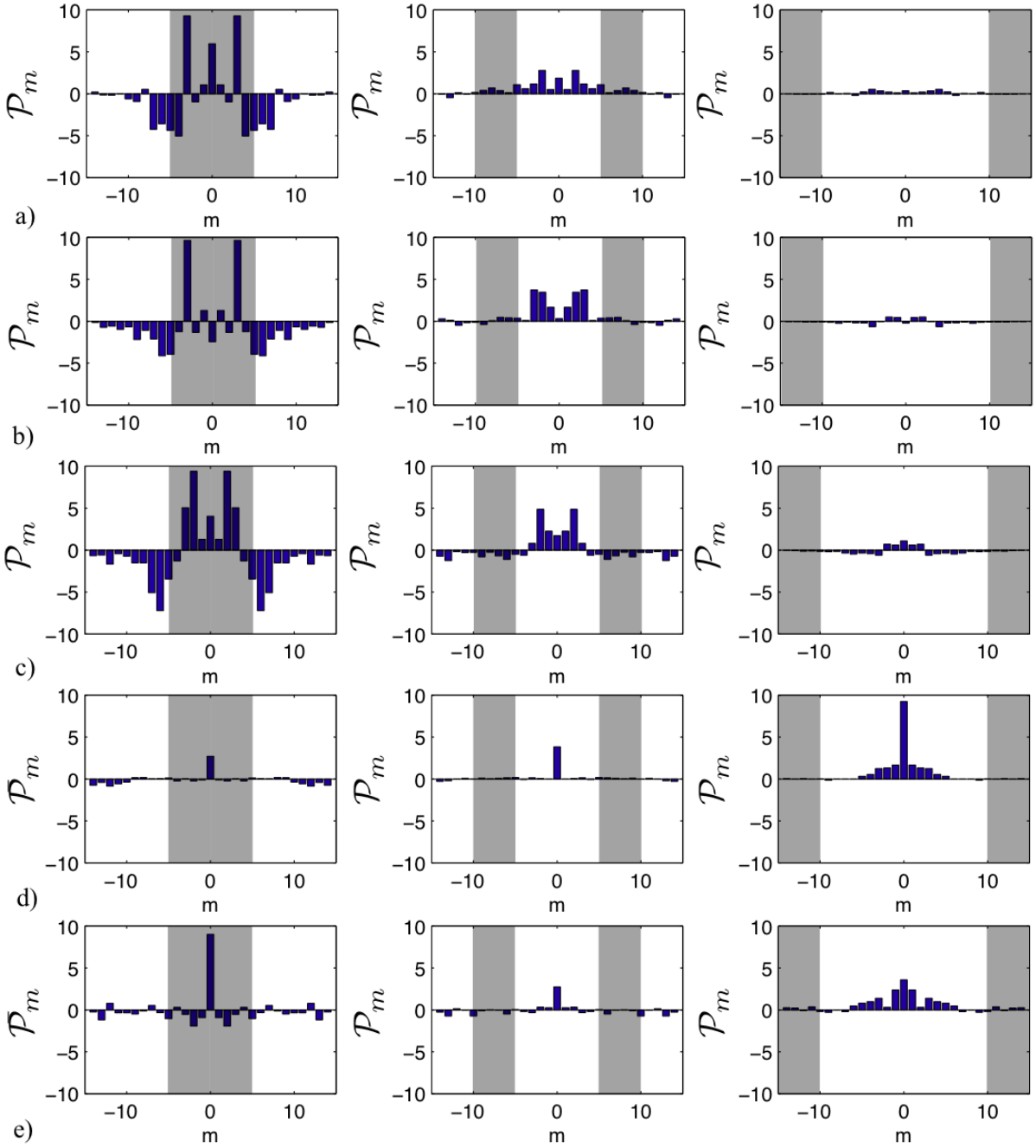

Figure 6.17: Normalised azimuthal spectral energy transfer $\mathcal{P}_m$ as a function of radius and azimuthal wavenumber for a selection of experiments at high rotation rate $\Omega = 3.9$ rad s^{-1}. From top to bottom they are a) flat boundary, fluid B, $\Delta T = 2K$, b) flat boundary, fluid A, $\Delta T = 4K$, c) flat boundary, fluid B, $\Delta T = 4K$, d) sloping boundary, fluid A, $\Delta T = 4K$ and e) sloping boundary, fluid B, $\Delta T = 4K$. For each plot, the areas marked in grey are those from which the wavenumbers p, q are selected.

6.3 Discussion

This section only provides a brief review of the results of this chapter. For a more general discussion of the experimental results in the context of the entire thesis, turn to Chapter 9.

To summarise: the behaviour of the differentially heated rotating annulus was investigated at high Taylor and low Hide numbers. When the top and bottom boundaries are flat, it was found, as in previous studies, that the locally smooth flow observed at relatively low Taylor numbers evolves into a rapidly varying turbulent one as the rotation rate is increased.

When sloping top and bottom boundaries are present, multiple jets formed at mid-depth in the fluid. A Reynolds stress analysis showed that eddies were directly feeding momentum into the jets. A crude E-P flux analysis indicated that eddy *heat* flux divergences may have had an even greater role in forcing the jets, although the way in which eddy temperature fields were derived means that the results cannot be regarded as conclusive. Spectral analysis of the barotropic mode also showed that eddy energy was concentrated around a definite peak wavenumber and frequency, even in the multiple jet formation regime.

Perhaps the single most important result obtained from the experiment, however, is that described at the end of Section 6.2. Through a spectral transfer calculation, it was shown that the eddies were exchanging energy directly and *nonlocally* in spectral space with the zonal modes. Hence turbulent cascade theory, which postulates that energy exchange between local wavenumbers will dominate, appears to not be applicable, particularly in the case of the sloping boundary results.

This result also hints that the wave-mean flow ideas of Chapters 3 and 4 are an appropriate base from which to construct a reduced theoretical or numerical model of the experiment. In the next chapter, this idea is investigated further.

Chapter 7

Ocean basin experiments

There are many differences between oceanic and atmospheric fluid flow on Earth. In terms of the jet formation problem, one of the most obvious differences is the fact that all ocean flows are ultimately bounded by coastlines[1] — there is no 'global ocean'. Although it is generally thought that there is no fundamental constraint against jet formation in ocean basins, no scientific study to date has directly addressed the effects of adding boundaries to a system in which the phenomenon is already known to occur. Rotating annulus experiments with a blocking wall present *have* been conducted before in several configurations, most comprehensively by Rayer et al. [48]. However, none of these investigations were carried out in the highly nonlinear jet formation regime.

During the course of this DPhil, therefore, it was decided that inclusion of a vertical 'ocean wall' in the existing laboratory setup would make a most interesting experiment, as it would allow the hypothesis that vertical boundaries do not inhibit jet formation to be tested directly. In this chapter, the results of these experiments are presented and analysed. This chapter is based on a paper [71] that is in preparation for publication.

7.1 Experimental setup

A schematic of the new experimental setup is given in Figure 7.1. It is basically identical to that described in Chapter 5, with the single difference that a vertical wall is included at $\theta = \pi/2$ in the annulus. The wall was constructed from a 1 cm thick sheet of perspex, which can be regarded as thermally insulating to a good approximation.

As the development of jets in an ocean basin was of most interest to the investigation, all simulations were performed with the sloping top and bottom boundaries present in the annulus. Six experiments were performed in total, with varying rotation rates of $\Omega = 1.3$ rad s^{-1} and 3.9 rad s^{-1} and temperature differences of $\Delta T = 2$, 4 and 6 K. The lower viscosity fluid B was used in all cases. As in the previous sections, all experiments were run for two hours, with data collection occurring in the second hour. In the analysis, all time averages were performed over the entire data collection period.

[1] Exception to the rule: the Antarctic circumpolar current in the Southern Ocean.

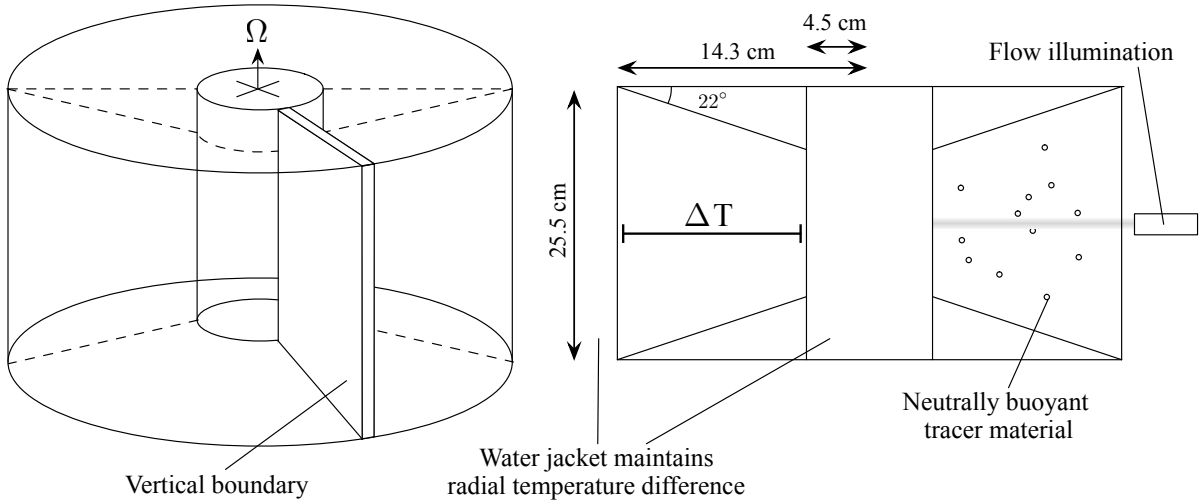

Figure 7.1: Schematic of the modified 'ocean wall' experimental setup.

7.2 Results

Mid-level streak images of the two experiments at $\Delta T = 4K$ are displayed in Figure 7.2. As can be seen, the flow is zonally asymmetric in both cases, with a strong 'western' boundary current clearly visible on the left hand side of the boundary. This current exists due to a geostrophic effect caused by the radial temperature difference along the ocean wall (see Rayer et al. [48] for details). As is visible from the streak images, it is the western edge of a long gyre that extends azimuthally almost to the other side of the wall, decreasing in strength as it goes. In both images, eddy motion is visible; however in the lower rotation rate experiment (left) it is mainly confined to a region close to the inner cylinder. In the high rotation rate experiment (right), eddies are visible throughout most of the domain, and in places, the inner half of the gyre appears to have split into multiple jets.

The extent to which zonation is occurring is made clearer by looking at mid-level, time-averaged zonal velocity $\langle u_\theta \rangle$. In Figure 7.3, this quantity is plotted for all six experiments. In Figure 7.4, $\langle u_\theta \rangle$ is also plotted for high rotation rate flat and sloping boundary experiments without a vertical boundary present, to allow direct comparison with these cases. As can be seen, at low rotation rates and high temperature differences, the velocity only changes sign once across the channel in the vertical boundary experiments. At high rotation rate, multiple jets can be clearly observed, particularly in the $\Delta T = 4K$ experiment.

Although Figure 7.3 shows zonal velocities averaged over a 1-hour interval, coherent multiples jets were observed in fields averaged over intervals as short as a few minutes. This suggests that the fluctuation timescales in these experiments were relatively rapid. As can be seen, the jets in the $\Delta T = 4$K, $\Omega = 3.9$ rad s^{-1} experiment also have characteristic length scales (approximately $\frac{1}{2}$ to $\frac{1}{3}$ of the circumference). The reason for their decay with azimuth is not known, although it is most likely related to the varying strength of the 'background' gyre.

In Figure 7.5, a vertical slice of time-averaged zonal velocity $\langle u_\theta \rangle$ is plotted for all six experiments. The slice was taken opposite to the vertical boundary, at $\theta = 3\pi/2$. As can be seen, the flow is

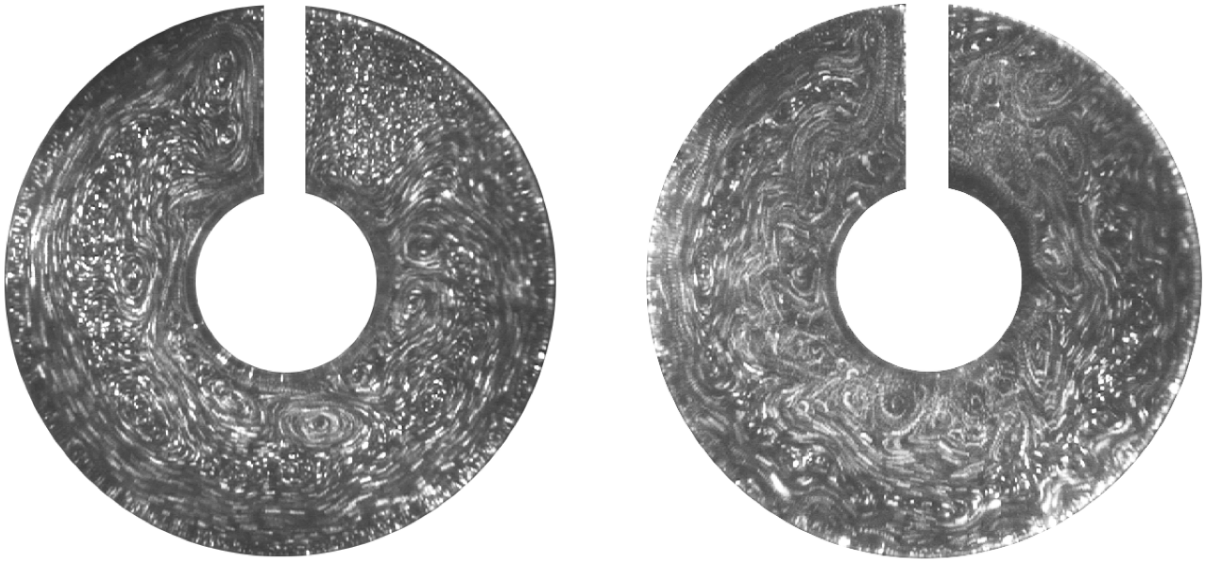

Figure 7.2: Streak image comparison of the mid-depth flow with temperature difference $\Delta T = 4K$, at low rotation rate $\Omega = 1.3$ rad s^{-1} (left) and high rotation rate $\Omega = 3.9$ rad s^{-1} (right) in the ocean wall experiments.

remarkably barotropic; more so, in fact, than in the cases where no sloping boundary or vertical barrier was present. As in Figure 7.3, the transition to multiple jets is most apparent in the high rotation rate $\Delta T = 4K$ experiment.

Because the basic mean flow in these experiments has a strong radial component, zonal averages are less obviously useful for analysis than they were in the previous experiments. It is of more interest to compare the relative strengths of the *time-averaged* flow, and the fluctuations from that average. In Figure 7.6, mid-level total, time-average and fluctuation kinetic energy are plotted for the two $\Delta T = 4K$ experiments.

As can be seen, time-averaged is greater than fluctuation kinetic energy by about an order of magnitude at low rotation rate, but only by a factor of about three at the high rotation rate. The spatial structure of the mean energy plots is extremely revealing. At low rotation rates, most energy is concentrated around the inner and outer boundaries and the western wall of the annulus. At high rotation rates, the western boundary current is still present, but significant mean energy can also be seen in the interior. Fluctuation energy is also more widely distributed in the high rotation rate case, although it is greatest near the inner cylinder for both experiments.

7.2.1 Reynolds stress analysis

It is also of interest to examine eddy momentum fluxes for these experiments. Due to the difficulty involved in numerically deriving a geostrophic streamfunction in the azimuthally bounded annular domain, discussion of eddy heat flux is omitted here.

In Figure 7.7, time-averaged eddy momentum flux divergences are plotted beside the time-averaged zonal flow for the two $\Delta T = 4K$ experiments. In the low rotation rate experiment, where eddy motion was comparatively weaker, strong flux divergence is confined to a region close to the inner

cylinder. The momentum flux is acting to strengthen the negative inner jet close to the cylinder, but weaken it in the centre of the channel.

At high rotation rates, the eddies are spread throughout the domain, and the flux divergence field appears more complex. Nonetheless, there are clear areas of correlation with the zonal flow, particularly in the upper right section of the plot. Ultimately, it is most likely that the observed steady-state flow profile is maintained partially by eddy action (via both momentum and heat flux divergences), and partially by the geostrophic effects that give rise to the gyre at low rotation rates.

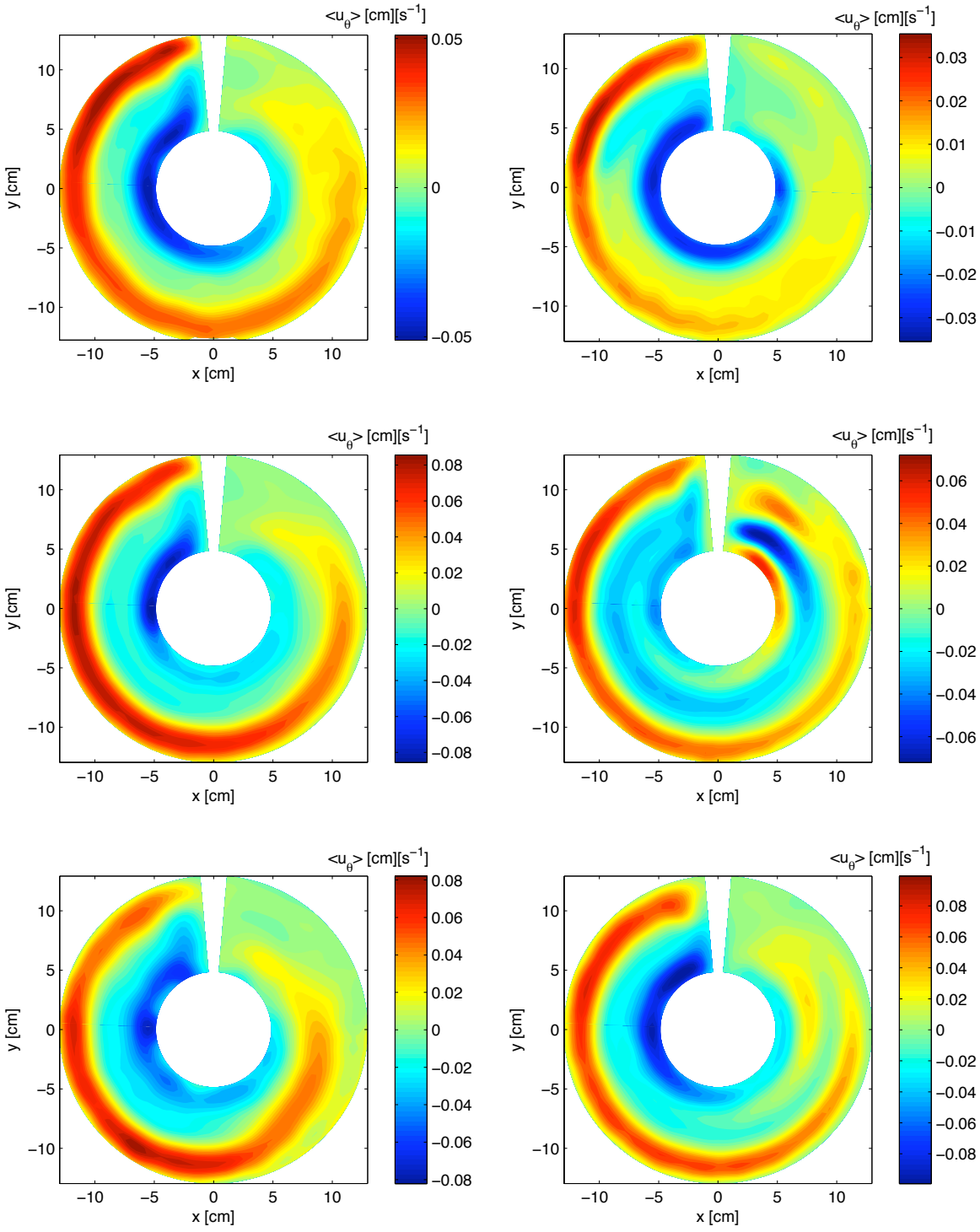

Figure 7.3: Mid-depth time-averaged zonal velocity $\langle u_\theta \rangle$ at low rotation rate $\Omega = 1.3$ rad s^{-1} (left) and high rotation rate $\Omega = 3.9$ rad s^{-1} (right) in the ocean wall experiments, with temperature difference $\Delta T = 2K$ (top), $\Delta T = 4K$ (centre) and $\Delta T = 6K$ (bottom).

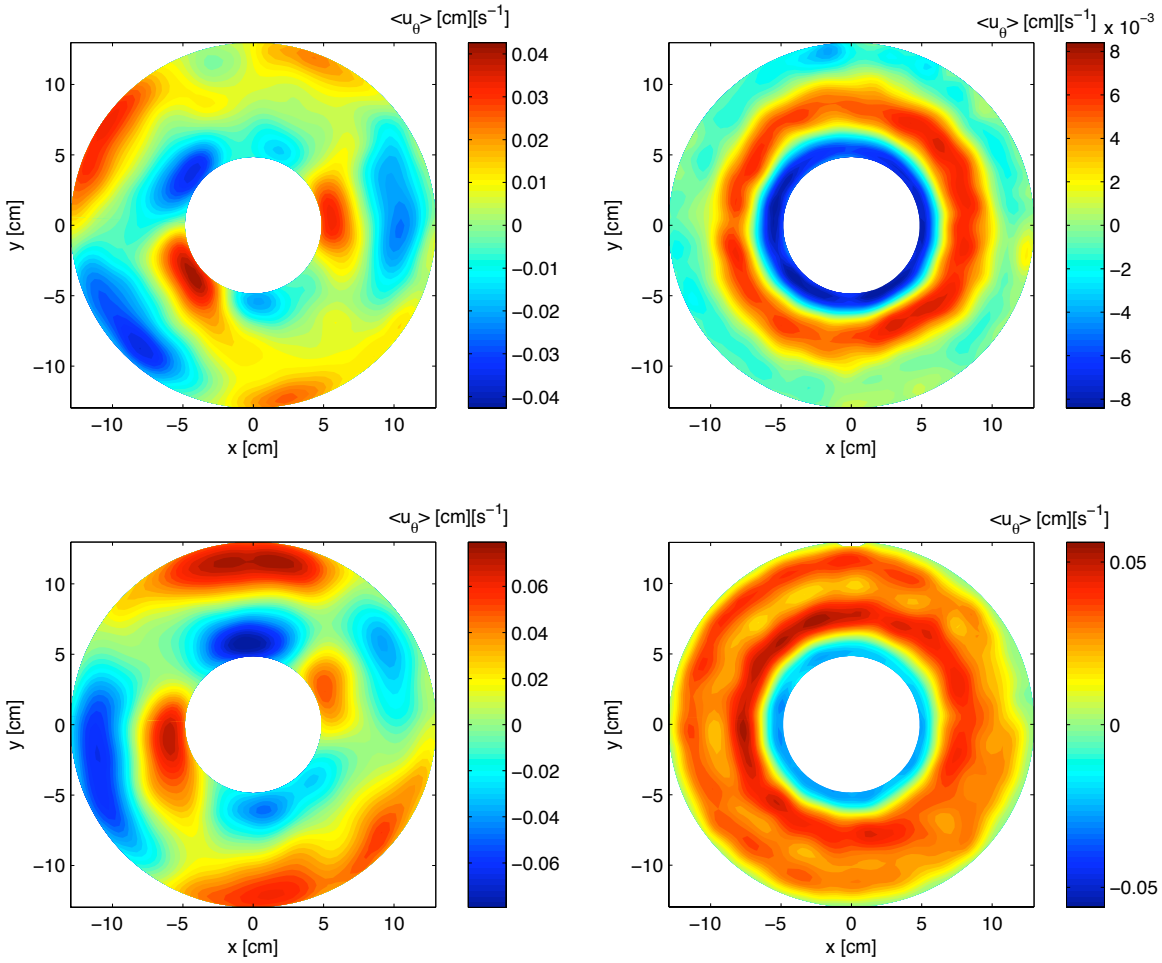

Figure 7.4: Mid-depth time-averaged zonal velocity $\langle u_\theta \rangle$ at high rotation rate $\Omega = 3.9$ rad s^{-1} in the flat (left) and sloping (right) boundary experiments described in Chapter 6, with temperature difference $\Delta T = 2K$ (top), $\Delta T = 4K$ (bottom). Fluid B was the working fluid in all cases. The strong azimuthal variation in the flat boundary cases was due to the large-scale coherent structures described in Chapter 6, which did not precess noticeably over the duration of the analysis.

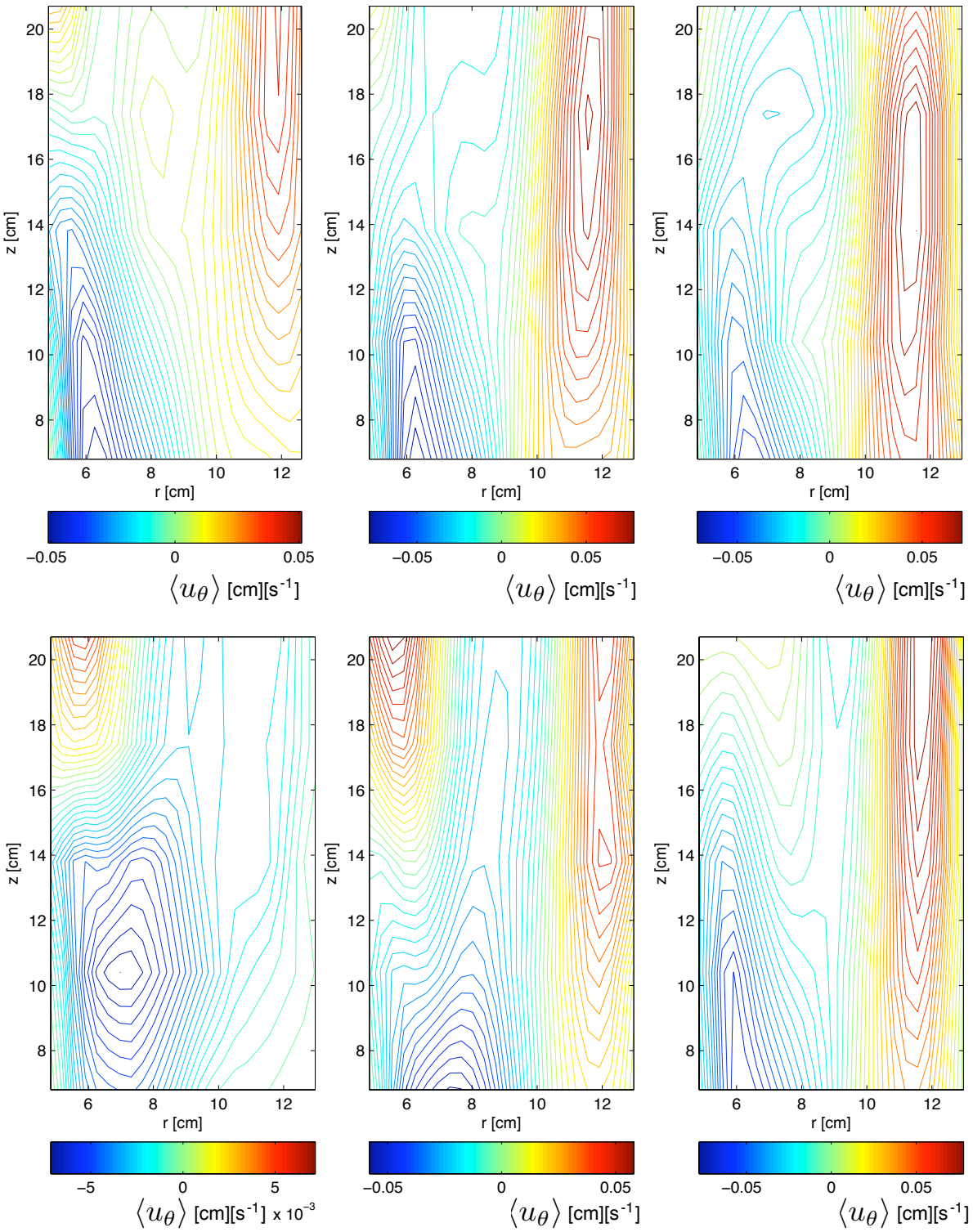

Figure 7.5: Time-averaged zonal velocity at $\theta = 3\pi/2$ as a function of r and z for $\Delta T = 2K$ (left), $\Delta T = 4K$ (center) and $\Delta T = 6K$ (right) ocean wall experiments, with rotation rate $\Omega = 1.3$ (top) and 3.9 rad s^{-1} (bottom).

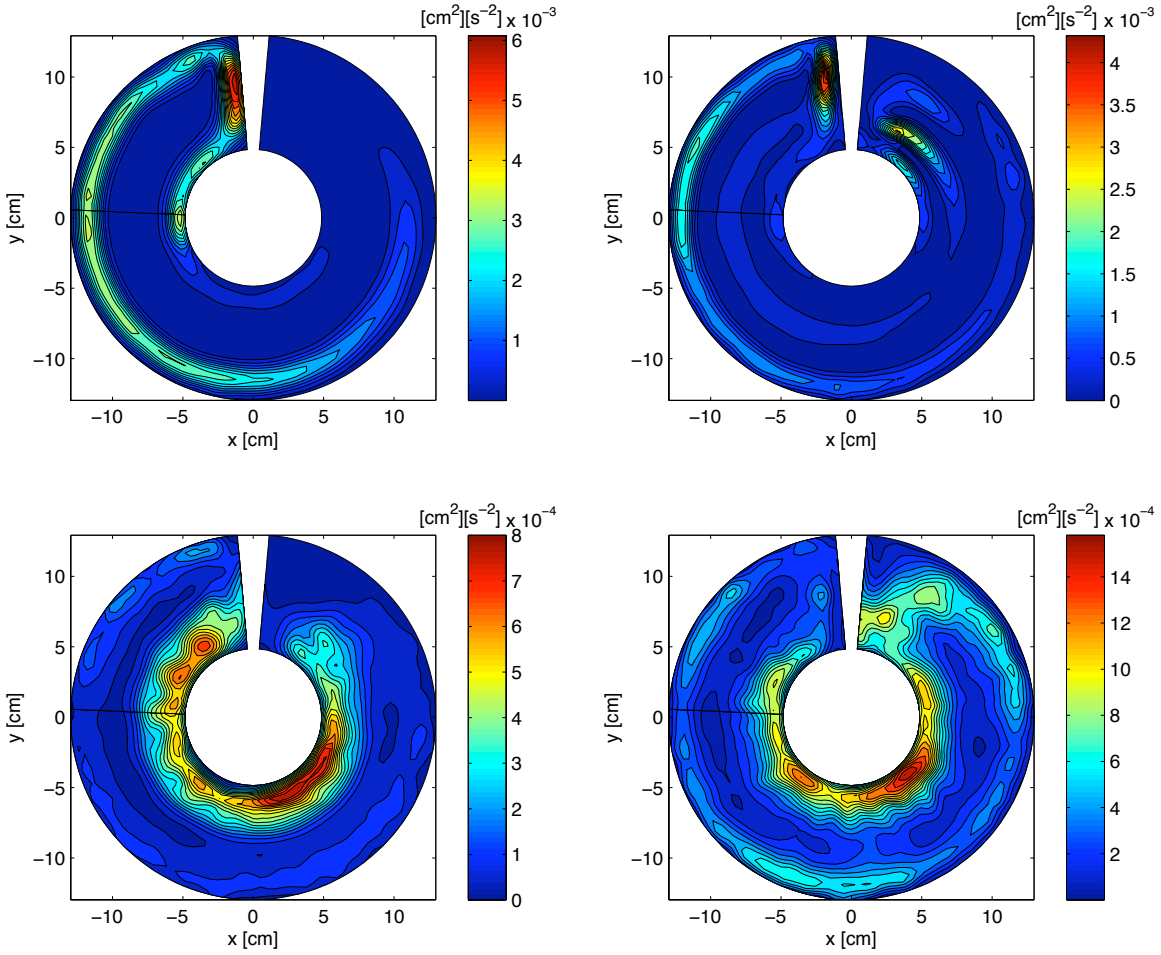

Figure 7.6: Time average (top) and fluctuation (bottom) kinetic energy at mid-depth for $\Delta T = 4$K ocean wall experiments with rotation rate $\Omega = 1.3$ rad s^{-1} (left) and $\Omega = 3.9$ rad s^{-1} (right).

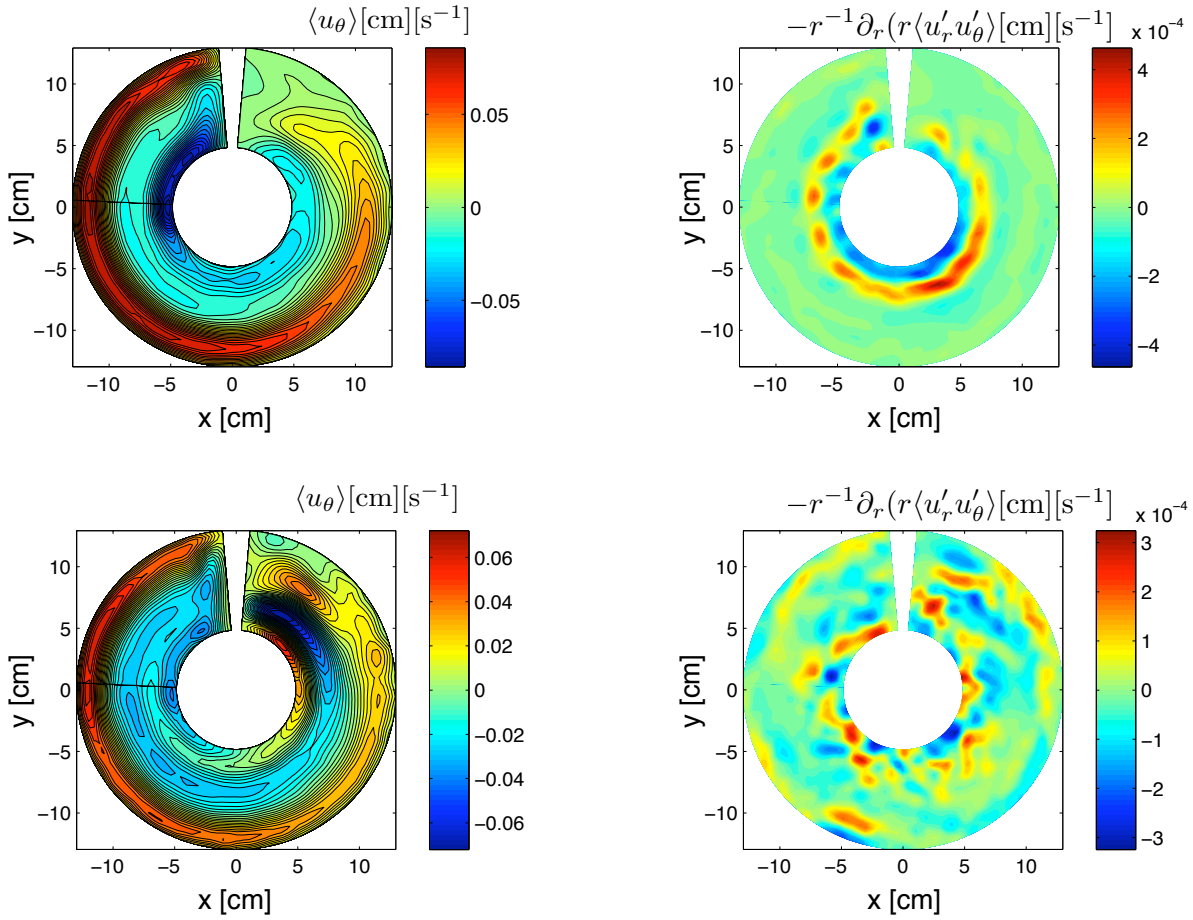

Figure 7.7: Time-averaged zonal velocity $\langle u_\theta \rangle$ (left) and eddy momentum flux divergence $-r^{-1}\partial_r(r\langle u_r' u_\theta' \rangle)$ (right) for ocean wall experiments with temperature difference $\Delta T = 2K$ and rotation rate $\Omega = 1.3$ rad s^{-1} (top) and $\Omega = 3.9$ rad s^{-1} (bottom).

7.3 Discussion

The results of this chapter demonstrate that quasi-barotropic jet formation can occur even if a vertical boundary is present in the annulus. It was found that at high Taylor numbers, the gyre and western boundary current observed by Rayer et al. [48] becomes turbulent and splits into a series of multiple zonal jets at mid-depth. Clearly, these results may have interesting implications for the oceanic jet formation problem.

It is interesting to compare the vertical structure of the jets observed in this chapter with those of Chapter 6. As has been noted, the former were found to be significantly more barotropic. The reason for this is unknown, although in Rayer et al. [48], it was suggested that the low rotation rate gyre was mainly height-independent in the fluid interior (the so-called 'ζ-circulation'), and that it could be described by an essentially linear argument.

The eddy momentum flux results are also of interest, although the analysis is made more difficult by the lack of zonal symmetry of the observed flow. The time-averaged eddy momentum flux divergence fields at low rotation rates clearly indicate that initially, eddies act to split the inner part of the gyre into two jets. At higher rotation rates, the flux divergence field is less coherent, although some correlation with the zonal flow can be observed, especially in the 'eastern' part of basin (top right). It would be of much interest in future work to analyse the relative importance of eddy momentum and heat fluxes.

Chapter 8

Reduced model of the experiment

In this chapter, the numerical code of Chapter 4 is generalised to the two-layer equations, in order to create a simple reduced model of the laboratory experiment. In the first section, the model setup is described. Next, the results of the model for a linear instability test case are compared with theory, and it is verified that the model conserves energy when forcing and damping are zero. Realistic forcing and damping mechanisms are then included, and the model is run in a bounded cylindrical coordinate system with the same dimensions as the experimental annulus. As will be seen, the qualitative steady-state jet structure predicted by the model is remarkably close to that observed in the sloping boundary experiments at high rotation rates.

8.1 Model setup

The numerical model presented in Chapter 4 is incapable of describing the flow in the annulus, even qualitatively, because it lacks vertical structure and hence cannot capture baroclinic instability. As discussed in Chapter 2, the simplest possible way to describe baroclinic processes in reduced form is via the two-layer approximation.

Here, therefore, equations (2.27)-(2.28) are used as a starting point. Of course, it is naive to expect that all details of the experimental system can be captured with a purely quasigeostrophic model. This is not the aim of the chapter. Instead, we wish to see if the *general* features of the observed flow can be captured with as simplified a set of equations as possible.

The main approximation is that made in Chapter 3: all wave-wave interaction is neglected. Only interaction between the zonal mean flow and a single azimuthal mode is to be considered. The spectral transfer analysis of Section 6.2 has suggested (but not proved) that this approximation may well be a reasonable one. In one sense, therefore, this entire chapter can be regarded as a test of the following hypothesis:

The structure of the jets in the experimental flow is primarily determined by wave-mean flow interactions. Wave-wave interactions are of secondary importance only.

Of course, the restriction to a single azimuthal mode brings an additional, large approximation to the model. Referring to the spectral energy graphs of Chapter 6, for example, it is clear that significant amounts of energy are distributed among different wavenumbers even for the low rotation

rate, non-turbulent experiments. At the end of the chapter, we discuss the effect this second approximation has on the model dynamics.

When the standard decomposition into zonal mean and eddy fields is made, the modal two-layer equations (2.27)-(2.28) (with Ekman damping now included) become[1]

$$\partial_t \overline{q} + \frac{1}{2}\left(\overline{J[\psi_1', q_1']} + \overline{J[\psi_2', q_2']}\right) = -\kappa \overline{q} \tag{8.1}$$

$$\partial_t \overline{\sigma} + \frac{1}{2}\left(\overline{J[\psi_1', q_1']} - \overline{J[\psi_2', q_2']}\right) = -\kappa \overline{\sigma} \tag{8.2}$$

for the mean flow. Following the procedure described in Chapter 3, this can be rewritten as

$$\partial_t \overline{q} + \frac{1}{2}\partial_y\left(\overline{v_1' q_1'} + \overline{v_2' q_2'}\right) = -\kappa \overline{q} \tag{8.3}$$

$$\partial_t \overline{\sigma} + \frac{1}{2}\partial_y\left(\overline{v_1' q_1'} - \overline{v_2' q_2'}\right) = -\kappa \overline{\sigma}. \tag{8.4}$$

Note that for simplicity, we use the channel coordinate system of Chapter 3 throughout this chapter. Given the many other approximations used in the model, it was decided that the error introduced by neglecting annulus curvature would not be significant.

Given the relationship between potential vorticity, streamfunction and velocity, the above equations can be rewritten in terms of the barotropic ($\overline{u}_t$) and baroclinic ($\overline{u}_c$) zonal flow only[2]

$$\partial_t \overline{u}_t = \frac{1}{2}\left(\overline{v_1' q_1'} + \overline{v_2' q_2'}\right) - \kappa \overline{u}_t \tag{8.5}$$

$$\partial_t \overline{u}_c = \frac{1}{2}\left(1 - k_D^{-2}\hat{k}_y^2\right)\left(\overline{v_1' q_1'} - \overline{v_2' q_2'}\right) - \kappa \overline{u}_c. \tag{8.6}$$

The two-layer equations for the disturbances are derived in the same way as equation (3.6). They are

$$\frac{\partial q'}{\partial t} + \overline{u}_t \partial_x q' + \gamma_t \partial_x \psi' + \overline{u}_c \partial_x \zeta_c' + \left(\gamma_c - k_D^2 \overline{u}_c\right)\partial_x \tau' = -\kappa q' \tag{8.7}$$

$$\frac{\partial \sigma'}{\partial t} + \overline{u}_c \partial_x q' + \gamma_c \partial_x \psi' + \overline{u}_t \partial_x \sigma' + \gamma_t \partial_x \tau' = -\kappa \sigma', \tag{8.8}$$

where $\gamma_t = \partial_y \overline{q}$, $\gamma_c = \partial_y \overline{\sigma}$, and $\zeta_c' = \nabla^2 \tau$.

To investigate equations (3.5) and (3.6) numerically, we follow the method of Chapter 4, and assume the disturbance fields to be broadband in the k_y direction, but a function of one azimuthal wavenumber only: e.g., $q_t' = \mathrm{Re}[Q_t e^{ik_0 x}]$. This allows, after a little algebra, the derivation of the simplified one-dimensional equations

$$i\frac{\partial Q_t}{\partial t} = k_0\left(\overline{u}_t Q_t + \gamma_t \Psi_t + \overline{u}_c(Q_c + k_D^2 \Psi_c) + \left(\gamma_c - k_D^2 \overline{u}_c\right)\Psi_c\right) - i\kappa Q_t \tag{8.9}$$

$$i\frac{\partial Q_c}{\partial t} = k_0\left(\overline{u}_c Q_t + \gamma_c \Psi_t + \overline{u}_t Q_c + \gamma_t \Psi_c\right) - i\kappa Q_c \tag{8.10}$$

[1] It is worth noting here that the two-layer equations are directly analogous to the *two-level equations*, in which a binary discretisation of the continuous quasigeostrophic equation (2.20) is performed. See e.g., Pedlosky [44] for further details.

[2] Note for the worried mathematician reader: equation (8.6) can be rigorously derived by considering the Taylor expansion of the operator $\hat{k}_y^2 / \left(\hat{k}_y^2 + k_D^2\right)^{-1}$, with $\hat{k}_y = -i\partial_y$ as in Chapter 3, and k_D a constant.

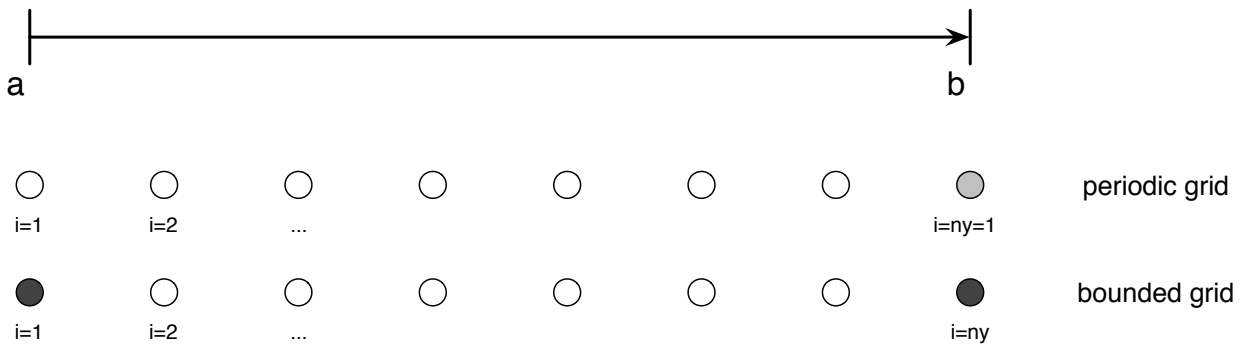

Figure 8.1: Schematic of the two different grids used in the reduced model. In the periodic grid, the value of all fields at the $i = 1$ point is set to that at the $i = n$ point at each timestep. In the bounded grid, all quantities are set to zero at $i = 1, n$.

and

$$\frac{\partial \overline{u}_t}{\partial t} = \mathcal{R}_t - \kappa \overline{u}_t \tag{8.11}$$

$$\frac{\partial \overline{u}_c}{\partial t} = \left(1 - k_D^{-2}\hat{k}_y^2\right)\mathcal{R}_c - \kappa \overline{u}_c \tag{8.12}$$

for waves and mean flow respectively, where

$$\mathcal{R}_t = +\frac{k_0}{2}\left(\mathrm{Im}[\Psi_t]\mathrm{Re}[\hat{k}_y^2\Psi_t] - \mathrm{Im}[\hat{k}_y^2\Psi_t]\mathrm{Re}[\Psi_t] + \mathrm{Im}[\Psi_c]\mathrm{Re}[\hat{k}_y^2\Psi_c] - \mathrm{Im}[\hat{k}_y^2\Psi_c]\mathrm{Re}[\Psi_c]\right) \tag{8.13}$$

$$\mathcal{R}_c = -\frac{k_0}{2}\left(\mathrm{Im}[\Psi_c]\mathrm{Re}[Q_t] - \mathrm{Im}[Q_t]\mathrm{Re}[\Psi_c] + \mathrm{Im}[\Psi_t]\mathrm{Re}[Q_c] - \mathrm{Im}[Q_c]\mathrm{Re}[\Psi_t]\right), \tag{8.14}$$

and

$$Q_t = -\left(\hat{k}_y^2 + k_0^2\right)\Psi_t \tag{8.15}$$

$$Q_c = -\left(\hat{k}_y^2 + k_0^2 + k_D^2\right)\Psi_c. \tag{8.16}$$

The coupled equations (8.9)-(8.16) are solved numerically by the same explicit 4^{th} order method as in Chapter 4.

Initial tests of the model were performed with periodic boundary conditions for simplicity; these are described in the next section. However, a bounded domain was used for the direct experimental simulations. The two different grids used are compared in Figure 8.1.

In the latter case, it was chosen to use non-slip boundary conditions for the zonal flow and free-slip for the eddy fields, which corresponds to the requirement that

$$\overline{u}_t = \overline{u}_c = \psi_t' = \psi_c' = 0, \qquad r = a, b. \tag{8.17}$$

While they may appear rather unusual, these conditions are necessary in order to ensure energy and mass conservation in the model [45]. The issue of physical boundary conditions in quasigeostrophic models is a long and contentious one, and we will not attempt to fully describe the details of the problem here. For further information, Davey (1978) is recommended [15].

Finally, we also note that thermal forcing and viscous damping are to be included in the final simulations. These additions are described after basic model validation, in Section 8.3.

8.2 Model validation

One of the most attractive features of the two-layer equations is that they can be linearised and solved *exactly* for the β-plane baroclinic instability problem. This is extremely useful for code validation, as it allows the output of the model to be tested against known analytical predictions.

By assuming that the barotropic mean flow is zero, that the baroclinic mean flow has the constant value U and that there is no Ekman or viscous damping, equations (8.9)-(8.11) can be greatly simplified. If $Q_t(y,t)$ and $Q_c(y,t)$ are then written in terms of the usual modal variables ω and k_y, (such that e.g., $Q_t = Q_0 e^{ik_y y - i\omega t}$) the linear dispersion relation

$$\omega = \frac{1}{2}\left(\omega_\psi + \omega_\tau\right) \pm \frac{1}{2}\sqrt{\left(\omega_\psi - \omega_\tau\right)^2 - 4A(B-A)} \tag{8.18}$$

results [58]. Here, ω_ψ and ω_τ are the free barotropic and baroclinic wave frequencies

$$\omega_\psi = \frac{-\beta k_0}{k_0^2 + k_y^2}, \qquad \omega_\tau = \frac{-\beta k_0}{k_0^2 + k_y^2 + k_D^2} \tag{8.19}$$

and the other constants are defined as

$$A = \frac{k_0 |\mathbf{k}| U}{\sqrt{k_0^2 + k_y^2 + k_D^2}} \qquad \text{and} \qquad B = \frac{k_0 k_D^2 U}{|\mathbf{k}|\sqrt{k_0^2 + k_y^2 + k_D^2}}. \tag{8.20}$$

In Figure 8.2(a), the analytical growth rate $\omega_i \equiv Im[\omega]$ according to (8.18) is plotted as a function of the parameters U and $|\mathbf{k}| = \sqrt{k_0^2 + k_y^2}$ (which are shown in dimensionless units for this example). The red curve shows the boundary between stable and unstable flows.

In Figure 8.2(b), the growth rate as predicted by the reduced model with periodic boundary conditions and resolution $ny = 64$ is shown. The growth rate in the model was calculated by starting a simulation with a constant baroclinic zonal flow $\overline{u}_c(y) = U$, zero mean barotropic flow and a small amplitude random initial condition for the waves. After a model evolution time of 100 dimensionless units, with barotropic and baroclinic zonal flow held constant, a combined Fourier-Laplace transform was then used to acquire the growth rates of individual modes.

As can be seen, the model agrees closely with analytical predictions. The only minor deviations occur at the top-left instability boundary, where forcing amplitude U is high and absolute wavenumber is low. As the experimental simulations involve flows that were typically well within the instability region, these deviations were not regarded as significant. In Figure 8.3, growth rate is plotted against north-south wavenumber k_y, with model results given by the red circles and analytical predictions by the black curve. Again, the model results match the predictions closely, showing that in the linear regime the model is indeed behaving as expected from theory.

Next, the model was tested in the nonlinear regime, with zonal flow evolution due to eddy interaction included. In order to test energy conservation of the model, a simulation was performed with forcing and damping switched off, in the same doubly periodic channel domain as before. At each step, the energy of each component was recorded and the total energy computed according to (2.53). As can be seen from Figure 8.4, total energy was conserved by the system despite significant variations in the energy of the different barotropic and baroclinic components. In Figure 8.5, the steady-state energy flow in the model when forcing and damping are included is summarised in terms of a block diagram.

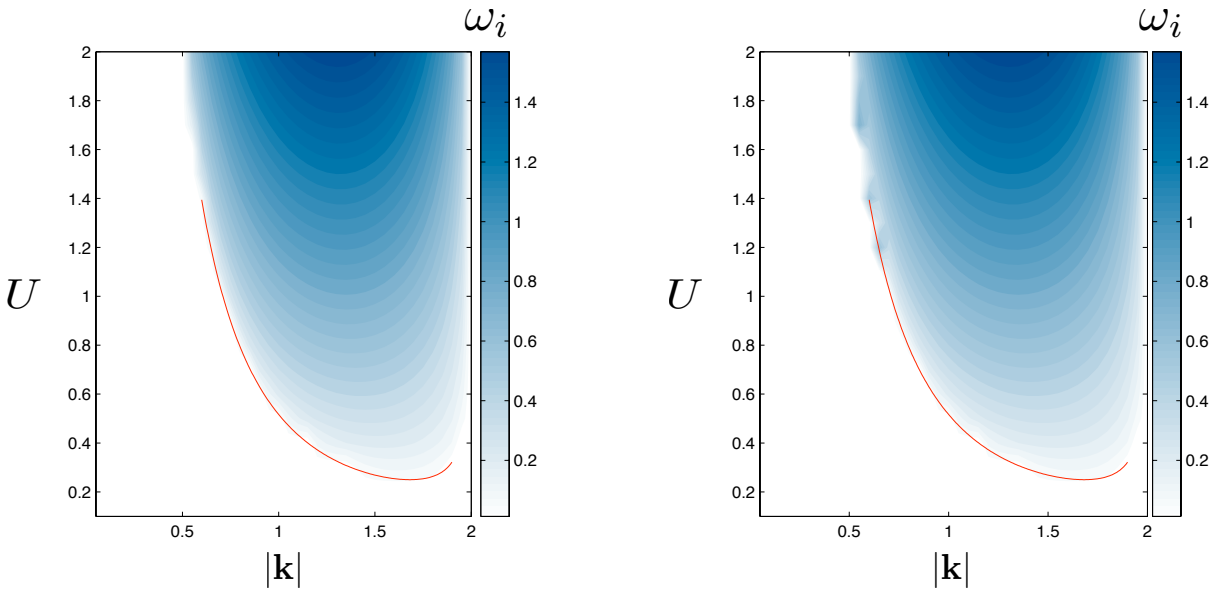

Figure 8.2: Contour plot of baroclinic instability growth rate vs. absolute wavenumber $|\mathbf{k}|$ and baroclinic shear strength U according to (a) analytical predictions and (b) the numerical model.

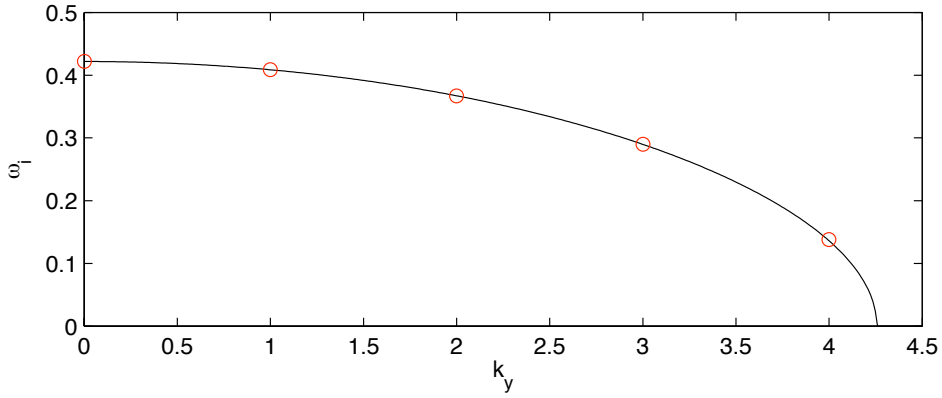

Figure 8.3: Plot of baroclinic instability growth rate vs. radial wavenumber k_y. The black line is the analytical prediction, while the red dots are output from the reduced model in a periodic boundary configuration, with Ekman damping, viscosity and mean flow evolution all set to zero.

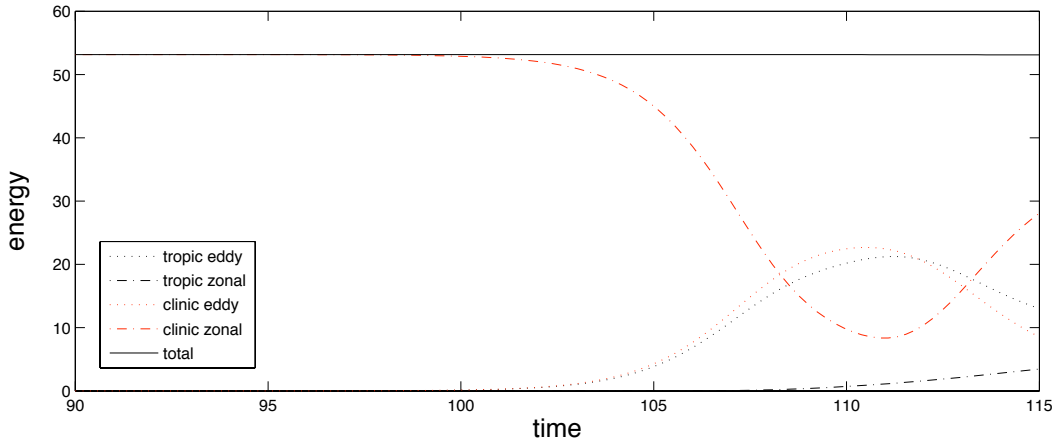

Figure 8.4: System energy as a function of time for a reduced model simulation in the periodic configuration, with Ekman damping and viscosity set to zero.

8.3 Simulation of the sloping boundary experiment

To simulate the sloping boundary results of Chapter 6, it is necessary to include several extra features in the model. First, quasigeostrophic boundary conditions are enforced at $r = a, b$, as described in Section 8.1. Second, as steady-state solutions are desired, thermal forcing must included to balance the Ekman damping.

The simplest possible form of forcing involves linear relaxation to a fixed baroclinic mean flow. The baroclinic forcing amplitude, U_f, can be related to real experimental parameters by dimensional analysis. Approximately, the thermal wind equation

$$2\Omega \frac{\partial u_\theta}{\partial z} = \frac{g}{\rho} \frac{\partial \rho}{\partial r}, \tag{8.21}$$

combined with the hydrostatic balance approximation (2.6) and the linear equation of state

$$\rho = -\rho_0 \alpha (T - T_0) \tag{8.22}$$

can be used to derive the expression

$$U_f = \frac{\alpha \Delta T g d}{4\Omega(b-a)}. \tag{8.23}$$

Thus baroclinic forcing amplitude is proportional to the applied horizontal temperature difference. Following previous quasigeostrophic studies of baroclinic instability in a heated annulus [35], the form of the forcing is chosen to be linear relaxation to a sine function over the channel

$$\mathcal{F} = \kappa(U_f \sin(\pi r/(b-a)) - \overline{u}_c). \tag{8.24}$$

The deformation wavenumber k_D was taken to be π/L_D, with L_D the deformation scale as defined by (6.1). For simplicity, the factor χ was taken to be unity. Although this means that k_D in the

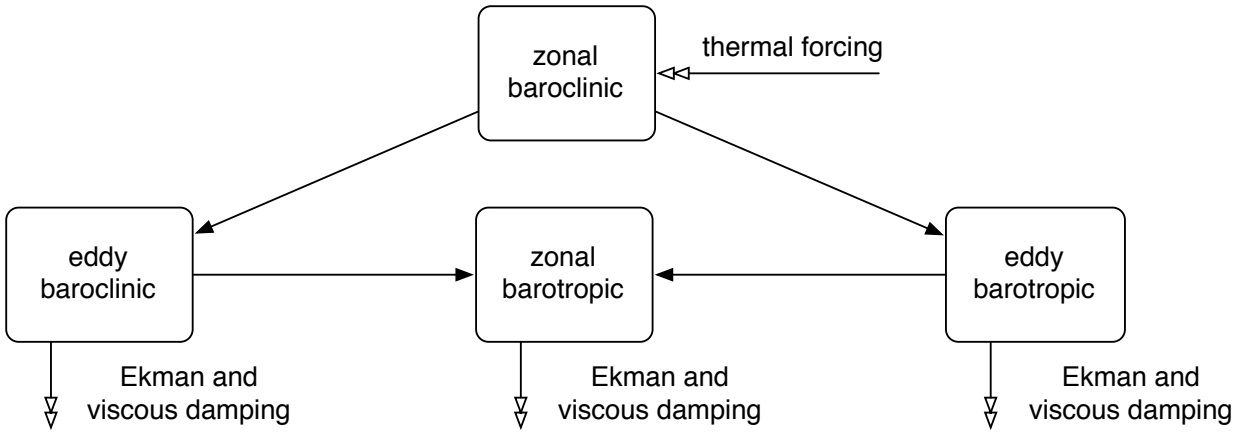

Figure 8.5: Schematic of energy flow in the reduced model when forcing and damping are present.

simulation will be an underestimate of its experimental value, the difference was not judged to be significant given the other approximations already made.

Initially, runs were perfomed with only these modifications present; the effects of direct viscous damping, in particular, were neglected. It was found that a large number of multiple jets typically formed in these runs, with the jets frequently becoming barotropically unstable before a steady state was reached. It was then decided to include the effects of viscous damping, which are almost always ignored in quasigeostrophic models of atmospheric flow, but are of importance in the laboratory. This caused a dramatic difference in the flow evolution; fewer jets formed, and those that did stayed barotropically stable. The relative effects of Ekman and viscous damping, displayed in Figure 8.7 for a typical simulation run, are discussed further later in this section.

With all new terms included, the model equations therefore become

$$\frac{\partial \overline{u}_t}{\partial t} = \mathcal{R}_t - \kappa \overline{u}_t + \nu \partial_{yy} \overline{u}_t \tag{8.25}$$

$$\frac{\partial \overline{u}_c}{\partial t} = \left(1 + k_D^{-2} \partial_{yy}\right) \mathcal{R}_c + \mathcal{F} + \nu \partial_{yy} \overline{u}_c \tag{8.26}$$

$$i \frac{\partial Q_t}{\partial t} = k_0 \left(\overline{u}_t Q_t + \gamma_t \Psi_t + \overline{u}_c \zeta_c + \left(\gamma_c - k_D^2 \overline{u}_c \right) \Psi_c \right) - i\kappa Q_t + i\nu (\partial_{yy} - k_0^2) Q_t \tag{8.27}$$

$$i \frac{\partial Q_c}{\partial t} = k_0 \left(\overline{u}_c Q_t + \gamma_c \Psi_t + \overline{u}_t Q_c + \gamma_t \Psi_c \right) - i\kappa Q_c + i\nu (\partial_{yy} - k_0^2) Q_c. \tag{8.28}$$

A schematic of the expected energy flow in the model is shown in Figure 8.5. Initially, all energy is concentrated in the axisymmetric baroclinic shear flow, $\overline{u}_c$. As the flow is unstable, it causes baroclinic and barotropic eddies to grow. As the eddies grow larger, they begin to transfer energy to the barotropic zonal jets. Eventually, a steady state is reached where Ekman and viscous damping of the eddies and barotropic mean flow balances the energy input to the baroclinic mean flow due to thermal forcing.

It was decided to set the azimuthal wavenumber $m = 15$ for the comparison simulation, corresponding to $k_0 = 2m/(b-a) = 3.06$ rad cm^{-1}. This value was chosen because barotropic energy was observed to peak there in the spectral plots (see Figure 6.15 in Chapter 6). Later in this section, the effects of varying wavenumber on the model results are considered.

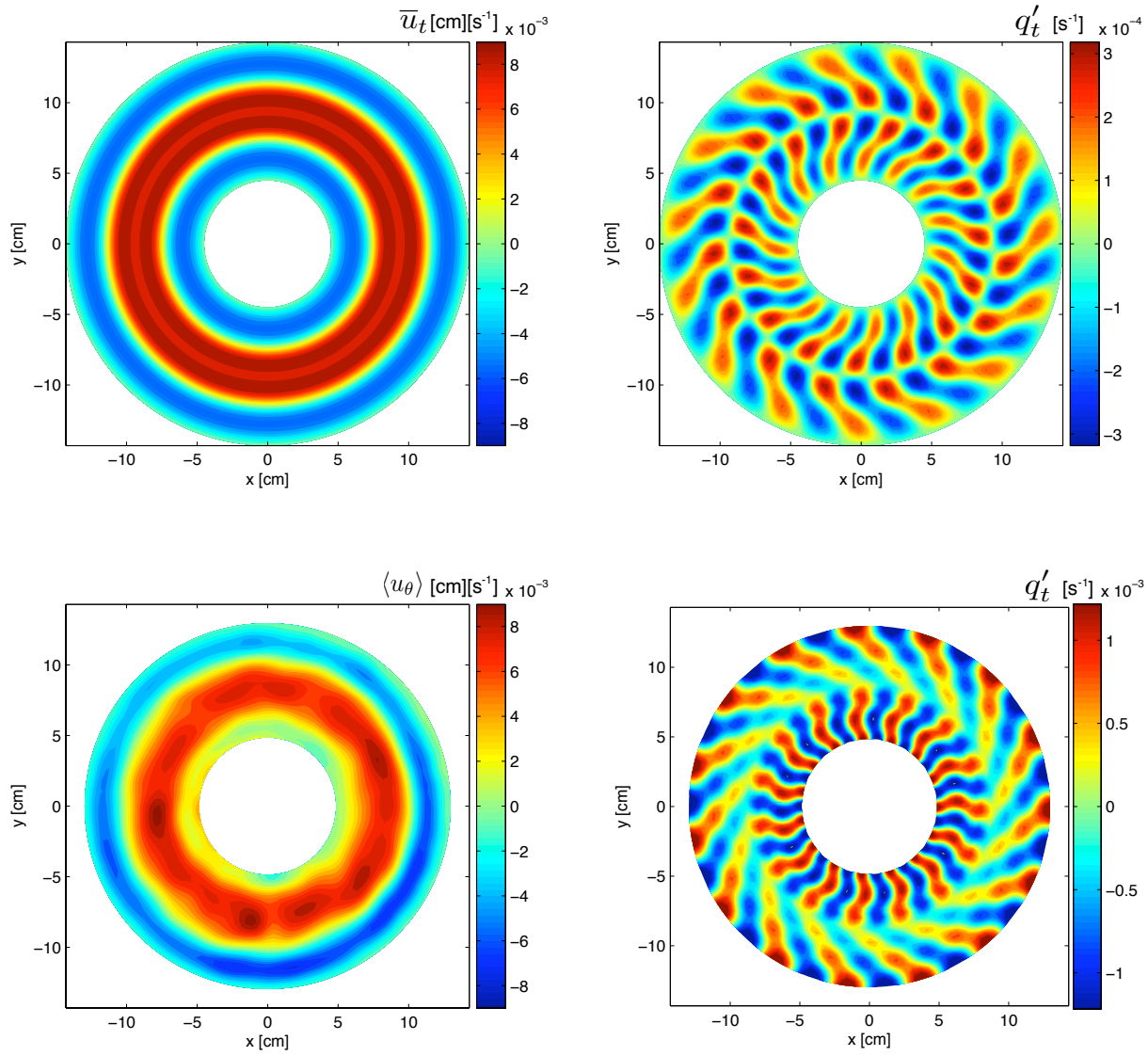

Figure 8.6: Steady-state barotropic zonal velocity (left) and $m = 15$ eddy barotropic potential vorticity (right) in a reduced model simulation with forcing and damping present (top) and in a real experiment (bottom). As in Chapter 6, barotropic fields for the experiment were produced by vertical averaging.

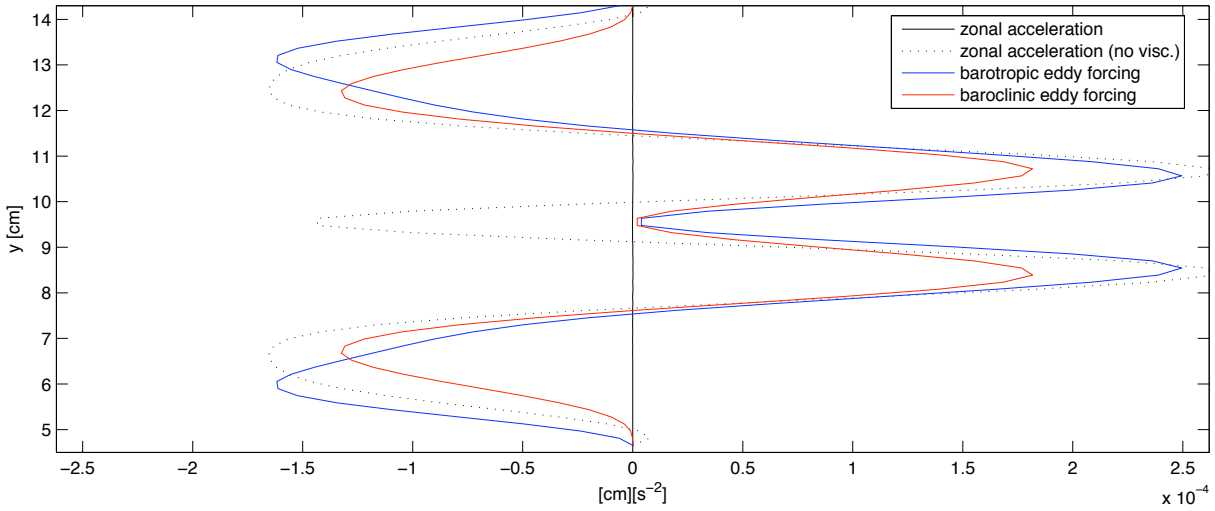

Figure 8.7: Plot of barotropic and baroclinic eddy forcing alongside zonal acceleration (with and without viscous damping included) for the steady-state barotropic zonal flow.

The effects of varying radial resolution were tested and found to be negligible for the value chosen ($nr = 64$). Indeed, it was found that the model produced qualitatively similar results with resolution as low as $nr = 16$! The viscous effects, which preferentially damp small scales, were believed to be the primary reason for this.

In Figure 8.6, output of the model and experimental results are directly compared. On the left, plots of time-averaged zonal velocity in the steady-state regime are shown. On the right, instantaneous barotropic eddy vorticity for the $m = 15$ azimuthal mode is displayed. The external parameters for the simulation and experiment are identical, except for the forcing amplitude U_f, which is 3.5 times greater in the simulation. The reasons for this will be discussed shortly.

As can be seen, the quantitative correspondence between the barotropic zonal flow in the two cases is remarkably close. There is also qualitative similarity between the $m = 15$ barotropic eddy vorticity fields; in particular, the 'tilt' of the wavefield is the same, indicating that the eddies are transporting momentum into the jet in both cases. Quantitatively, however, the experimental eddy vorticity is stronger, by a factor of around four.

In Figure 8.7, the various forces balancing the acceleration of the barotropic zonal flow in the steady state are shown. Blue and red lines show the barotropic and baroclinic forcing terms, while the dotted black line shows what the zonal acceleration *would* be if viscous damping was not present. As can be seen, direct viscous effects play a very important role in keeping the steady-state jet

Table 8.1: Parameters of the chosen comparison experiment.

Sloping boundary angle	δ	22°
Kinematic viscosity of fluid	ν	2.04×10^{-6} m^{2}s^{-1}
Radial temperature difference	ΔT	2K
Rotation rate	Ω	3.9 rad s^{-1}
Effective baroclinic shear	U_{expt}	0.0872 cm s^{-1}

stable.

To produce a barotropic jet that quantitatively matched that in the experiment, it was necessary to increase the forcing parameter U_f by a factor of 3.5. To determine the effect of varying baroclinic forcing in general, a series of runs were performed with different values of forcing amplitude U_f. In Figure 8.8 (top), maximum absolute barotropic zonal velocity u_{max} as a function of forcing amplitude is displayed. Three example steady-state barotropic jet profiles are also displayed below.

As can be seen, there is an initial region below a critical forcing threshold in which the system is stable and eddy growth cannot occur (just as in the linear problem described in Section 8.2). Once instability is possible, the dependence of u_{max} on U_f appears approximately linear, with some changes in the gradient occurring at certain values in concert with a change in the number of steady-state jets (e.g., $3 \rightarrow 2$ jets at $U_f \approx 0.3$ cm s^{-1}). Beyond a second critical value, the barotropic jets produced were unstable. Note that some evidence of multiple equilibria was found in the system; two runs with identical parameters but different initial small random fields for Q_t and Q_c were sometimes found to produce different steady-state jets. Most commonly, there were only two equilibria, consisting of jets with equal magnitude, but opposite sign.

The effect of varying azimuthal wavenumber in the simulation was also studied. Results are plotted in Figure 8.9, with the format similar to that in the previous example. Interestingly, u_{max} was observed to peak at around $m = 20$, a value slightly higher than that chosen for the simulation. As in the case of varying U_f, abrupt changes in the steady-state jet profile were also observed, with the $m = 16$ results (centre bottom of Figure 8.9) showing two jets instead of three.

The inclusion of viscous damping in the model tends to smooth out both the zonal flow and eddy wave action in the radial direction. As a result, the phase space view used so extensively in Chapter 4 is less revealing than in the invisicid case; eddy wave action tends to have very low wavenumber values, with little spatial wavenumber variation. For this reason, it was decided not to analyse the phase space distribution of barotropic and baroclinic modes in this Chapter.

8.4 Discussion

The results of this chapter demonstrate that the jet formation observed in the rotating annulus experiment can be qualitatively reproduced with an extremely reduced and simplified model. In essence, the full three-dimensional Navier-Stokes equations, which could be used at great computational cost to describe the annulus flow with high accuracy, have been reduced down to four coupled one-dimensional equations.

Table 8.2: Reduced model parameters.

Radius of inner cylinder	a	4.5 cm
Radius of outer cylinder	b	14.3 cm
Kinematic viscosity of fluid	ν	2.04×10^{-6} m^{2}s^{-1}
Beta parameter	β	0.2932 cm^{-1}s^{-1}
Radial resolution	nr	64
Azimuthal wavenumber	m	15
Forcing amplitude	U_f	3.5 U_{expt}

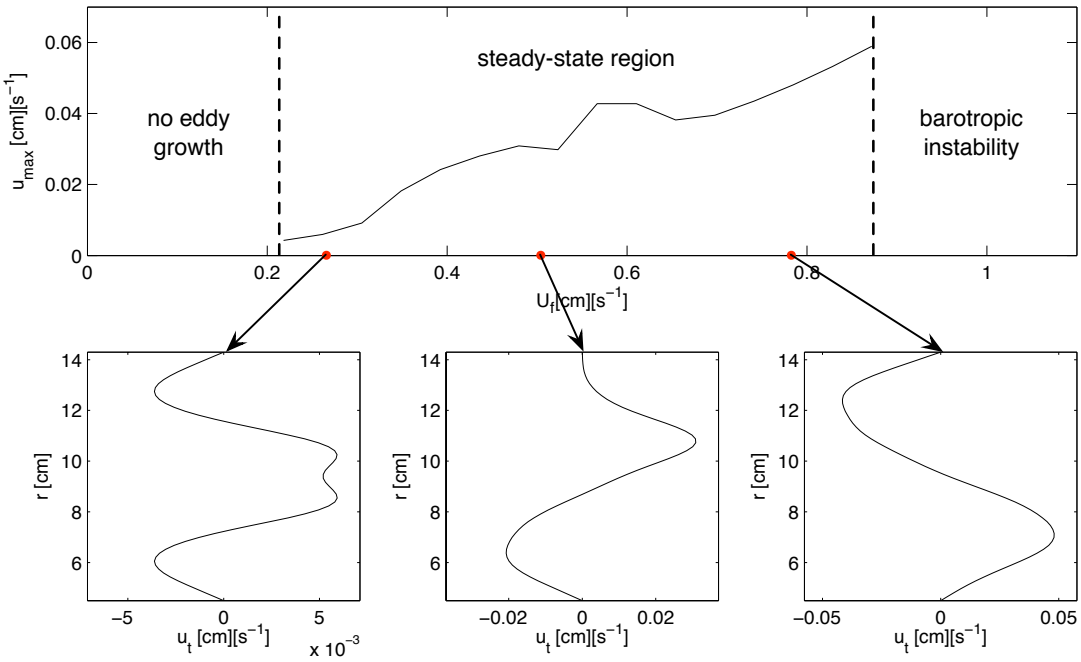

Figure 8.8: The effects of varying baroclinic forcing on the maximum steady-state barotropic zonal velocity u_{max}. Three example barotropic jet profiles are also shown.

The main discrepancy between the experiment and the model is that the model requires a greater effective temperature difference (baroclinic forcing amplitude) to produce a barotropic jet of the same magnitude. This is almost certainly due to the fact that the model artificially excludes all azimuthal modes except for the zonal flow and the waves. As a result, a given baroclinic zonal shear equilibrates with a comparatively smaller amount of total eddy wave action and hence tends to produce a weaker barotropic jet.

It would of course be interesting in future work to generalise the reduced model to include multiple azimuthal modes, possibly along with an option to include full nonlinear interactions. However, the simplicity of the model, combined with its success in predicting qualitative features of the jets, provides a strong argument that wave-mean flow interaction is the key to the dynamics of the experimental system.

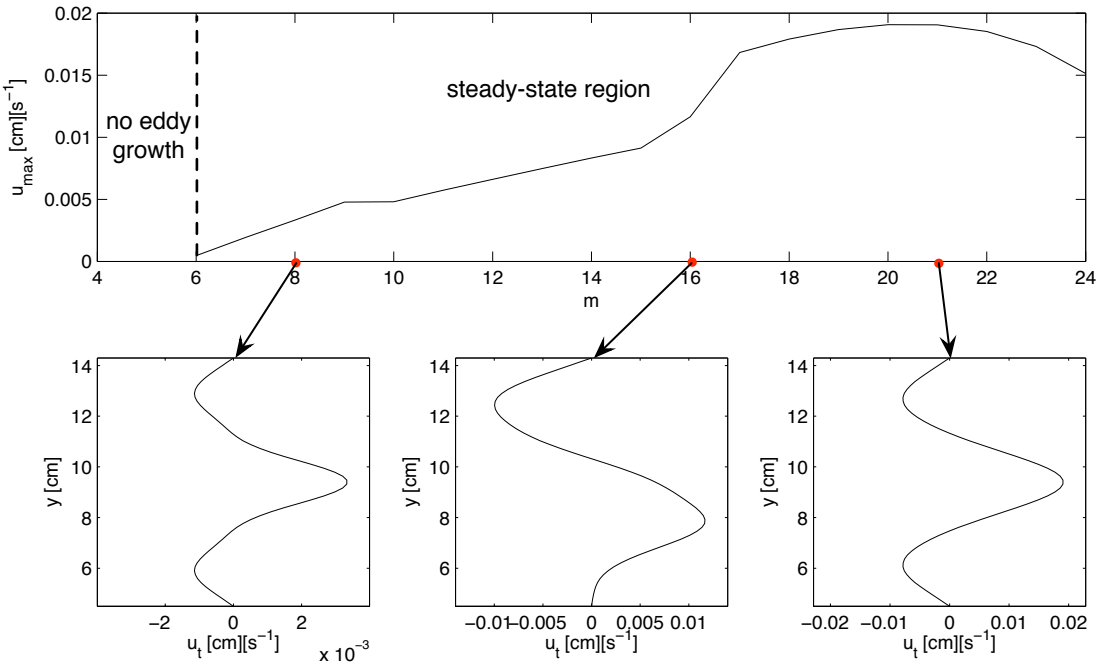

Figure 8.9: The effects of varying azimuthal mode m on the maximum steady-state barotropic zonal velocity u_{max}. Three example barotropic jet profiles are also shown.

Chapter 9

Conclusion

9.1 Summary of results and discussion

What has been achieved in this thesis?

Let us begin the discussion by reviewing the theoretical section (Chapters 3 and 4). In Chapter 3, it was shown that the nonlinear interaction between an arbitrary zonal flow and a broadband distribution of planetary waves can be expressed in terms of the Wigner distribution, a tool first developed in quantum mechanics. In the following chapter, the Wigner distribution was used to analyse and interpret the results of a wave-mean flow numerical simulation.

The derivation presented in Chapter 3 generalised previous results on the subject, also highlighting some interesting links between wave-mean flow theory and quantum mechanics. However, it still made one large assumption: that of no wave-wave interaction. The aim of Chapter 4 was to study jet formation in as reduced a form as possible. Although the numerical model described there was extremely simplified, it was possible to use it to explain jet formation and asymmetry in a simple test case. Several possible extensions of the model were suggested in Section 4.5, including the addition of random forcing, to study the case of multiple jet formation. In Chapter 8, the model was extended to include the effects of vertical stratification.

It should be noted that other phase space analysis techniques, such as the wavelet transform, have been used with some success in fluid dynamics to analyse the properties of chaotic and turbulent flows (see e.g., van der Berg (2004) for a review of wavelet techniques [65]). However, the Wigner distribution has several important advantages. First, as was shown in Chapter 3, it can be used to directly derive *dynamical* wavepacket transport equations, extending its use beyond a purely diagnostic role. Second, when correctly defined, as in the derivation given here, its projection onto real space is the wave action of the disturbance field. This fact connects the phase and real space views directly, allowing previous theoretical results on the subject to be combined. If the idea of treating classical fields as ensembles of interacting wavepackets has future merit, therefore, it is likely that the Wigner distribution will continue to play a central role.

In the second main part of this thesis (Chapters 5-7), a laboratory study of fluid motion in a differentially heated rotating annulus at high Taylor and low Hide numbers was presented. A range of experiments were performed with both flat and sloping top and bottom boundaries. Some experiments were also performed with a vertical flow barrier present in the annulus.

In Section 1.4, we posed six key questions about jet formation in the experiment. They are reproduced below for convenience:

- Do multiple barotropic jets develop in the experimental system?
- If so, are the jets dynamically stable?
- How do they interact with the turbulent eddies?
- Is a turbulent cascade of energy from small to large scales occurring?
- If not, can wave-mean flow theory be used to describe the jet formation process?
- Do jets form in the annulus when a vertical flow barrier is also present?

The first question is easily answered by referring to Figures 6.7-6.8. Multiple jets *do* form in the sloping boundary experiments, but only under special conditions: high rotation rate, low viscosity, and relatively low thermal forcing.

The jets were found to be barotropically stable *at all times*. This is in contrast to the experiment of Read et al. [52], where the instantaneous zonal flow was found to be unstable, but the time-averaged flow tended towards a marginally stable state. It is possible that the barotropic stability of the flow may have been of importance in suppressing eddy-eddy interactions; although as is discussed below, there was also evidence of spectrally nonlocal interactions in the experiment of Read et al..

The third, fourth and fifth questions are intimately related to each other. Initially, the problem of jet-eddy interaction was tackled in the most obvious and simple way possible; via a Reynolds stress analysis (Section 6.1). It was found that generally, eddy momentum fluxes converged onto same-signed zonal flow in the sloping boundary experiments, but onto opposite-sign zonal flow in the flat boundary cases. This result provided direct evidence that the multiple barotropic jets in the sloping case were at least partially sustained by the horizontal transport of eddy momentum.

Through a quasigeostrophic assumption, approximate eddy temperature fields were derived and used to calculate the radial eddy heat flux. It was found that, as expected, that eddies always transported heat radially inwards ('poleward'). However, the lack of direct thermal data meant that the relative effect of heat flux divergence on the zonal flow evolution was difficult to determine accurately. The crude E-P analysis performed suggested that heat flux effects may have been greater than momentum flux effects, implying a zonal flow mainly driven by thermal eddy effects.

Answering the fourth question was more challenging. In order to address it, an expression for the transfer of kinetic energy between different azimuthal barotropic modes of the system was derived (6.10). Transfer of energy between different radial and vertical modes was ignored, in order to keep the calculation as simple as possible. It was found that energy transfer was typically nonlocal in the subset of triads analysed, especially in the sloping boundary experiments, where energy transfer from high and intermediate wavenumbers to the $m = 0$ zonal flow dominated in almost all cases. Although energy transfer was from smaller to larger scales in almost every case studied, spectrally local energy transfer was not observed in experiments where sloping boundaries were present.

In Read et al. [52], a spectral transfer analysis of the experimental results was also performed, although in their work, only the energy transfer from small to large scales was computed. As in the experiment presented here, the transfer was found to be strongly nonlocal when sloping boundaries

were present, with energy flow to zonal modes dominating over other interactions. Although the effects of varying rotation rate and forcing on the spectral transfer were not studied, their result does indicate that nonlocal interaction may even occur in systems with much weaker viscous damping than the experiment studied here.

In Chapter 8, the wave-mean flow numerical model used in Chapter 4 was generalised to two layers, in order to address the fifth question posed in the introduction. It was found that the jet formation observed in the experiment *could* be qualitatively reproduced by the numerical model, although quantitatively, there were differences between the two cases.

For simplicity, the model focused on the interaction between the zonal flow and only one azimuthal mode, which was chosen to correspond to the most energetic non-zonal mode in the experiment, as observed from kinetic energy spectra (Figure 6.15). A numerical code that described the interaction between zonal flow and all azimuthal modes would have been much more complex, which would have weakened the motivation for constructing the reduced model in the first place. However, it is possible that such a model would have reproduced the experimental flow more accurately than that described here.

It is of much interest to compare the experimental results with the observed properties of real planetary-scale fluid motion. The sloping boundary results are perhaps most relevant to the state of Earth's atmosphere at mid-latitudes. As described in Chapter 1, the eastward Atlantic jet stream is known to be partially maintained by a combination of eddy heat and momentum fluxes — much like the jets produced in the sloping boundary experiments.

Typically, the deformation radius in the midlatitude troposphere is of order 1000km [58], and the width of the jet stream is approximately 5000km. In the high rotation rate sloping boundary experiments, the horizontal buoyancy scale (6.1) was approximately $1/10^{\text{th}}$ of the channel width, implying the relative deformation scales may be roughly comparable in these two systems. As with any laboratory study, a key problem in making comparisons comes from the fact that Ekman damping and viscous damping is always greater than that in planetary atmospheres. In Chapter 8, it was seen that viscous damping, in particular, has a dramatic effect on the flow, increasing barotropic stability and reducing the total number of steady-state jets.

Despite these important differences, the results here raise interesting questions regarding the real atmosphere that may well be worth pursuing further. The spectral transfer result, in particular, deserves further investigation, as established theory on atmospheric turbulence often assumes a more standard cascade picture of planetary-scale turbulence. If wave-mean flow interactions are found to be dominant in Earth's atmosphere, it could well have interesting implications for the climate modelling community. This point is discussed further in the next section.

It is also interesting to compare these results with the zonation observed on gas giant planets. The differences in the gas giant case are somewhat greater, as interior convection, rather than baroclinic instability, may well be the dominant forcing mechanism there. Also, the observed Jovian jets are persistently barotropically unstable, whereas the ones produced by this experiment were stable. However, the basic mechanism of multiple jet formation due to eddy flux divergences does appear to be the same in both cases. Whether or not a spectrally local turbulent cascade from eddy to jet scales is occurring on the gas giant planets is, to the author's knowledge, still an open question.

The final question in the list was answered in Chapter 7, where the results of experiments with both sloping boundaries and a vertical wall were reported. In the experiments, a gyre and 'western' boundary current were observed at low rotation rates, in agreement with the findings of Rayer et al.

[48]. At moderate rotation rates, eddies appeared near the inner cylinder, but did little to affect the steady-state appearance of the gyre. At high rotation rates, however, the eddies intensified and spread throughout the channel. Simultaneously, the gyre was observed to split, with time-averaged zonal velocity plots clearly showing the presence of multiple jets at mid-depth.

As mentioned in Chapter 1, some evidence of multiple jet formation has already been observed in ocean simulations of varying complexity [55]. However, there is still active debate as to whether the dynamical jet formation process can be the same as that seen in planetary atmospheres. For example, in a recent numerical study by Berloff (2005), an alternative explanation of oceanic jet formation in terms of the nonlinear interaction of resonant basin modes was suggested [10]. This study is the first one to directly compare flows in the jet regime with and without vertical boundaries present. For this reason, it should prove of relevance to the wider oceanographic debate.

9.2 Future work

There are clearly many ways in which the work presented here could be extended and generalised. We begin with a discussion of the experimental part of the thesis.

The most obvious weak point of the experimental results is a lack of direct information on the temperature of the fluid interior. In order to resolve some of the remaining questions about the relative importance of eddy momentum and heat fluxes, it is strongly recommended that any future investigators make the acquisition of velocity *and* temperature field information their priority. As discussed in Chapter 5, the PIT (particle imaging thermometry) method appears to hold the greatest long-term potential for this purpose. The challenge in implementing PIT is a technological one; in particular, effective lighting and a high-quality colour camera are required for it to be successful.

In terms of the broader scientific picture, the most logical extension of the experimental work would be a much wider study of geophysically relevant baroclinically forced jet regimes, with a particular focus on the nature of the zonal-eddy and eddy-eddy interactions. Such a project could be carried out either experimentally, or using a fully nonlinear numerical simulation.

The key challenge in performing any study, numerical or experimental, is reducing the damping of the system, in order to reach conditions closer to those of real planetary-scale flows. Extremely high resolution numerical simulations would probably be capable of quantitatively reproducing the results of the experiments reported here. However, larger facilities, such one in which the experiments of Read et al. [52] were conducted, are still far beyond the effective reach of fully three-dimensional, unparameterised numerical simulation. If a baroclinic turbulence study were technologically feasible in a large-scale apparatus, therefore, the experimental approach would probably be the best one to pursue.

There would also be much to be gained from a systematic study of jet formation regimes in simple systems with ocean basin boundary conditions. As current state of the art ocean simulations still lack the necessary resolution to resolve many important dynamical processes (particularly baroclinic instability), the detailed study of simplified systems may prove of great benefit to our understanding of the differences between the ocean and atmospheric cases.

The results of Chapters 3 and 4 have shown that phase space analysis techniques can give much insight in wave-mean flow problems. In Chapter 8, however, the viscous terms in the fluid equations

meant that higher wavenumbers were preferentially damped away, and application of phase space ideas to the problem ultimately proved unrevealing.

As an extension of the work in Chapter 4, therefore, it would be most interesting to apply the Wigner analysis to more strongly nonlinear simulations or experiments, possibly of the type just discussed. If wave-mean flow interactions turn out to be dominant even in these cases, then phase space analyses may well give greater insight into the dynamics.

Another possibility would be to investigate multiple jet formation via the modulational instability of planetary waves, using the numerical model of Chapter 4. Although a limiting case of the problem has been studied in [38], little investigation into more general cases has been made. Potentially, such a study could allow prediction of characteristic jet scales from first principles – something which has so far only been possible to achieve through scaling analysis.

Finally, the techniques described here could be utilised in many other wave-mean flow problems. One obvious candidate would be the interaction of quasigeostrophic vortices with inertia-gravity waves. Phase space analysis might in fact be particularly suited to this problem, as the scale separation between mean flow and waves is more distinct than in the planetary wave - zonal flow case.

More speculatively, the numerical model of Chapter 8 may also point to interesting possible future applications. At the time of writing, a letter has been published by O'Gorman and Schneider [42], in which the effects of removing all eddy-eddy interaction from a fully general circulation model were studied. In their work, it was found that many, but not all, features of general circulation remained the same when only eddy-mean flow interactions were permitted.

As was mentioned in Chapter 8, removing eddy-eddy interactions from numerical simulations allows the model run time to be dramatically shortened. If it can be more rigorously shown that wave-mean effects dominate in geophysically relevant fluid flows, then this opens up some intriguing possibilities for general climate simulations. For example, it is possible that by parameterising, or even neglecting eddy-eddy interactions altogether, fast, simple GCMs could be constructed. As much of the current focus of climate research is on ensemble forecasting, which involves extremely large numbers of similar simulations, such an improvement could possibly allow the exploration of multi-dimensional parameter regimes in far more detail than has so far been possible.

Bibliography

[1] A. Abdulrahman, C. A. Jones, M. R. E. Proctor, and K. Julien. Large wavenumber convection in the rotating annulus. *Geophys Astrophys Fluid Dyn*, 93(3):227–252, 2000.

[2] D. G. Andrews, C. B. Leovy, and J. R. Holton. *Middle Atmosphere Dynamics*. Academic Press, 1987.

[3] D. G. Andrews and M. E. McIntyre. Planetary waves in horizontal and vertical shear: the generalised Eliassen-Palm relation and the mean zonal acceleration. *J Atmos Sci*, 33:2031–2048, 1976.

[4] D. G. Andrews and M. E. McIntyre. An exact theory of nonlinear waves on a Lagrangian-mean flow. *J Fluid Mech*, 89:609–646, 1978.

[5] G. B. Arfken and H. J. Weber. *Mathematical methods for physicists*. Harcourt Academic Press, 2001.

[6] F. Bagenal, T. Dowling, and W. McKinnon. *Jupiter: The Planet, Satellites and Magnetosphere*. Cambridge University Press, 2004.

[7] M. E. Bastin and P. L. Read. Experiments on the structure of baroclinic waves and zonal jets in an internally heated, rotating, cylinder of fluid. *Phys Fluids*, 10(2):374–389, 1998.

[8] G. K. Batchelor, H. K. Moffatt, and M. G. Worster, editors. *Perspectives in fluid dynamics*. Cambridge University Press, 2000.

[9] E. S. Benilov, V. G. Gnevyshev, and V. I. Shrira. Nonlinear interaction of a zonal jet and barotropic Rossby-wave turbulence: the problem of turbulent friction. *Dynamics of Atmospheres and Oceans*, 16:339–353, 1992.

[10] P. S. Berloff. On rectification of randomly forced flows. *J Marine Res*, 63:497–527, 2005.

[11] F. H. Busse and C. R. Carrigan. Laboratory simulation of thermal convection in rotating planets and stars. *Science*, 191:81–83, 1976.

[12] A. Chekhlov, S. Orszag, S. Sukoriansky, B. Galperin, and I. Staroselsky. The effect of small-scale forcing on large-scale structures in two-dimensional flows. *Physica D*, 98:321–334, 1996.

[13] S. A. Condie and P. B. Rhines. A convective model for the zonal jets in the atmospheres of Jupiter and Saturn. *Nature*, 367:711–713, 1994.

[14] D. Dabiri and M. Gharib. Digital particle image velocimetry - theory and application. *Exp in Fluids*, 97:77–86, 1991.

[15] M. K. Davey. Recycling flow over bottom topography in a rotating annulus. *J Fluid Mech*, 87(3):497–520, 1978.

[16] A. I. Dyachenko, S. V. Nazarenko, and V. E. Zakharov. Wave-vortex dynamics in drift and beta-plane turbulence. *Phys Lett A*, 165(4):330–334, March 1992.

[17] A. Eliassen and E. Palm. On the transfer of energy in stationary mountain waves. *Geofysiske Publ*, 22:1–23‘, 1961.

[18] L. Elkins-Tanton. *Jupiter and Saturn*. Facts on File Inc, 2006.

[19] A. M. Fincham and G. R. Spedding. Low cost, high resolution DPIV for measurement of turbulent fluid flow. *Expt Fluids*, 23:449–462, 1997.

[20] R. Fjortoft. On the changes in the spectral distribution of kinetic energy for two-dimensional nondivergent flow. *Tellus*, 5:225, 1953.

[21] B. Galperin, S. Sukoriansky, N Dikovskaya, P. L. Read, Y. H. Yamazaki, and R. Wordsworth. Anisotropic turbulence and zonal jets in rotating flows with a beta-effect. *Nonlin Proc Geophys*, 13:83–86, 2006.

[22] A. D. Del Genio, J. M. Barbara, J. Ferrier, A. P. Ingersoll, R. A. West, A. R. Vasavada, J. Spitale, and C. C. Porco. Saturn eddy momentum fluxes and convection: first estimates from Cassini images. *Icarus*, 189:479–492, 2007.

[23] D. A. Godfrey. A hexagonal feature around Saturn's north pole. *Icarus*, 76:335–356, 1988.

[24] K. Hasselmann. On the non-linear energy transfer in a gravity-wave spectrum. Part 1: General theory. *J Fluid Mech*, 12:481–500, 1962.

[25] P. H. Haynes. On the instability of sheared disturbances. *J Fluid Mech*, 175:463–478, 1987.

[26] R. Hide. Some experiments on thermal convection in a rotating fluid. *Q J R Meteorol Soc*, 79:161, 1953.

[27] R. Hide. An experimental study of thermal convection in a rotating fluid. *Phil Trans R Soc Lond A*, 250:442–478, 1958.

[28] R. Hide, S. R. Lewis, and P. L. Read. Sloping convection: a paradigm for large-scale waves and eddies in planetary atmospheres. *Chaos*, 4:135, 1994.

[29] R. Hide and P. J. Mason. Sloping convection in a rotating fluid: a review. *Adv Phys*, 24:47–100, 1975.

[30] P. Hignett, A. A. White, R. D. Carter, W. D. N. Jackson, and R. M. Small. A comparison of laboratory measurements and numerical simulations of baroclinic wave flows in a rotating cylindrical annulus. *Q J R Meteorol Soc*, 467:131–154, 1985.

[31] H.-P. Huang and W. Robinson. Two-dimensional turbulence and persistent zonal jets in a global barotropic model. *J Atmos Sci*, 55:611–632, 1998.

[32] K. Itoh, S.-I. Itoh, P. H. Diamond, T. S. Hahm, A. Fujisawa, G. R. Tynan, M. Yagi, and Y. Nagashima. Physics of zonal flows. *Phys Plasmas*, 13(5):055502–055502–11, 2006.

[33] A. N. Kolmogorov. The local structure of turbulence in incompressible viscous fluid for very large Reynolds numbers. *Dokl Akad Nauk SSSR*, 30:301–305, 1941.

[34] S. Lee and H-K. Kim. The dynamical relationship between subtropical and eddy-driven jets. *J Atmos Sci*, 60:1490–1503, 2003.

[35] S. R. Lewis. *Long-lived eddies in the atmosphere of Jupiter*. PhD thesis, University of Oxford, 1988.

[36] M. S. Longuet-Higgins and A. E. Gill. Resonant interaction between planetary waves. *Proc Roy Soc A*, 120:299, 1967.

[37] E. N. Lorenz. Deterministic nonperiodic flow. *J Atmos Sci*, 20:130–141, 1963.

[38] D. Y. Manin and S. Y. Nazarenko. Nonlinear interaction of small-scale Rossby waves with an intense large-scale zonal flow. *Phys Fluids*, 6(3):1158–1167, March 1994.

[39] P. J. Mason. Baroclinic waves in a container with sloping endwalls. *Phil Trans R Soc Lond A*, 278:397–445, 1975.

[40] N. A. Maximenko, B. Bang, and H. Sasaki. Observational evidence of alternating zonal jets in the world ocean. *Geophys Rev Lett*, 32:L12607, 2006.

[41] A. C. Newell. Rossby wave packet interactions. *J Fluid Mech*, 35:255–271, 1969.

[42] P. A. O'Gorman and T. Schneider. Recovery of atmospheric flow statistics in a general circulation model without nonlinear eddy-eddy interactions. *Geophys Rev Lett*, 34:L22801, 2007.

[43] R. Lee Panetta. Zonal jets in wide baroclinically unstable regions: persistence and scale selection. *J Atmos Sci*, 50:2073–2105, 1993.

[44] J. Pedlosky. *Geophysical fluid dynamics*. Springer, 1987.

[45] N. A. Phillips. The general circulation of the atmosphere: a numerical experiment. *Q J R Meteorol Soc*, 82:123–164, 1956.

[46] R. A. Plumb. A new look at the energy cycle. *J Atmos Sci*, 40(7):1669–1688, 1983.

[47] W. H. Press, S. A. Teukolsky, W. T. Vetterling, and B. P. Flannery. *Numerical Recipes in C++: The Art of Scientific Computing*. Cambridge University Press, 2002.

[48] Q. G. Rayer, D. W. Johnson, and R. Hide. Thermal convection in a rotating fluid annulus blocked by a radial barrier. *Geophys Astrophys Fluid Dyn*, 87(3):215–252, 1998.

[49] P. L. Read. Finite-amplitude, neutral baroclinic eddies and mean flows in an internally heated, rotating fluid: 2. Effects of spatially varying N^2. *Dynamics of Atmospheres and Oceans*, 11:211–264, 1988.

[50] P. L. Read. Transition to geostrophic turbulence in the laboratory, and as a paradigm in atmospheres and oceans. *Surveys in Geophysics*, 22:265–317, 2001.

[51] P. L. Read, Y. H. Yamazaki, S. R. Lewis, P. D. Williams, K. Miki-Yamazaki, J. Sommeria, H. Didelle, and A. Fincham. Jupiter and Saturn's convectively driven jets in the laboratory. *Geophys Rev Lett*, 31:L22701, 2004.

[52] P. L. Read, Y. H. Yamazaki, S. R. Lewis, P. D. Williams, and R. D. Wordsworth. Dynamics of convectively driven banded jets in the laboratory. *J Atmos Sci*, 64:4031–4052, 2007.

[53] G. M. Reznik. On the energy transfer equation for weakly interacting waves. *J Nonlinear Mech*, 19:95–113, 1980.

[54] P. B. Rhines. Waves and turbulence on a beta-plane. *J Fluid Mech*, 69:417–443, 1975.

[55] K. J. Richards, N. A. Maximenko, F. C. Bryan, and H. Sasaki. Zonal jets in the Pacific Ocean. *Geophys Rev Lett*, 33(3):L03605, 2006.

[56] H. Riehl and D. Fultz. Jet stream and long waves in a steady rotating-dishpan experiment: Structure of the circulation. *Q J R Meteorol Soc*, 83(356):215–231, 1957.

[57] R. Salmon. Two-layer quasigeostrophic turbulence in a simple special case. *Geophys Astrophys Fluid Dyn*, 15:167–211, 1978.

[58] R. Salmon. *Lectures on Geophysical Fluid Dynamics*. Oxford University Press, 1998.

[59] C. Salyk, A. P. Ingersoll, J. Lorre, A. Vasavada, and A. D. Del Genio. Interaction between eddies and mean flow in jupiter's atmosphere: Analysis of cassini imaging data. *Icarus*, 185(2):430–442, 2006.

[60] S. Sukoriansky, N. Dikovskaya, and B. Galperin. On the arrest of inverse energy cascade and the Rhines scale. *J Atmos Sci*, 64(9):3312–3327, 2007.

[61] S. Sukoriansky, B. Galperin, and N Dikovskaya. Universal spectrum of two-dimensional turbulence on a rotating sphere and some basic features of atmospheric circulation on giant planets. *Phys Rev Lett*, 89:124–128, 2002.

[62] H. U. Sverdrup, M. W. Johnson, and R. H. Fleming. *The Oceans (Their Physics, Chemistry, and General Biology)*. Prentice-Hall Inc., 1942.

[63] A. Torre. *Linear Ray and Wave Optics in Phase Space*. Elesvier, 2005.

[64] G. K. Vallisa and M. E. Maltrud. Generation of mean flows and jets on a beta plane and over topography. *J Phys Ocean*, 23:1346–1362, 1993.

[65] J. C. van den Berg. *Wavelets in Physics*. Cambridge University Press, 2004.

[66] A. R. Vasavada, S. M. Hörst, M. R. Kennedy, A. P. Ingersoll, C. C. Porco, A. D. Del Genio, and R. A. West. Cassini imaging of Saturn: southern hemisphere winds and vortices. *J Geophys Res*, 111:E05004, 2006.

[67] F. Vettin. Über den aufsteigenden Luftstrom, die Entstehung des Hagels und der Wirbel-Stürme. *Ann Physik*, 178(10):246–255, 1857.

[68] G. P. Williams. Planetary circulations: barotropic representations of jovian and terrestrial turbulence. *J Atmos Sci*, 35:1399–1426, 1978.

[69] R. D. Wordsworth. Jet formation in planetary-scale fluids: a phase space view. *In preparation*, 2008.

[70] R. D. Wordsworth, P. L. Read, and Y. H. Yamazaki. Turbulence, waves and jets in a differentially heated rotating annulus experiment. *Phys Fluids (accepted for publication)*, 2008.

[71] R. D. Wordsworth, Y. H. Yamazaki, and P. L. Read. A laboratory analogue of zonal jet formation in Earth's oceans. *In preparation*, 2008.

[72] V. E. Zakharov, G. Falkovich, and V. S. Lvov. *Kolmogorov Spectra of Turbulence I*. Springer-Verlag, Berlin, 1992.

Appendix A

Acquisition of eddy streamfunction

Eddy streamfunction fields were used in Section 6.1, in order to estimate radial eddy fluxes of heat. They were derived via a standard finite-difference matrix inversion method, which we describe here.

The continuous relationship $\zeta' = \nabla^2\psi'$, $\psi'|_{r=a,b} = 0$ (see Section 6.1) becomes

$$\zeta' = \left(\frac{1}{r}\frac{\partial}{\partial r}\left(r\frac{\partial}{\partial r}\right) + \frac{1}{r^2}\frac{\partial^2}{\partial\theta^2}\right)\psi', \qquad \psi'|_{r=a,b} = 0 \tag{A.1}$$

in two-dimensional polar coordinates. Note that as derivation of T' from ψ' required use of the quasigeostrophic assumption, free-slip boundary conditions were judged to be most appropriate here.

Equation (A.1) can be written in finite difference form as

$$\zeta'_{i,j} = \frac{r_{i+\frac{1}{2},j}\psi'_{i+1,j} - 2r_{i,j}\psi'_{i,j} + r_{i-\frac{1}{2},j}\psi'_{i-1,j}}{r_{i,j}\Delta r^2} + \frac{\psi'_{i,j+1} - 2\psi'_{i,j} + \psi'_{i,j-1}}{r^2_{i,j}\Delta\theta^2},$$
$$\psi'_{i,j}|_{r_{i,j}=a,b} = 0. \tag{A.2}$$

Equation (A.2) was converted into a tridiagonal matrix (see e.g., [47]) and inverted using Matlab's *inv* matrix routine. Conversion of vorticity to streamfunction fields then required only a single, computationally efficient matrix multiplication.

Figure A.1 shows an example original eddy vorticity field at mid-depth (top left), and the streamfunction field (top right) derived according to this method. In the bottom left is the vorticity field *rederived* by numerical differentiation of the streamfunction field. In the bottom right, the squared difference between real and rederived vorticity fields is plotted.

As can be seen, the difference between real and rederived fields is fairly small, although it increases towards the edges of the annulus. This is most likely due to boundary layer effects; the free-slip boundary conditions are strictly only valid for a quasigeostrophic fluid. Slight errors are also added by the numerical differentiation mapping ψ' to ζ_{ret}. The difference between the two fields was judged to be small enough to be neglected in the eddy heat flux analysis of Section 6.1.

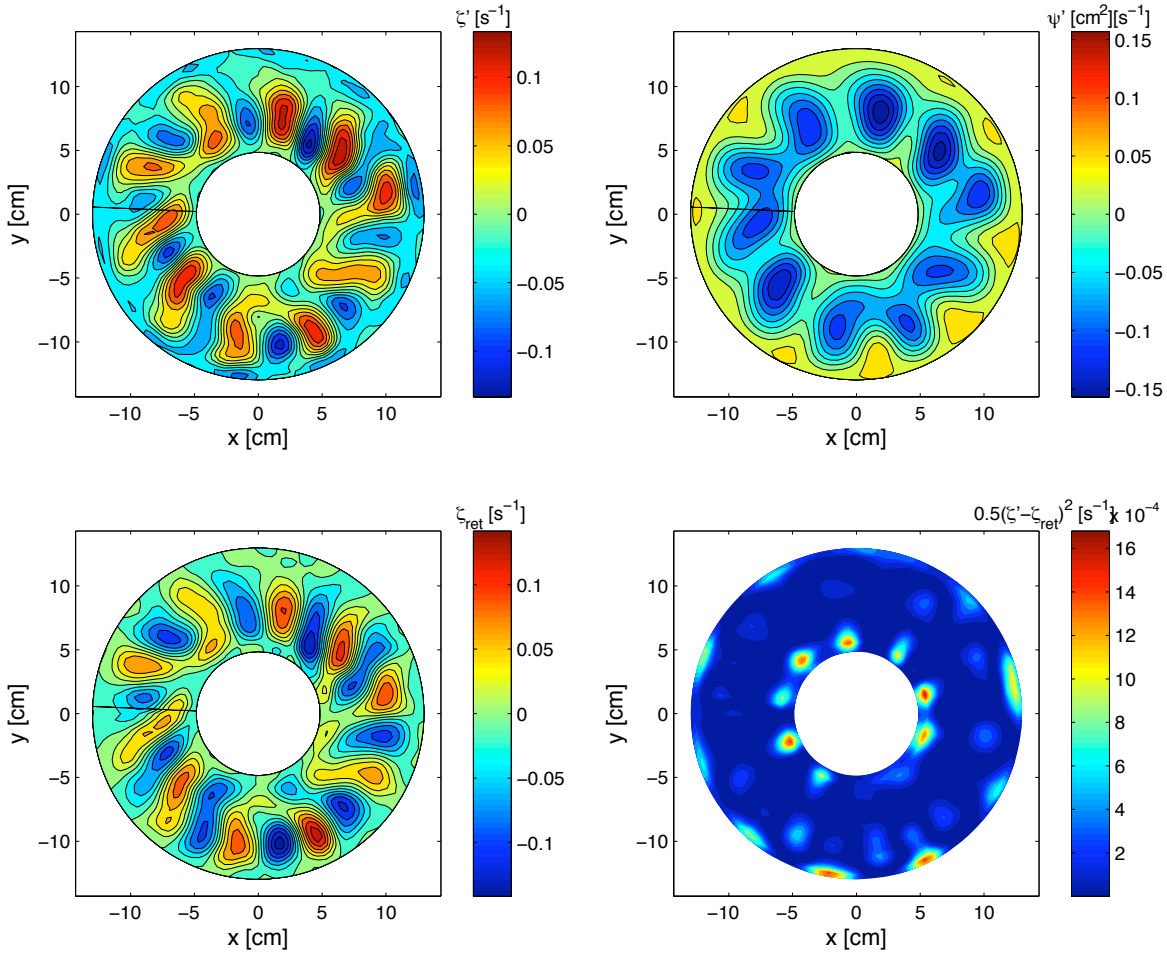

Figure A.1: (top left) Mid-level snapshot of vertical eddy vorticity component ζ' for a sloping boundary experiment with $\Omega = 1.3$ rad s^{-1} and $\Delta T = 2K$. (top right) Mid-level streamfunction ψ' as derived form the algorithm outlined in Chapter 6. (bottom right) Rederived vorticity field ζ_{ret} as calculated from $\nabla^2\psi' = \zeta_{ret}$. (bottom right) Squared vorticity difference $0.5(\zeta' - \zeta_{ret})^2$.

Appendix B

The eigenvalue problem in annular geometry

As discussed in Chapter 6, the cylindrical geometry of the experiment means that spectral expansions are most accurately defined in terms of Fourier-Bessel modes [5]. In this appendix, the method used for producing the plots in Figure 6.15 is described.

Recall that in Section 6.2, it was stated that any scalar ϕ defined in a 2D annular domain $b \geqslant r \geqslant a$, with boundary conditions of the form $\phi(a,\theta) = \phi(b,\theta) = 0$, can be expanded in terms of the complete, orthogonal basis set

$$\phi(r,\theta) = \sum_{m=-\infty}^{m=+\infty} \sum_{n=1}^{n=\infty} \left(\phi^J_{mn} J_m(\gamma_{mn} r) + \phi^Y_{mn} Y_m(\gamma_{mn} r)\right) e^{im\theta} \tag{B.1}$$

with J_m and Y_m Bessel functions of the first and second kind, and γ_{mn} a constant that can be determined numerically. The task of finding the special solution to equation (B.1) is made more complicated by the annular boundary conditions, which do not permit us to remove Y_m, as would be done for a cylindrical domain boundary problem with no inner cylinder.

Firstly, it was necessary to construct a zero-finding program capable of recognising and discarding discontinuities in the function

$$\mathcal{G}_{mn}(\gamma_{mn}) = \frac{J_m(\gamma_{mn} b)}{Y_m(\gamma_{mn} b)} + \frac{J_m(\gamma_{mn} a)}{Y_m(\gamma_{mn} a)} \tag{B.2}$$

which arises from the boundary conditions of (B.1) (see Figure B.1). The bisection method [5] was used for this purpose, with discontinuities recognised by the criterion $|f'(x_0)| > f_{max}$, where f_{max} is chosen to be some very large positive number. This took care of the constants γ_{mn}. Orthogonality of the radial eigenmodes was then checked by numerical calculation of the relation

$$\int_a^b r R_{kl}(\gamma_{kl} r) R_{km}(\gamma_{km} r) \mathrm{d}r = \alpha_{lm} \tag{B.3}$$

with $R_{mn}(\gamma_{mn} r) \equiv J_{mn}(\gamma_{mn} r) + Y_{mn}(\gamma_{mn} r)$. Orthonormality was then imposed by setting $a_{lm} = \delta_{lm}$ in (B.3). In Figure B.2, some example eigenmodes derived by this method are plotted.

In order to project real experimental data onto these modes, a transformation matrix was constructed in Matlab from the complete set of eigenfunctions and inverted. For convenience, an

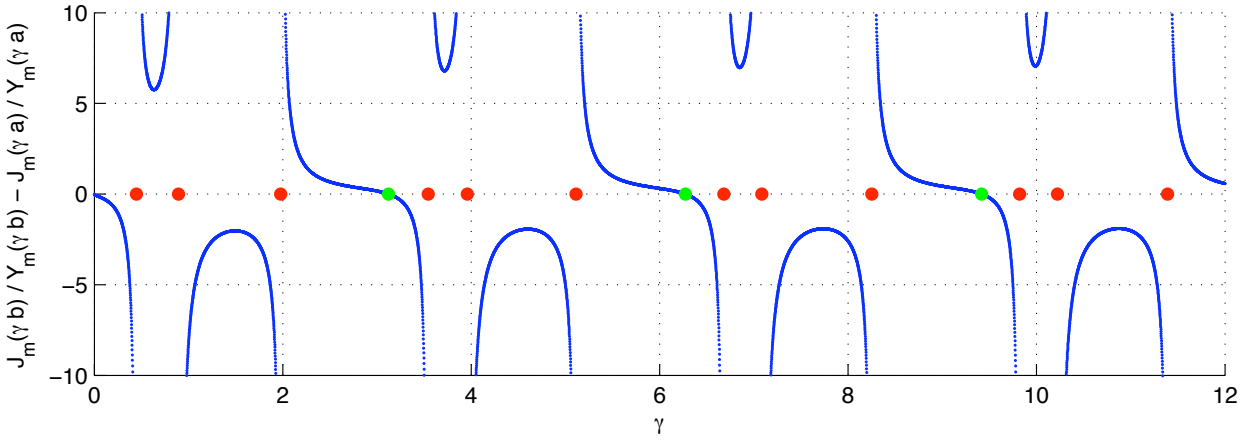

Figure B.1: Blue line shows B.3 as a function of γ. Green and red dots are the true zeros and discontinuities respectively, as predicted by the zero-finding Matlab routine.

azimuthal Fourier transform was performed first, and the radial transformation procedure was performed separately for each mode m.

To derive energy spectra, it was necessary to separately transform azimuthal and radial velocity fields u_θ and u_r. Non-slip boundary conditions implied that both fields were equal to zero at $r = a$, b, so the general expansion form (B.1) could be used for both quantities. Energy spectra were then calculated by multiplying each transformed field with its complex conjugate, and summing the two quantities.

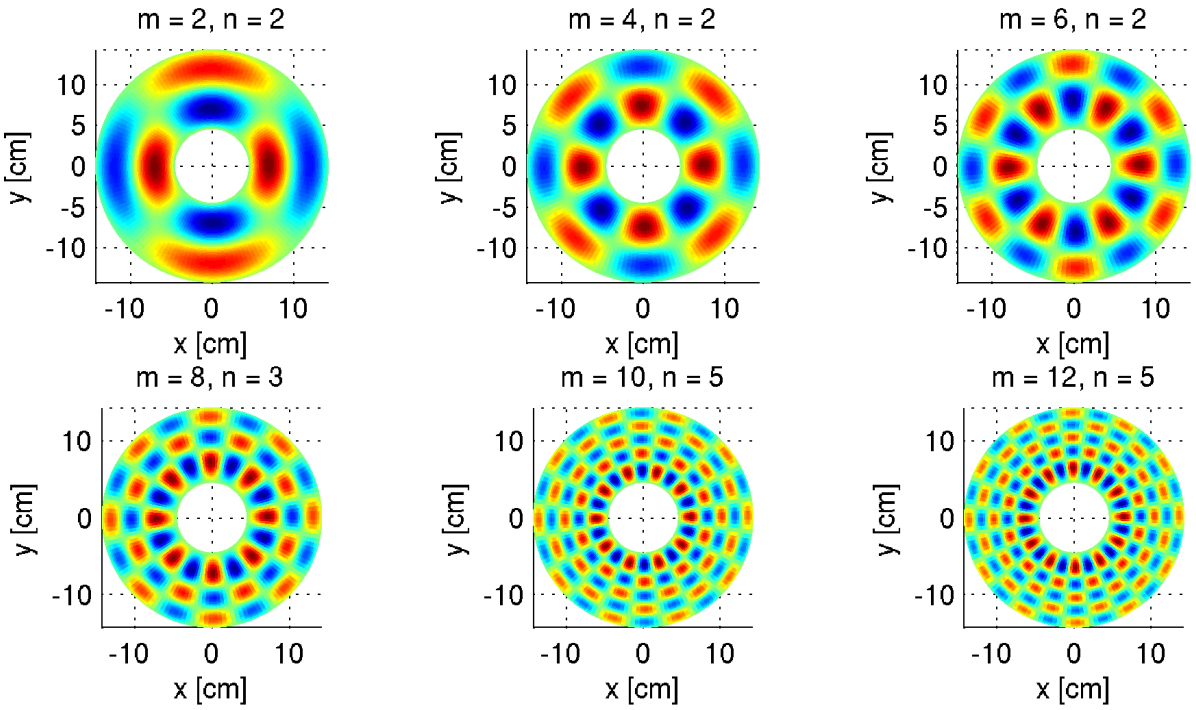

Figure B.2: Selected annular eigenmodes, as described by equation (B.1).

Appendix C

Derivation of the 1D spectral energy transfer equation

Spectral transfer calculations were used in Section 6.2 to study the extent to which eddy-mean flow interactions dominated when the system was in a steady-state. In this appendix, the derivation of the spectral transfer equation 6.10 is given.

Given the quasigeostrophic approximation, the momentum equation in absence of forcing and damping is simply

$$D_0\mathbf{u}_0 \equiv \partial_t\mathbf{u}_0 + \mathbf{u}_0 \cdot \nabla\mathbf{u}_0 = -\mathbf{f}_0 \times \mathbf{u}_1 - \mathbf{f}_1 \times \mathbf{u}_0 \tag{C.1}$$

where $\mathbf{u}_0$ only has components in the horizontal plane.

We are interested in barotropic nonlinear interactions and so ignore the right hand side of (C.1). Dropping the zero subscript on geostrophic quantities for convenience and using cylindrical coordinates, the remainder then becomes

$$\begin{aligned}\left(\frac{\partial}{\partial t} + u_r\frac{\partial}{\partial r} + \frac{u_\theta}{r}\frac{\partial}{\partial\theta}\right)u_r - \frac{u_\theta^2}{r} = 0\\ \left(\frac{\partial}{\partial t} + u_r\frac{\partial}{\partial r} + \frac{u_\theta}{r}\frac{\partial}{\partial\theta}\right)u_\theta + \frac{u_r u_\theta}{r} = 0.\end{aligned} \tag{C.2}$$

Define all variables in terms of their azimuthal Fourier coefficients, e.g.,

$$u_\theta(r,\theta,t) = \sum_m e^{im\theta}u_{\theta,m}(r,t). \tag{C.3}$$

Then substitution of (C.3) into (C.2) followed by a Fourier transform of the entire expression leads to

$$\begin{aligned}\frac{\partial u_{r,m}}{\partial t} + \sum_{m=p+q} a_{pq} = 0\\ \frac{\partial u_{\theta,m}}{\partial t} + \sum_{m=p+q} b_{pq} = 0\end{aligned} \tag{C.4}$$

with the terms a_{pq}, b_{pq} defined as

$$a_{pq}(r,t) = u_{r,p}u'_{r,q} + iq\frac{u_{\theta,p}u_{r,q}}{r} - \frac{u_{\theta,p}u_{\theta,q}}{r}$$
$$b_{pq}(r,t) = u_{r,p}u'_{\theta,q} + iq\frac{u_{\theta,p}u_{\theta,q}}{r} + \frac{u_{r,p}u_{\theta,q}}{r}. \tag{C.5}$$

Defining semi-spectral energy as

$$E_m(r,t) = \frac{1}{2}\left(u_{r,m}u^*_{r,m} + u_{\theta,m}u^*_{\theta,m}\right) \tag{C.6}$$

where * denotes complex conjugate, we can write

$$\frac{\partial E_m(r,t)}{\partial t} = T_m(r,t) = -\sum_{m=p+q} T_{mpq} = 0$$
$$T_{mpq} = \frac{1}{2}\left(u^*_{r,m}a_{pq} + u^*_{\theta,m}b_{pq} + c.c.\right). \tag{C.7}$$

Averaging in time and the radial direction

$$\langle E_m(r,t)\rangle = \frac{2}{T(b^2-a^2)}\int_{t_0}^{t_1}\int_a^b E_m(r,t)r\mathrm{drdt}, \tag{C.8}$$

where t_0 and t_1 are starting and finishing times and $T = t_1 - t_0$, we arrive at the desired result

$$\mathcal{P}_m = \frac{\partial\langle E_m(r,t)\rangle}{\partial t} = -\sum_{m=p+q}\langle T_{mpq}\rangle = 0. \tag{C.9}$$

In the real experimental system, this quantity will of course be balanced by energy loss due to Ekman and viscous damping, and energy transfer due to mixed barotropic – baroclinic interactions.